Reorientation Dynamics of Branched and Linear Alcohols

By

Oluwaseun Olayemi Mesele

Submitted to the graduate degree program in Department of Chemistry and the Graduate Faculty of the University of Kansas in partial fulfillment of the requirements for the degree of Doctor of Philosophy.

Ward H. Thompson, Chairperson

Brian B. Laird

Committee members

Christopher G. Elles

Mikhail V. Barybin

Craig Marshall

Date defended: July 06, 2017

The Thesis Committee for Oluwaseun Olayemi Mesele certifies
that this is the approved version of the following thesis :

Reorientation Dynamics of Branched and Linear Alcohols

Ward H. Thompson, Chairperson

Date approved: July 14, 2017

Abstract

Molecular reorientation of the four isomeric butanols are investigated with molecular dynamics simulations. The purpose of this study is to probe how alcohol reorientational and hydrogen-bond (H-bond) dynamics is influenced by the arrangement of the steric bulk of the isomeric butanols in their liquid state. The OH reorientation times are explained with the extended jump model in which the OH reorientation is broken down into contributions due to "jumps" between H-bond partners and "frame" reorientation of the intact H-bonded pair. In the case of the isomeric butanols, the model provides a quantitative description of the OH reorientation times. Our results show that reorientation is fastest in *iso*-butanol and slowest in *tert*-butanol, while *sec*- and *n*-butanol have similar reorientation times. Similar reorientation times for *sec*- and *n*-butanol is due to the unpredictable cancellation between the jump and frame reorientation in the two alcohols. Entropic, enthalpic and dynamical factors that include transition state recrossing effects are seen to contribute to the jump reorientation times. Finally, a model that is based on the liquid structure is offered to evaluate the enthalpic and entropic contributions to the jump time. This study represents the foundation for a model that predicts OH reorientation times in alcohols even though further work is needed for a better prediction of frame reorientation times and the transition state recrossing effects. An estimation of the activation energy of chemical reactions like jump reorientation of OH groups in alcohols from molecular dynamics simulations has always required numerous simulations at several temperatures. In this work, several methods for calculating the activation energies at a single temperature have been explored. The applications explored include classical and quantum systems and the

activation energy is evaluated using the same time correlation functions that are used to evaluate rate constants from molecular or quantum dynamics trajectories. The use of these time correlation functions show that the activation energy can be evaluated with no extra computational cost. In addition to an analysis of molecular dynamics trajectories, vibrational spectroscopy is a very useful tool for probing structure and dynamics in liquids and the simulation of spectra can be achieved in a variety of ways. Empirical maps for spectroscopic quantities required for the simulation of spectra of OH stretching vibrations are related to the electric field on the hydrogen atom due to the surrounding liquid molecules. Upon the analysis of the four lowest linear alcohols, methanol, ethanol, *n*-propanol, and *n*-butanol, it is shown that a single (“universal") map can be used for alcohols with different alkyl groups. Spectra of the OH stretch simulated for the four lowest linear alcohols with this “universal" map is in very good agreement with those that are simulated using maps that have been optimized for the individual alcohols. However, the spectra resulting from this map differs from that simulated using maps developed for water. The simulated spectra suggest that it may be possible to use one map to simulate OH stretching vibration in other alcohols that are not part of the study. The simulated spectra are very similar to available experimental spectra and the role of non-Condon effects, reorientation dynamics, hydrogen bonding, and spectral diffusion in the simulated spectra are discussed. The Empirical maps developed for the OH stretching vibration of alcohols were used to simulate the IR, Raman, and 2D-IR photon echo spectra of isotopically dilute isomeric butanols. Raman spectra shows that the branched isomers have more weakly bonded alcohols compared to linear alcohols. While the simulation of the vibrational spectra of the OH stretch of isotopically dilute alcohols is relatively straightforward, the accurate simulation of vibrational spectra of the OH stretch in the neat liquids requires a good estimate of intermolecular vibrational coupling. The discrete variable representation method is used to calculate intermolecular vibrational coupling of OH and OD bonds

in water. Intermolecular vibrational coupling decreases on H→D substitution and the transition dipole coupling approximation is seen to accurately predict the intermolecular vibrational coupling constant at long intermolecular distances.

Contents

List of Figures

List of Tables

Chapter 1

Introduction

1.1 Reorientation Dynamics and its Influence on Chemical Processes Involving Alcohols

In liquids like alcohols and water where the molecules interact through hydrogen bonds (H-bonds), thermal fluctuations are enough to encourage continuous breaking and forming of hydrogen bonds. This breaking and forming of hydrogen bonds involves reorientation of the molecules and an exchange of H-bond partners (See Fig. 1.1). Because some of the interesting macroscopic properties [4, 5] of these liquids are due to the hydrogen bonds present in them, there is need for a molecular level understanding of the mechanism and rate of the breaking and forming of H-bonds.

Among liquids where there are H-bonds, water is the most widely studied and there seems to be agreement in the scientific community about the mechanism and timescale of H-bond exchange in water even though there are still questions left unanswered about its nature. Unlike water, alcohols which also interact through H-bonds have not been well studied. The dearth of studies on alcohols is rather curious. This is because like water, alcohols also have a wide range of applications in the chemical and technology industry. In the chemical industry, they are used in separation processes because unlike water, they are miscible with many organic solvents. They are also used as fuels, as reactants, solvents, and co-solvents in chemical reactions.

The reactivity of alcohols is mainly due to the extremely acidic nature of their hydrogen atom which can be prone to substitution reactions in deuterium oxide (heavy water) and sodium hydroxide, and the susceptibility of their hydroxyl groups to nucleophilic substitution reactions. The common theme among these reactions and some reactions (e.g proton transfer, where alcohols act

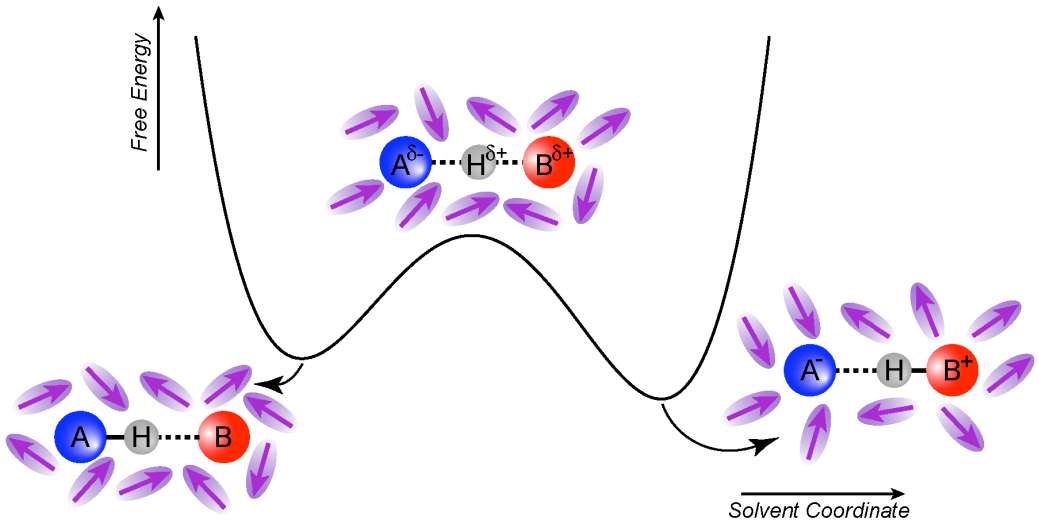

Figure 1.1: Reactant, transition state, and product during H-bond exchange. Figure shows H_d (hydrogen atom of the donor molecule), O_A (oxygen atom of the closest acceptor), O_B (oxygen atom of the next closest acceptor).

as solvent) is the presence of a charged transition state or intermediate. For these type of reactions, the rate determining step involves reorientation of the alcohols in order to stabilize the charged intermediate states.

Fig. 1.2 shows the reaction energy profile of a proton transfer reaction where the rate determining step is the reorientation of the solvent. A neutral reactant state where the solvent molecules are randomly arranged around the reactants is shown on the left. In the middle, we see the transition state where there is partial charge transfer and the solvent molecules are seen to be fairly oriented around the partially charged transition state. Finally, the molecular dipoles are seen to be aligned around the charged product in such a way that they stabilize the new charge distribution. These many uses of alcohols and the role that the dynamics of molecular reorientation plays on the nature of these processes makes the study of different alcohols very important

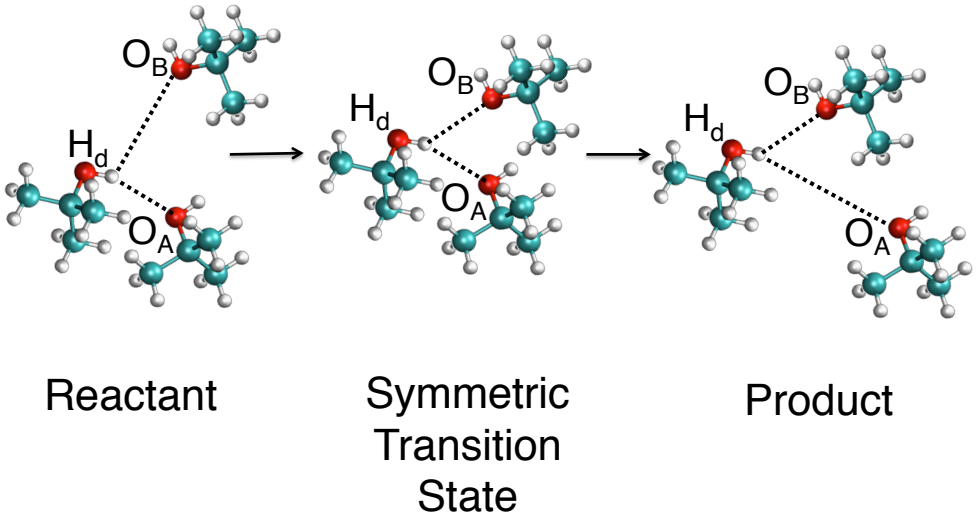

Figure 1.2: Reaction energy profile of a proton transfer reaction. The structure on the left is the neutral reactant, in the middle the transition state, and on the right the product.

1.2 Predicting Molecular Reorientation Times from Molecular Dynamics Simulations

In molecular dynamics (MD) simulations the trajectories of the position and velocities of particles are determined using classical mechanics. These trajectories contain the positions and velocities due to the interaction of the particles as a function of time. In order to predict molecular reorientation times, diffusion coefficients, and other transport properties, the generated trajectory file is then analyzed. In the case of H-bonded molecules like alcohols, the molecular reorientation is followed by the autocorrelation function ($C_\ell(t)$) of the OH bond,

$$C_\ell(t) = \langle P_\ell[\mathbf{e}_{OH}(0)\cdot\mathbf{e}_{OH}(t)]\rangle \approx \sum_{i=1}^{n} A_i e^{-1/\tau_i}, \tag{1.1}$$

where P_ℓ is the Legendre polynomial of order ℓ and $\mathbf{e}_{OH}(t)$ is the unit vector along the OH axis at time t. Most of the time, the second order Legendre polynomial ($C_2(t)$) is calculated because the results of this correlation function determined from MD simulations can be related to some experimental observables determined from IR pump-probe anisotropy experiments,[6–8] as well as NMR measurements.[9–13]

1.3 Molecular Reorientation Times from Experiments and Molecular Dynamics Simulations

In the IR pump-probe anisotropy experiment, the anisotropy decay ($r(t)$) is related to two-fifths of the second order autocorrelation function $C_2(t)$ making it possible to extract reorientation times of OH bonds of alcohols. As shown in Eq. 1.1, the $C_2(t)$ autocorrelation function from simulations can be fit to a sum of exponentials with the different timescales related to the different modes of molecular reorientation.[14] The fastest timescale is known as the inertial timescale and involves collision with other molecules within its mean free path. The second timescale is known as the librational timescale and has to do with reorientation of molecules within the hydrogen bond network. This back and forth wobbling motion within the hydrogen bond network is due to the inertial collision with other molecules and the restoring force due to the hydrogen bond cage that wants to restore the molecules to their initial hydrogen bond geometry. Finally, the slowest timescale is the one that involves complete reorientation of the molecules with a change in hydrogen bond partner. Previous simulation of the IR pump-probe[3] of methanol, ethanol, and *iso*-propanol give slow reorientation times of 4.6, 12, and 27 ps respectively which compares well to $C_2(t)$ reorientation times of 5.5 ± 0.3 and 12.1 ± 1.7 for methanol and ethanol from previous MD simulations.[14]

In the case of NMR experiments, the average reorientation time is related to the spin-lattice relaxation time (T_1) by the relation,[9, 10]

$$1/T_1 = \frac{3\pi}{2}\chi^2 \langle \tau \rangle , \tag{1.2}$$

where $\langle \tau \rangle$ is the average reorientation time given by $\langle \tau \rangle = \int_0^\infty C_2(t)\, dt$ in MD simulations, and χ^2 is the quadrupolar coupling constant. Knowledge of the quadrupolar coupling constant and spin-lattice relaxation gives the average $C_2(t)$ reorientation time which includes the inertial, librational, and slow OH reorientation timescales. Experiments have shown that the average reorientation time increases with increasing alkyl chain length as we go from methanol to pentanol [15, 16] and it will be shown in Chapters 3 and 4 that the NMR relaxation times compare well to the values determined

from MD simulations.

Two-dimensional IR photon echo experiments described in Chapter 4 is another way by which molecular reorientation can be probed. In this experiment, the time evolution of the vibrational frequency of the OH stretch is determined. The changing OH stretch vibrational frequency is a measure of the local H-bond environment of the OH group. The timescale of the evolution of the vibrational frequency (*i.e.,* spectral diffusion) is thus another measure of molecular reorientation in alcohols. Simulations of the 2D-IR photon echo of methanol, ethanol and *iso*-propanol have shown that the slow reorientation times are 4, 7, and 14 ps respectively.[3] These times, especially for ethanol and *iso*-propanol are seen to be smaller than that determined from the IR pump-probe experiments but still show a slower reorientation (spectral diffusion) with increase in the length of the alkyl chain of the alcohol. The difference in the timescales of spectral diffusion in comparison to OH reorientation times has been said to indicate a difference between the mechanism of randomization of OH vibrational frequency (*i.e.,* spectral diffusion) and OH reorientation in the alcohols.

1.4 Mechanism of Molecular Reorientation

There are several theories that describe molecular reorientation in liquids with the Debye-rotational Brownian motion[17] being one of the oldest and most used. In the Debye model, molecular reorientation in H-bonded liquids like alcohols involves the random and small angular displacement of a molecule when it breaks away from its initial H-bond partner until it finds a new H-bond partner. The diffusive reorientation time is given by,

$$\tau_\ell = \frac{1}{\ell(\ell+1)D_R}, \tag{1.3}$$

where ℓ is the rank of the Legendre polynomial, and D_R is the rotational diffusion constant. The diffusive reorientation times can be calculated from molecular dynamics simulations and it can then be determined if the mechanism of molecular reorientation in the liquid follows a Debye

model. For liquids where the reorientation follows this Debye model, the ratios of reorientation times become $\tau_1/\tau_2 = 3$ and $\tau_1/\tau_3 = 6$.

Molecular dynamics simulations of water give time ratios of 2.0 ± 0.4 and 2.9 ± 0.6 for τ_1/τ_2 and τ_1/τ_3 respectively. These values indicate that molecular reorientation in water doesn't follow the Debye model. Better agreement with the Debye model is found for methanol where we have $\tau_1/\tau_2 = 2.5 \pm 0.2$ and $\tau_1/\tau_3 = 4.6 \pm 0.3$ for methanol and $\tau_1/\tau_2 = 3.1 \pm 0.5$ and $\tau_1/\tau_3 = 6.5 \pm 1.0$ for ethanol. These results have been ascribed to the increasing weight of the reorientation of intact H-bonds as the jump times become longer.[14] Both the jump time and intact H-bond reorientation times are described in the final paragraph of the current section.

In contrast to the Debye model, the Ivanov model[18] says that the mechanism through which molecules switch H-bond partners involves large amplitude angular jumps. In this model, this jump reorientation time is given by,

$$\tau_\ell^{jump} = \tau_0 \left[1 - \frac{1}{2\ell+1} \frac{[(\ell+1)/2\Delta\theta]}{sin(\Delta\theta/2)} \right]^{-1}, \tag{1.4}$$

where τ_0 is the time it takes to jump from one H-bond to another, $\Delta\theta$ is the angle $(O_A - O_d - O_B)$ immediately after a jump and ℓ is again the rank of the Legendre polynomial, and A, d, and B stand for the initial hydrogen bond acceptor, the donor, and the final acceptor molecule.

The extended jump model (EJM) is an improvement on the Ivanov model. The EJM which has been successfully used to describe reorientation in water and alcohols like methanol and ethanol[14, 19] describes OH reorientation as occurring on two different timescales. The first timescale is that described by the Ivanov jump model (jump time) and the second timescale is a rotational diffusive motion of intact H-bond partners known as the "frame" time. It should be noted that the rotational diffusion in this case is different from the Debye diffusive time where the diffusion is that of non-hydrogen bonded molecules. As shown in Eq. 1.5, the total molecular reorientation time (τ_2) which is determined from the $C_2(t)$ correlation time, is related to the jump

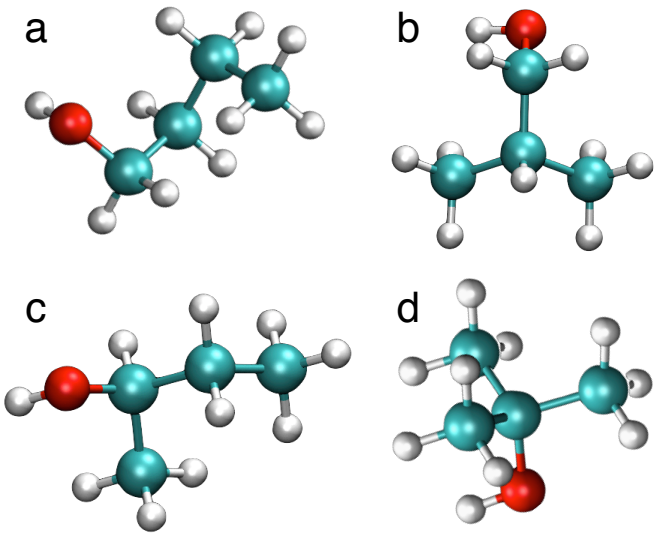

Figure 1.3: Structures of the four isomeric butanols: (a) *n*-butanol (b) *iso*-butanol, (c) *sec*-butanol, and (d) *tert*-butanol.

and frame reorientation time:

$$\frac{1}{\tau_2} = \frac{1}{\tau_2^{frame}} + \frac{1}{\tau_2^{jump}}. \tag{1.5}$$

As stated in the previous paragraph, studies of some alcohols and water have shown that molecular reorientation in these liquids is adequately described by the EJM. For this reason, the molecular reorientation study on isomeric butanols will be investigated within this model of molecular reorientation.

1.5 Purpose of the Current Study

While some studies of linear alcohol have shown changes in the mechanism and timescale of their molecular reorientation with increasing chain length, the aim of this work is to understand how different arrangement of steric bulk of alcohols of the same molecular weight as well as an increase in the alkyl chain length of linear alcohols affect the mechanism and timescale of molecular reorientation. Using the tools of molecular dynamics and vibrational spectroscopy, we will investigate the structure and dynamics of isomeric butanols (see Fig. 1.3) and linear alcohols (methanol, ethanol, propanol, and butanol). Ultimately, we are seeking a predictive model that

describes molecular reorientation based on the structure of the liquid. It is hoped that this work will lay a strong groundwork for further experimental studies to verify the results and conclusions reached in this study.

The rest of this dissertation is arranged as follows. In chapter 2, based on the MD simulations of isomeric butanols a predictive model derived from the liquid structure is used to describe molecular jump reorientation in alcohols. In chapter 3, a method of calculating activation energies for molecular reorientation and other chemical reactions based on a single molecular dynamics simulation is explored. In chapter 4, empirical maps based on methanol, ethanol, propanol, and butanol are developed for simulating the OH vibrational spectra of alcohols. The infrared, Raman, and 2D-IR photon echo spectra of the OH vibration of isotopically dilute methanol, ethanol, propanol, and butanols are simulated and compared with results from experiments. In chapter 5, the empirical maps developed for alcohols are used to simulate the vibrational spectra of the OH stretch of isotopically dilute isomers of butanol. Chapter 6 shows how intermolecular vibrational coupling of OH bonds in water can be calculated using a sinc-function discrete variable representation (DVR), how the intermolecular coupling changes with isotopic substitution as we move from OH to OD, and how these results will affect the spectra of the neat water and heavy water. In the final chapter concluding remarks are given with an outlook on future directions.

Chapter 2

Reorientation of Isomeric Butanols: The Multiple Effects of Steric Bulk Arrangement on Hydrogen-Bond Dynamics

Alcohols are classical protic liquids widely used as both reactants and solvents for chemical reactions. The properties of alcohols can be widely varied through modification of the alkyl group, yielding both interesting fundamental behavior and broad usefulness in practical applications. In particular, as solvents the reorientational dynamics of alcohols can play a key role, for example, in charge transfer[20–22] and solvolysis reactions.[23] As protic solvents, it is not only the reorientational timescales that can be important, those associated with exchanges of hydrogen-bond (H-bond) partners can also influence reaction dynamics. While reorientational and H-bond dynamics are naturally related, their connection varies with the alcohol (*vide infra*). This role of alcohols as commonly used solvents in organic transformations along with the presence of OH groups in biological macromolecules has spurred significant interest in understanding hydroxyl reorientation and H-bond dynamics in alcohols.[3, 8, 24–29]

The nature of molecular reorientation of the OH group of water in the bulk and at interfaces has been investigated by several groups[6, 7, 19, 30–37] while only a few such investigations have been reported for alcohols.[3, 8, 14, 38–41] A key recent advance has been the development of the extended jump model[19, 30] (EJM) to describe OH reorientation in water. Within this model the OH reorientation dynamics arises from two components: "jumps" associated with an exchange of H-bond partners[18] and diffusive "frame" reorientation of intact H-bonded pairs. The EJM has been successfully used to describe water dynamics including near solutes and interfaces. Reorientation in water is dominated by large-amplitude jumps, occurring with a timescale of ~ 3 ps

and with an average jump angle around 70°. Recently, our group showed that the EJM can also be used to describe OH reorientation in the lower alcohols methanol and ethanol.[14] In those liquids, the alcohol alkyl group prevents the approach of potential new H-bond acceptors, significantly slowing the timescale for H-bond jumps compared to water. As a consequence the OH reorientation times in methanol and ethanol are dominated by the frame reorientation of intact H-bonds between jumps, in contrast to water.

A detailed review by Böhmer *et al.* of the history of work on the structural and dynamical properties of monohydroxy alcohols has recently appeared.[28] They note the substantial progress that has been made in understanding the behavior of alcohols but also the significant questions that remain. The past two decades have seen significant activity in the study of the structural and dynamical properties of alcohols. Butanols specifically, the subject of the present work, have been examined using techniques including NMR,[10, 42–45] vibrational spectroscopy,[8, 45–55] second harmonic generation at interfaces,[56, 57] solvation dynamics,[58–60] neutron and X-ray scattering,[44, 45, 61–64] and dielectric relaxation spectroscopy.[28, 43, 54, 55, 65–67]

In this work, I use molecular dynamics (MD) simulations to study the OH reorientation dynamics in the four isomeric butanols, *n*-butanol *iso*-butanol, *sec*-butanol, and *tert*-butanol shown in Figs. 2.1 a, b, c, and d in their respective bulk liquids. These molecules all possess the same quantity of steric bulk but with a different arrangement. Previous NMR measurements on linear alcohols have shown that increasing the alkyl chain length of linear alcohols leads to a slow down in the OH reorientation.[15] However, investigations that provide a molecular picture of the role of steric bulk on reorientation in butanols are at best sparse.[15, 39, 43, 68–73] Thus, the aim of this study is to improve our understanding of how the spatial arrangement of the steric bulk influences OH reorientation as well as H-bond dynamics. As such, the present work extends our previous study of methanol and ethanol reorientation dynamics.[14]

The OH reorientation dynamics can be characterized through the autocorrelation function,

$$C_\ell(t) = \langle P_\ell[\mathbf{e}_{OH}(0) \cdot \mathbf{e}_{OH}(t)] \rangle \,, \tag{2.1}$$

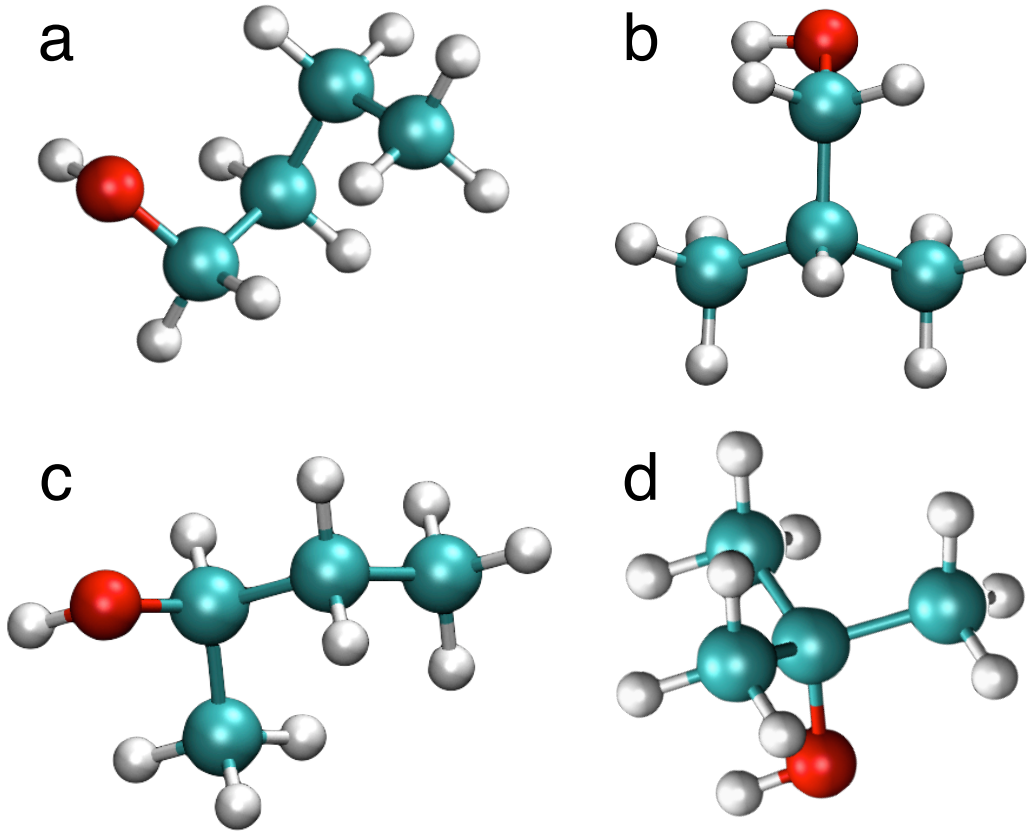

Figure 2.1: Structures of the four isomeric butanols: (a) *n*-butanol (b) *iso*-butanol, (c) *sec*-butanol, and (d) *tert*-butanol.

where P_ℓ is the Legendre polynomial of order ℓ and $\mathbf{e}_{OH}(t)$ is the unit vector along the OH axis at time t. In the present work, we will consider $\ell = 2$ as $C_2(t)$ can be compared to experimental results. Specifically, reorientation times calculated from the decay of the $C_2(t)$ can be compared to that determined from IR pump-probe anisotropy experiments,[6–8] as well as NMR measurements[15, 16]. In the latter case, NMR experiments provide the average reorientation correlation time,

$$\langle \tau \rangle = \int_0^\infty C_2(t)\, dt, \tag{2.2}$$

which also includes contributions from the inertial and librational motions of the OH group.

In this work, trajectories generated from MD simulations are used to determine the autocorrelation function $C_2(t)$ for the four isomeric butanols. These results are examined in the context of the EJM and a detailed analysis of the contributions to the OH reorientation timescales, particularly

the jump contribution, is carried out. The aim is to uncover the key properties that would be required to construct a predictive model for reorientation and H-bond exchange dynamics. Thus, the jump time is decomposed into its energetic, entropic, and dynamical constituents and their origins are examined. As a result, a simple model is proposed that is capable of reproducing some, but not all, of the factors describing H-bond exchanges in the isomeric butanols. The remaining pieces to a fully predictive model are discussed.

2.1 Simulation Details

Classical molecular dynamics (MD) simulations were carried out using the LAMMPS software.[74] The OPLS-AA force field[75, 76] was used to describe the interactions for all four alcohols, the structures of which are shown in Fig. 2.1. Lennard-Jones interactions were evaluated within a cut-off of 12 Å. The long-range electrostatic interactions were included using three-dimensional periodic boundary conditions and an Ewald summation with a tolerance of 1×10^{-4}. Three 40 ns trajectories were propagated for each alcohol and configurations were saved every 100 fs. The difference between these three is the length of a velocity-rescaling step, which was part of a two-step equilibration used in all simulations. The length of this velocity-rescaling stage was 0.25, 0.5, and 0.75 ns for the three trajectories integrations. Velocity rescaling was followed by a 4 ns equilibration and then a 40 ns NVT data collection period with a 1 fs timestep.

The isomers of butanols were simulated using 256 molecules at 298 K except *tert*-butanol which was simulated at 301 K due to its high melting point. Cubic boxes of side length 33.9 Å, 33.9996 Å, 33.95 Å, and 34.2 Å were used for *n*-butanol, *iso*-butanol, *sec*-butanol, and *tert*-butanol, respectively, to match the experimental density of *tert*-butanol at 301 K and for all other alcohols at 293 K.[77] Temperature-dependent properties are determined from the simulations of these alcohols at 315 K, 330 K, and 345 K. A Nosé-Hoover[78, 79] thermostat with a time constant of 0.1 ps was used to maintain the temperature during the data collection period. Tests were carried out to ensure that the thermostat did not affect the reorientation dynamics by carrying out shorter trajectory calculations in the NVE and NVT ensemble and comparing both results. For

tert-butanol, which exists as a liquid only at temperatures above room-temperature, the translation diffusion coefficient was calculated at the simulation temperature and experimental density and values close to those reported in experiments[39] were obtained.

Error bars were calculated using block-averaging with 10 blocks and reported as 95% confidence intervals using the Student *t*-distribution.[80]

2.2 Results

2.2.1 Hydroxyl Reorientation Timescales

Trajectories propagated for all four alcohols using the simulation approach described above were used to calculate the $C_2(t)$ autocorrelation functions (eq. 2.1) plotted in Fig. 2.2. The OH reorientation is found to occur on multiple timescales. For water, methanol, and ethanol,[14, 19] the reorientation correlation functions are well-described by a tri-exponential: the fastest timescale, $\tau_{iner} \leq 400$ fs, corresponds to inertial rotation, the intermediate one, τ_{libr}, to effectively librational motion, and the longest timescale, τ_2, to reorientation associated with hydrogen-bond exchanges. This last timescale is the one that leads to complete reorientation of the hydroxyl group and is the focus of the present work. For the isomeric butanols this long-time reorientation dynamics is not fully described by a single timescale. The origin of this multi-exponential behavior is not yet clear, but it is also only a minor feature. Describing the longer time reorientation dynamics with two timescales, *i.e.*, an overall four exponential fit to $C_2(t)$, does not lead to different qualitative or quantitative conclusions than adopting a single exponential description. Thus, we use the same approach previously adopted for water and the lower alcohols and obtain τ_2 from the longest timescale in a three exponential fit to $C_2(t)$; the minor error associated with this treatment can be seen in Fig. 2.2.

The τ_2 values are given in Table 2.1 and indicate that OH reorientation is fastest for *iso*-butanol and slowest for *tert*-butanol. Interestingly, the OH correlation times for *n*-butanol and *sec*-butanol, which are intermediate between those for *iso*- and *tert*-butanol, are nearly indistinguishable (as is

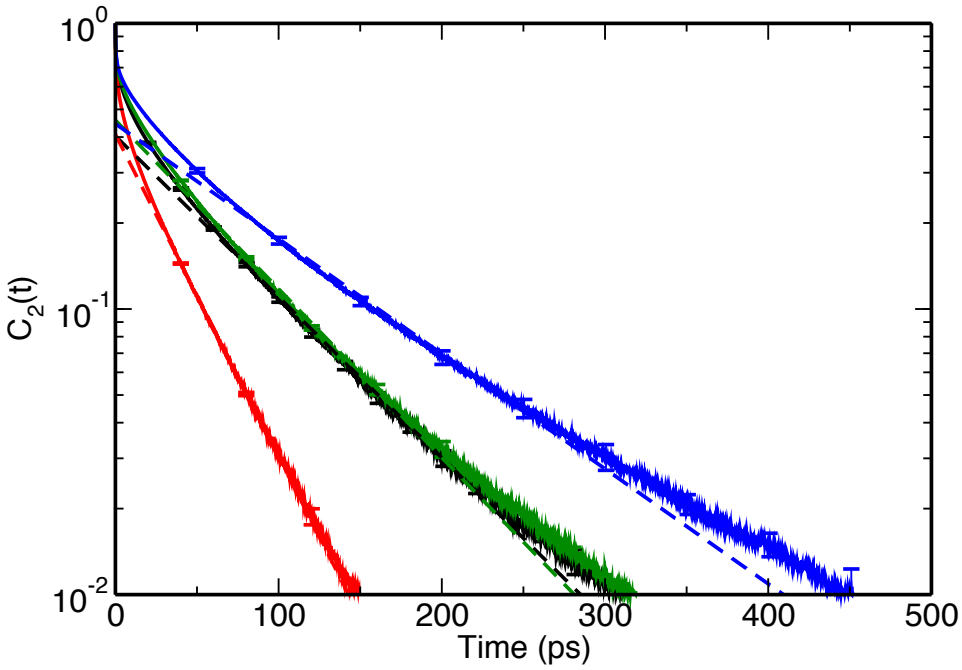

Figure 2.2: Reorientation autocorrelation function, $C_2(t)$, for *n*-butanol (black), *iso*-butanol (red), *sec*-butanol (green), and *tert*-butanol (blue) is plotted against time; dashed lines show the exponential fits to the long-time decay of the correlation functions (see the text).

also evident from Fig. 2.2).

Table 2.1 also gives the average reorientation times (eq. 2.2) from simulation, $\langle\tau\rangle_{MD}$, that include inertial, librational, and reorientational contributions. The average time for *n*-butanol determined from NMR experiments[15] is also provided for comparison. The two results are in reasonable agreement, with the simulated result of $\langle\tau\rangle_{MD} = 36.5$ ps being $\sim 25\%$ smaller than that from NMR measurements $\langle\tau\rangle_{NMR} = 51$ ps. Smaller values for average reorientation times from simulations compared to experiments were also observed previously for methanol and ethanol.[14] Whether this is a generic result or not is still unclear; it is possible that improved forcefields will be required to improve the agreement between simulations and NMR measurements. Apart from *n*-butanol, we are unaware of any data on average reorientation time of the other butanol isomers, though such measurements would be of significant interest.

Table 2.1: Timescales and amplitudes determined from single exponential fits of the long-time decay of $C_2(t)$ for all of the alcohols; all times are in ps.

Molecule	τ_2	$\langle\tau\rangle_{MD}$	$\langle\tau\rangle^{\ddagger}_{NMR}$
			‡ Ref. 15
n-butanol	74.9	36.5 ± 0.4	51
iso-butanol	39.8	17.7 ± 0.1	–
sec-butanol	75.3	38.4 ± 0.6	–
tert-butanol	104.8	55.1 ± 1.6	–

In the remainder of this Section, we analyze OH reorientation in the isomers of butanol using the extended jump model. Results from jump reorientation times, frame reorientation times, jump angle distribution, and the excluded volume effect are then used to identify the role of the different arrangement of steric bulk on the trend in reorientation of the four isomers.

2.2.2 Extended Jump Model (EJM)

The extended jump model describes reorientation as occurring through a combination of two mechanisms: 1) jumps associated with the exchange of H-bonding partners, and 2) "frame" reorientation of intact H-bonds between jumps.[19] It can be expressed mathematically as

$$\frac{1}{\tau_2} = \frac{1}{\tau_2^{frame}} + \frac{1}{\tau_2^{jump}}, \tag{2.3}$$

where τ_2 is the reorientation time discussed above obtained from $C_2(t)$ and τ_2^{jump} (τ_2^{frame}) is the contribution from H-bond jumps (frame reorientation). The EJM was previously shown to describe the slowdown in OH reorientation in methanol and ethanol compared to water.[14] In that case, the alcohol alkyl group blocks potential new H-bonding acceptors, resulting in a slowdown in jump reorientation. In addition, while a complete theory for the trend in frame reorientation is still lacking, the timescale of frame reorientation also changes from water due to a combination of effects, including changing viscosity and the difference in the size and shape of the reorienting intact H-bonded groups. These same effects are present in butanols, with the modification that

each isomer has the same total alkyl group size, but in a different arrangement. For methanol and ethanol, the slowdown in H-bond exchanges is sufficiently great that OH reorientation is dominated by the frame component,[14] *i.e.*, rotation of intact H-bonds. For the butanols the picture is not so simple, as discussed below.

Within the EJM, the contributions to the reorientation time, τ_2, can be independently obtained from the trajectory results. The H-bond exchanges can be considered as a chemical reaction characterized by a rate constant, k_{jump}, and corresponding jump time, $\tau_0 = k_{jump}^{-1}$. Then the contribution of these jumps to the OH reorientation time, τ_2^{jump}, is a combination of this timescale for making a jump and a geometrical factor that depends on the angle traversed by the OH group during the jump, $\Delta\theta$:[18, 19]

$$\tau_2^{jump} = \tau_0 \left[1 - \frac{\sin(5\Delta\theta/2)}{5\sin(\Delta\theta/2)} \right]^{-1}. \tag{2.4}$$

The frame time contribution, τ_2^{frame}, to the OH reorientation is obtained from the $C_2(t)$ autocorrelation function of the $O\cdots O$ vector for continuously H-bonded molecules:

$$C_2^{frame}(t) = \langle P_2[\mathbf{e}_{OO}(0)\cdot\mathbf{e}_{OO}(t)]\rangle\,. \tag{2.5}$$

Here, $\mathbf{e}_{OO}$ is the $O\cdots O$ unit vector for an intact hydrogen bond and P_2, as described earlier, is the second Legendre polynomial. The $O\cdots O$ vector is used to eliminate the fluctuations of the OH vector around the intact H-bond that do not lead to reorientation. We now discuss the determination of each of these contributions, τ_0, $\Delta\theta$, and τ_2^{frame}, and the trends in their values among the isomeric butanols.

2.2.2.1 Hydrogen Bond Jump Times

The jump time, τ_0, can be determined from the MD trajectory using the stable-states picture of reactions.[19, 81, 82] In this approach the jump reorientation times between H-bond switches are

obtained through the time-correlation function,

$$C_{AB}(t) = \langle n_A(0) n_B(t) \rangle \,. \tag{2.6}$$

Here, $n_A(0)$ equals 1 if a molecule is donating a hydrogen bond to an acceptor molecule at a time chosen to be $t = 0$, that molecule is then labelled A; $n_A(0) = 0$ if the molecule is not donating an H-bond and thus does not contribute to $C_{AB}(t)$. Analogously, $n_B(t)$ equals 1 if the same donor molecule has switched H-bonding partners to a new acceptor, labelled B, at time t and $n_B(t) = 0$ if the donor is not H-bonded to B at time t. Absorbing boundary conditions are used, such that $n_B(t) = 1$ for all times after an H-bond switch. In this way, $C_{AB}(t)$ measures the hydrogen bond exchange rate constant k_{jump} and not the subsequent dynamics. Thus, $C_{AB}(t)$ rises from 0 to 1 with increasing t as the population of molecules that have switched H-bonding partners grows. It can be shown that if these exchanges represent a rate process, that $1 - C_{AB}(t)$ decays exponentially as e^{-t/τ_0}, or, equivalently,

$$\tau_0 = \int_0^\infty [1 - C_{AB}(t)]\, dt. \tag{2.7}$$

In this work, τ_0 is obtained *via* eq. 2.7 using a (strict) geometric definition of hydrogen bonds: $r_{O_d \cdots O} \leq 3.1$ Å, $r_{H_d \cdots O} \leq 2.0$ Å, and $\theta_{O_d H_d \cdots O} \leq 20^\circ$, where O_d and H_d represent the donor O and H atoms.

The stable states jump correlation function is plotted as $1 - C_{AB}(t)$ and shown in Fig. 2.3 for each of the four isomeric butanols and the corresponding jump times are given in Table 2.2. The trend in jump times among the four alcohols follows the trend *iso*-butanol < *n*-butanol < *sec*-butanol < *tert*-butanol. This generally indicates a slowdown in jump reorientation with increasing steric bulk around the α-carbon as the primary alcohols, *n*-butanol and *iso*-butanol exhibit faster H-bond exchange dynamics times compared to the secondary and tertiary alcohols. In particular, jumps in *sec*-butanol and *tert*-butanol are slower than those in *iso*-butanol by factors of roughly three and four, respectively. It is interesting that *iso*-butanol has faster H-bond dynamics than *n*-butanol; both have the same steric arrangement around the α-carbon and differ only in the placement of the

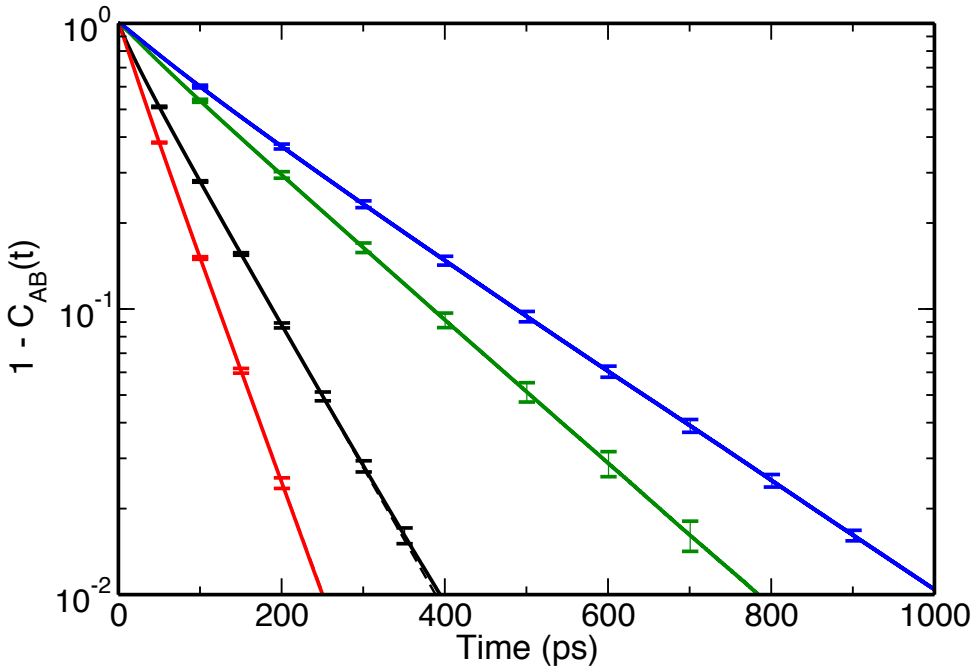

Figure 2.3: Jump correlation function, $1 - C_{AB}(t)$, is shown as a function of time for the four isomers of butanol. Colors are the same as in Fig. 2.2.

fourth methyl group; the origin of this result is not obvious.

The jump times of *n*-butanol and *sec*-butanol deserve particular attention in light of the fact that the two alcohols have essentially identical OH reorientation times (Table 2.1). In contrast, the H-bond exchange time for *sec*-butanol is twice that of *n*-butanol. Taken together with eq. 2.3, these two results indicate that the ordering of the frame reorientation times must be reversed from those of the jump times to give a remarkable cancellation leading to degenerate τ_2 values. This behavior is examined in detail in the Discussion in the context of the structural differences in these two alcohols.

2.2.2.2 Jump Angle Distributions

The other component of the jump time contribution to OH reorientation, τ_2^{jump}, is the jump angle, $\Delta\theta$. This is defined as the $O_A - O_d - O_B$ angle at the transition state for H-bond exchange; here,

Table 2.2: Comparison of jump time, average jump angle, jump time contribution, frame time, and EJM predicted times, τ_2^{EJM} from eq. 2.3, compared to OH reorientation times calculated directly from simulation, τ_2; all times are in ps.

Molecule	τ_0	$\langle\Delta\theta\rangle$	τ_2^{jump}	τ_2^{frame}	τ_2	τ_2^{EJM}
n-butanol	79.4	64°	105	158	74.9	62.9
iso-butanol	53.1	71°	65	86.7	39.8	36.9
sec-butanol	166	73°	199	122	75.3	75.6
tert-butanol	208	76°	245	191	104.8	107

O_A indicates the oxygen atom of the old acceptor, O_B that of the new acceptor, and O_d the donor oxygen.[19] The jump angle is best determined by identifying the transition state (TS) for an H-bond exchange. However, a simpler alternative is to obtain the jump angle from the $O_A - O_d - O_B$ angle immediately after a jump. With sufficient time resolution in the trajectory configurations, this approach is in excellent agreement with results obtained from the TS geometries, as was previously shown.[14] The probability distribution of jump angles, $P(\Delta\theta)$, is calculated in this way from the simulation trajectory, and normalized so that,

$$\int_0^\pi P(\Delta\theta)\ \sin\Delta\theta\ d\Delta\theta = 1 \tag{2.8}$$

The resulting jump angle distributions for the isomeric butanols are shown in Fig. 2.4. The distributions all exhibit a narrow peak around $\Delta\theta \approx 50°$, similar to that found for water and the lower alcohols.[14, 19] In addition, each has a broad peak between $\sim 80° - 150°$, which becomes less pronounced with decreased branching, *i.e.*, the amplitude of this peak follows the trend *tert*-butanol > *sec*-butanol > *iso*-butanol > *n*-butanol. In the case of *n*-butanol the broad peak appears as a decaying tail of the distribution at large jump angles.

The average jump angle, $\langle\Delta\theta\rangle$, is obtained straightforwardly from the distribution as

$$\langle\Delta\theta\rangle = \int_0^\pi \Delta\theta\ P(\Delta\theta)\ \sin\Delta\theta\ d\Delta\theta. \tag{2.9}$$

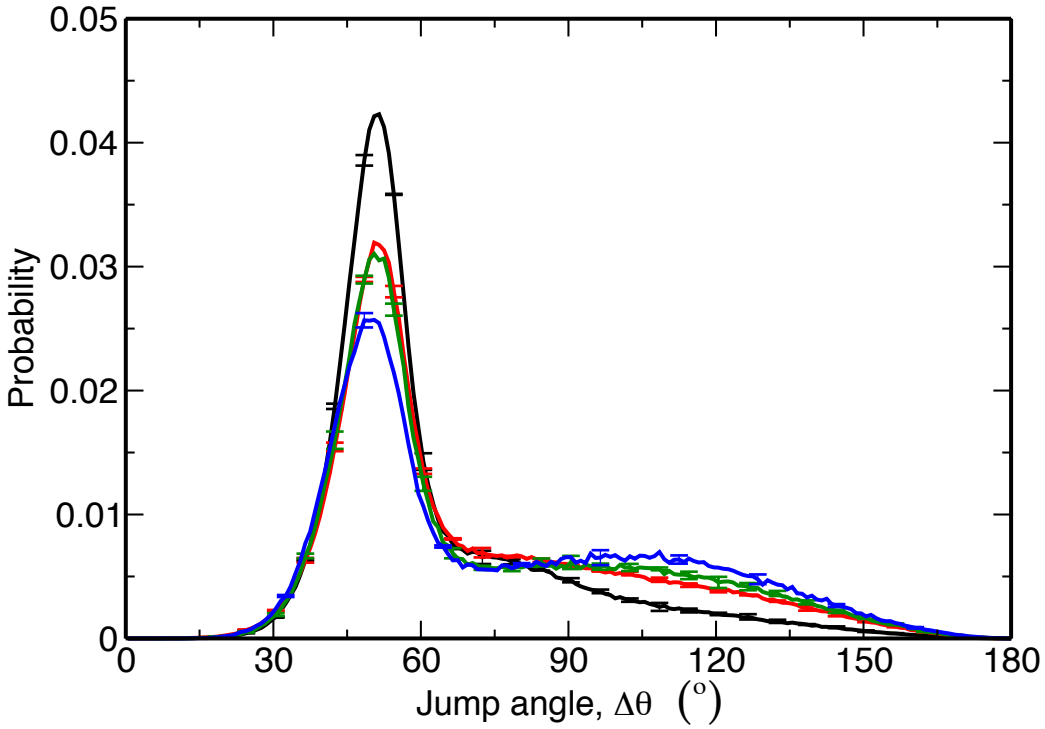

Figure 2.4: Jump angle distribution for hydrogen bond switches in *n*-butanol (black), *iso*-butanol (red), *sec*-butanol (green), and *tert*-butanol (blue).

These values for the jump angle are the ones used in eq. 2.4 in this work. The relative contributions from the sharper, lower jump angle peak and the broader, larger jump angle one give rise to changes in the average jump angle, $\langle \Delta\theta \rangle$ = 64°, 71°, 73°, and 76° for *n*-butanol, *iso*-butanol, *sec*-butanol, and *tert*-butanol, respectively. The average jump angles of these branched isomers of butanol can be compared to those determined for water (68°), methanol (72°), and ethanol (68°).[14, 19] The trend in $\langle \Delta\theta \rangle$ for the alcohols thus shows a decrease with alkyl chain length but an increase with greater steric bulk around the α-carbon.

2.2.2.3 Jump Activation Energy

In order to further probe the differences in H-bond dynamics between the butanol isomers, I have calculated the activation energies for the rate constant for H-bond exchanges, $k_{jump} = 1/\tau_0$. The jump time for each alcohol was calculated at 298 (301 K for *tert*-butanol), 315, 330, and 345 K, and the jump activation energy was determined for each from the slope of a linear fit to $\ln(1/\tau_0)$

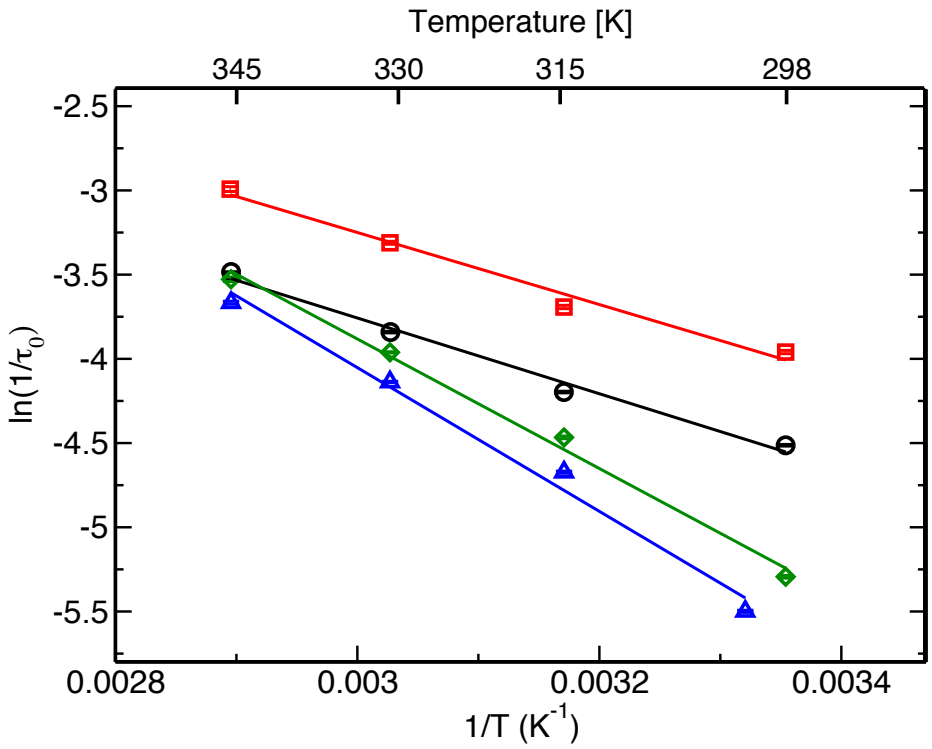

Figure 2.5: Arrhenius plots for the H-bond jump rate constant, $1/\tau_0$, for *n*-butanol (black), *iso*-butanol (red), *sec*-butanol (green), and *tert*-butanol (blue) are shown along with linear fits used to obtain the activation energy. Temperatures for all four alcohols are the same except the lowest simulation temperature of 301 K for *t*-butanol instead of 298 K.

as a function of $1/T$, which is plotted in Fig. 2.5; the temperature dependence of the jump times for each alcohol is well described by an Arrhenius equation. The activation energies for *n*-butanol, *iso*-butanol, *sec*-butanol, and *tert*-butanol are 4.71±0.05, 4.59±0.23, 6.34±0.14, and 6.90±0.04 kcal/mol respectively, and are also listed in Table 2.3. These values indicate that the jump activation energy follows the same general trend as the jump time itself except that the *n*- and *iso*-butanol activation energies are the same within error while *iso*-butanol has a jump time 33% faster than *n*-butanol. Clearly, the activation energy increases with steric bulk on the α-carbon of the alcohol. This trend in the activation energy points to differences in H-bond strength among these alcohols, a result that was not observed for water and the lower alcohols, methanol and ethanol;[14] this issue will be investigated in detail in the Discussion below.

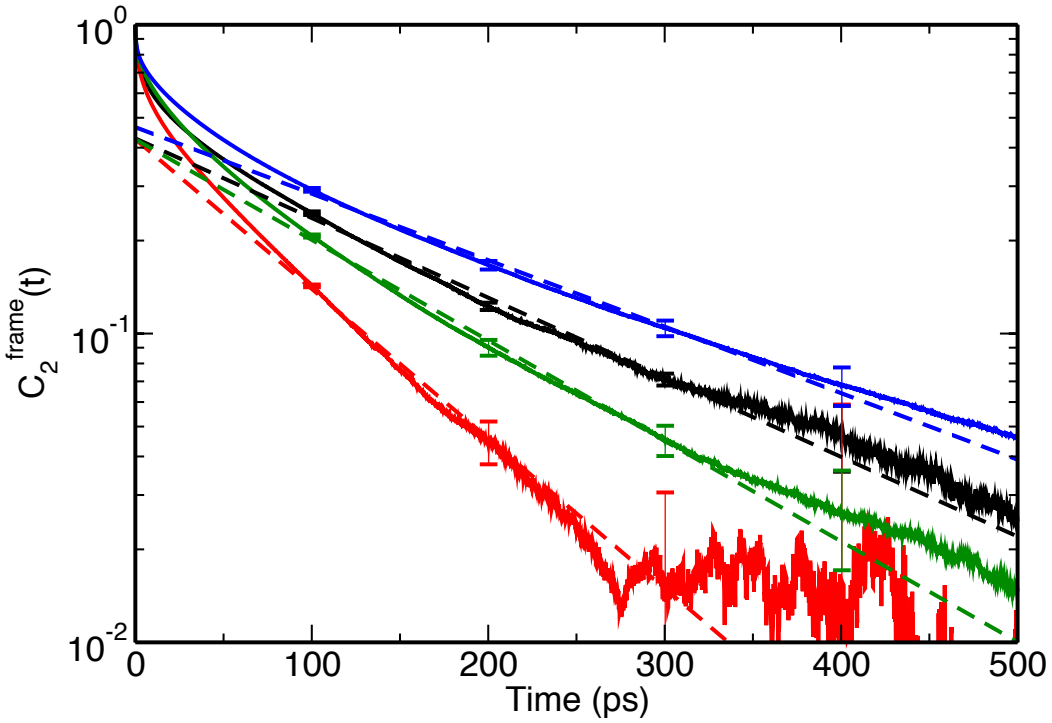

Figure 2.6: Correlation function for intact hydrogen bonds, $C_2^{frame}(t)$ in eq. 2.5, is plotted as a function of time for the butanol isomers. Dashed lines shows the exponential fits to the long-time tail of these correlation functions. Colors are the same as in Fig.2.2.

2.2.2.4 Frame Reorientation

The remaining piece required to determine OH reorientation within the EJM is the frame reorientation time, τ_2^{frame}, measuring the contribution from rotation of intact H-bonds. This frame time is obtained from the long-time decay of the frame reorientation correlation function given in eq. 2.5 and shown for the four butanols in Fig. 2.6. The long-time tail of the autocorrelation function is seen to fit well to a single exponential with timescales given in Table 2.2. The calculated times display a trend in frame reorientation time as: *iso*-butanol < *sec*-butanol < *n*-butanol < *tert*-butanol.

This ordering differs from that of the H-bond jump times only in that *sec*-butanol exhibits faster frame reorientation than *n*-butanol, while *n*-butanol has a faster jump time than *sec*-butanol. It is the contrasting effects of frame and jump reorientation times that result in the virtually identical overall reorientation times determined from the hydroxyl reorientation correlation function for *n*-butanol and *sec*-butanol in Fig. 2.2. In other words, this similarity is due to a fortuitous cancellation

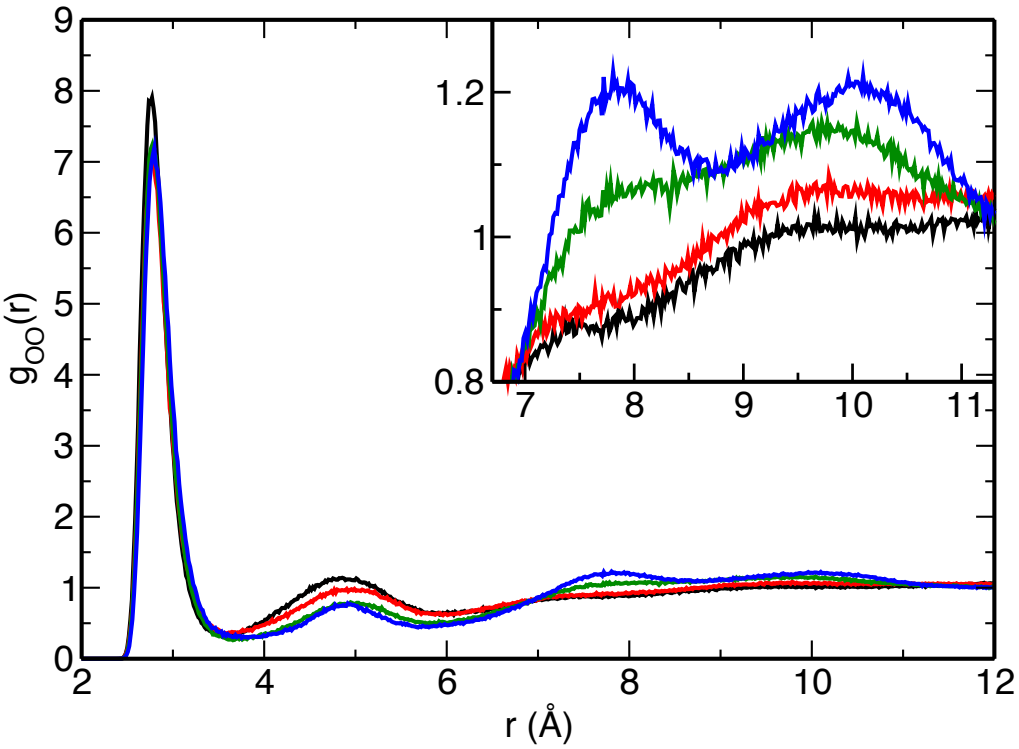

Figure 2.7: Oxygen-oxygen pair distribution functions for the isomers of butanol; the inset shows an expanded view of the third and fourth solvation shells. Colors are the same as in Fig. 2.2.

of the two contributions at room temperature and not a deep similarity in the dynamics.

2.2.3 Liquid Structure

A key difference between the four butanol isomers is the liquid structure. All are naturally networked liquids, but the nature of the H-bond networks is affected by the arrangement of the steric bulk in the alcohol. For example, many studies have shown that *tert*-butanol forms tetramers in H-bonded rings,[68, 71, 83] with the molecules arranged such that the methyl groups point out of the ring. In contrast, the structure of *n*-butanol is dominated by long, H-bonded chains.[39, 73] These differences may certainly have some effect on both the jump and frame reorientation times.

A first approach to examining the liquid structure is through the $O\cdots O$ pair distribution function, $g_{OO}(r)$, which is shown for each butanol isomer in Fig. 2.7. The primary alcohols, *iso*- and *n*-butanol exhibit more structure in the first and second solvation shells, located near $r_{OO} \approx 3$ and

5 Å, respectively, compared to the secondary and tertiary alcohols. As discussed in detail below, this plays a key role in H-bond making and breaking. In contrast, the latter show greater structure in the third and fourth solvation shells, near $r_{OO} \approx 8$ and 10 Å, which is highlighted in the inset of Fig. 2.7. This long range order is a reflection of the larger population of tetrameric rings in *sec*-butanol and *tert*-butanol compared to the primary alcohols; branching at the α-carbon of *sec*-butanol also leads to the formation of ring structures, though to a lesser degree than for *tert*-butanol.

2.2.4 Excluded Volume Effects

The excluded volume effect has been used successfully to explain the origin of the slowdown in jump reorientation, both qualitatively and quantitatively, of water molecules around hydrophobic solutes[33] as well as of the lower alcohols, *i.e.*, methanol and ethanol.[14] The notion is that hydrophobic groups that cannot participate in H-bonding block the approach of potential new acceptors to an OH group, thereby lengthening the jump time. The slowdown factor associated with this effect can be estimated from the excluded volume fraction, f, the fraction of volume that is blocked by atoms that cannot serve as potential acceptors, *e.g.*, alkyl groups on the alcohols, at the transition state for H-bond exchange. Because the steric bulk is arranged differently for the four butanol isomers, it is natural to expect that the excluded volume effect may be at least partly responsible for the variation in jump times among these isomers.

Using the method described in previous studies,[14, 33] we identify the TS for H-bond exchange and calculate the excluded volume fraction resulting from the alkyl atoms of the alcohols blocking potential H-bond acceptors. It is clear from the jump angle distributions that there is an ensemble of transition states with jump angles ranging from $\Delta\theta \sim 40^\circ - 150^\circ$; we consider TS geometries at jump angles ranging from 0° to 180°. In this procedure, a H-bond between molecules is established using the geometric criteria described above. A ring of points is then drawn at the location of potential H-bond switch transition state geometries defined by an $O_d \cdots O_A$ distance, $R^\ddagger = 3.5$ Å, and a given jump angle, $\Delta\theta$. The excluded volume fraction is then calculated as the

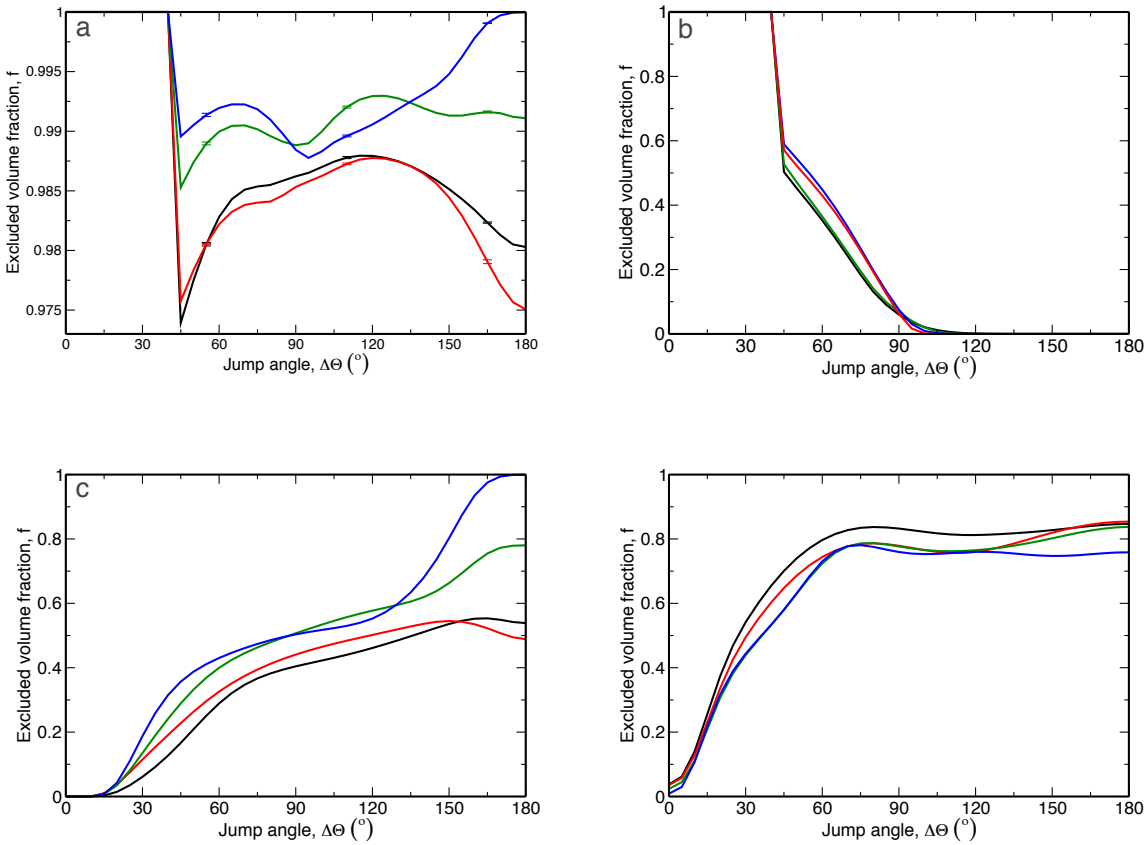

Figure 2.8: (a) Total excluded volume fraction for the four butanols and the ontributions due to non-H-bonding atoms on (b) the butanol that is the original H-bond acceptor, (c) the donor molecule undergoing the H-bond exchange, and (d) other molecules not part of the H-bonded pair. Colors are the same as in Fig. 2.2.

fraction of points on this ring that overlap with a non-H-bonding atom.

The results from this procedure where the excluded volume fraction, f, is shown as a function of jump angle for the four isomers along with the contributions to f from the original H-bond acceptor, the H-bond donor, and all other molecules not part of the original H-bond pair are shown in Figs. 2.8a, b, c, and d respectively. It is clear from Fig. 2.8 that the excluded volume fraction is large in an absolute sense for every butanol; $f \geq 0.97$ for all isomers and all jump angles, consistent with the long jump times. Moreover, f is larger at all jump angles for *sec*- and *tert*-butanol compared to the primary alcohols. For their part, the total excluded volume profile is quite similar for *iso*- and *n*-butanol, with *n*-butanol exhibiting a slightly greater f at intermediate

($\sim 60^\circ - 100^\circ$) and large ($\gtrsim 150^\circ$) jump angles. These trends are in accord with that observed for the jump time (Table 2.2).

These results suggest that the faster reorientation of *iso*-butanol compared to *n*-butanol is partly due to the difference in f for the two alcohols especially at large jump angles where *iso*-butanol has a high jump angle probability as seen in Fig. 2.4. However, because f is close to one, it is difficult to obtain quantitative slowdown factors in the usual way from $1/(1-f)$.

The decomposition of the total f into the components from different molecular types gives insight into the origins of these trends. The excluded volume due to alkyl atoms on the acceptor molecules in Fig. 2.8b shows a trend similar to that from earlier investigation where jumps at angles less than 40° are completely excluded.[14, 19] The exclusion of viable jumps is evident in the jump angle distribution (Fig. 2.4) and is due to the oxygen atom of the acceptor molecules blocking potential H-bonding partners. However, the volume excluded by the original H-bond acceptor is similar for all four isomers.

The contribution to the excluded volume for the H-bond donor does vary significantly among the isomers, with the general trend being that the contribution increases as $n < iso < sec < tert$. This trend is roughly reversed for the contribution from molecules that are not part of the original H-bond pair, though the variation between the isomers is smaller. The opposition of these trends is not unexpected[14] as the volume excluded by the donor also prevents other molecules from approaching the vicinity of the H-bond. Thus, larger excluded volume by the donor leads to less excluded volume by other molecules. It is interesting that the differences in the total f for *n*- and *iso*-butanol arise from a competition between the volume excluded by the donor, which is larger for *iso*-butanol, and that excluded by other molecules, which is larger for *n*-butanol. In addition, there is a distinction between the donor excluded volume for $\Delta\theta \gtrsim 140^\circ$ for the primary alchols, which is flat or decreasing, and for *sec*- and *tert*-butanol, which is increasing; this suggests that these large angles are strongly affected by branching at the α-carbon.

2.3 Discussion

In this Section, we further examine the OH reorientation dynamics of the isomeric butanols and their description by the extended jump model. The emphasis is on identifying the origins of the trends among these alcohols that only vary in the arrangement of the steric bulk.

2.3.1 Accuracy of the Extended Jump Model

It is important to first verify that the EJM provides a quantitative description of the OH reorientation dynamics of the butanols. This can be tested by comparing the reorientation time obtained from the EJM, τ_2^{EJM}, through eq. 2.3 with that obtained directly from the MD simulations of $C_2(t)$ shown in Fig. 2.2, the τ_2 given in Table 2.1. The EJM result is obtained using the jump times and average jump angles to obtain the jump time contribution, τ_2^{jump}, via eq. 2.4 and the frame time contributions from fitting $C_2^{frame}(t)$ in Fig. 2.6. The results are given in Table 2.2 and plotted in Fig. 2.9.

It is clear from Fig. 2.9 that the EJM provides a very good quantitative description of the OH reorientation times in all four alcohols. The poorest agreement is for *n*-butanol, where τ_2^{EJM} is lower than τ_2 by 16%, while for the other alcohols the EJM gives times within 8% of the MD result. These results provide confidence that the OH reorientation of the butanols can be interpreted within the extended jump model, *i.e.*, through the timescales for intact H-bond (frame) reorientation and jumps associated with changes in H-bond partner.

2.3.2 Contributions to the Jump Time

Among the advantages of the EJM is that it provides a framework for developing a molecular understanding of the contributions to the reorientation time. It is interesting to see if the trends in the isomeric butanol jump times, τ_0, can be described by such a decomposition into various factors.

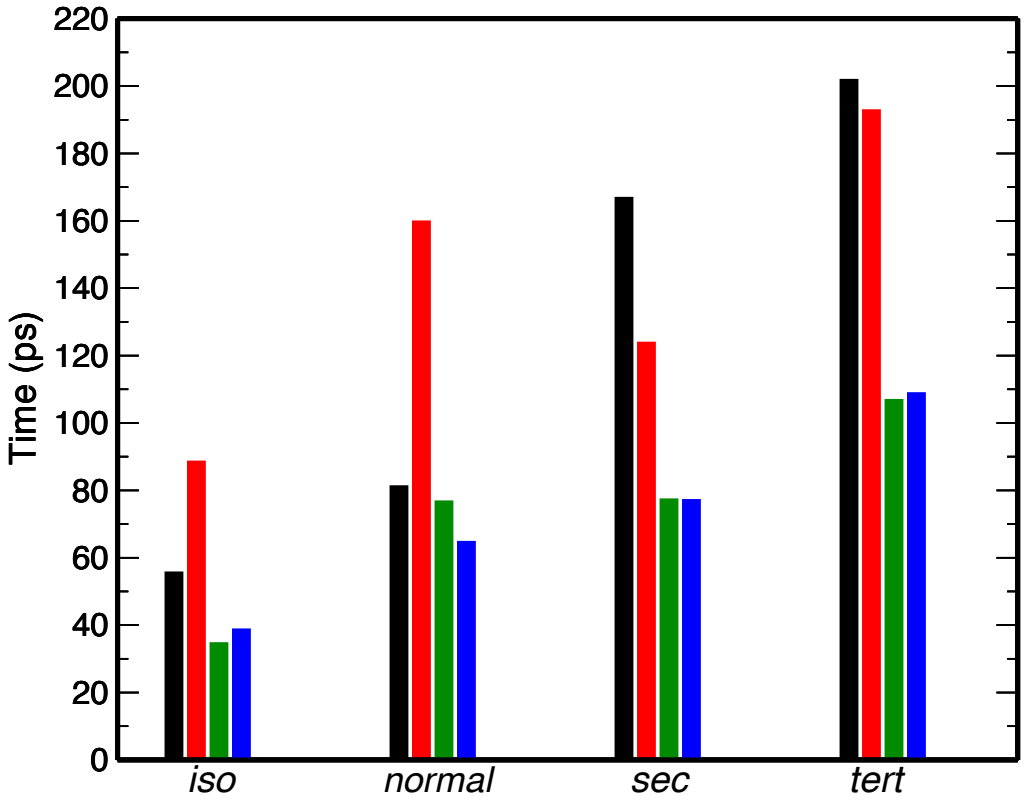

Figure 2.9: Jump (black), and frame times (red) for the isomeric butanols are shown along with the OH reorientation time from the EJM (blue) and exponential fits to $C_2(t)$ (green).

To begin, the jump rate constant can be expressed in a general form as

$$k_{jump}(T) = \frac{1}{\tau_0(T)} = \kappa(T)\,\omega_S\, e^{-\Delta A^{\ddagger}/RT}, \tag{2.10}$$

where κ is the transmission coefficient and $\omega_S \exp(-\Delta A^{\ddagger}/RT)$ is the transition state theory (TST) rate constant. In the latter, ω_S is the attempt frequency and $\Delta A^{\ddagger}$ is the (Helmholtz) free energy barrier for the H-bond exchange. The attempt frequency can be roughly approximated as $\omega_s \approx \tau_{libr}^{-1}$, where τ_{libr} is the librational time, the intermediate timescale for OH reorientation following inertial rotation but before reorientation due to H-bond exchanges. Then, a model can be constructed that gives the relative jump times based on the properties already presented in the Results section above.

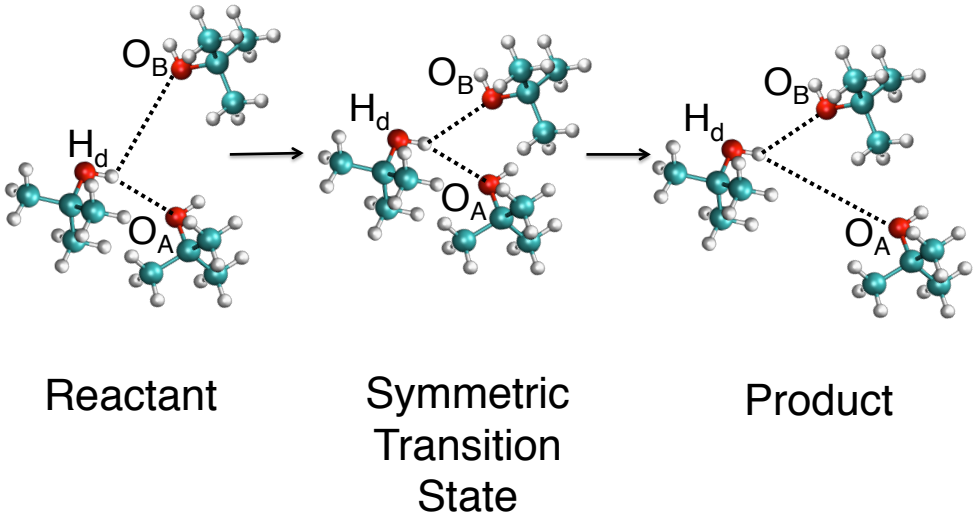

Figure 2.10: Reactant, transition state, and product during H-bond exchange. Figure shows H_d (hydrogen atom of the donor molecule), O_A (oxygen atom of the closest acceptor), O_B (oxygen atom of the next closest acceptor).

2.3.2.1 Free Energy Profiles for H-bond Jumps

We first explore the reaction free energy profile that shows the activation barrier, $\Delta A^{\ddagger}$. We adopt as the reaction coordinate $\Delta R = R_{H_d\cdots O_B} - R_{H_d\cdots O_A}$, where H_d is the hydrogen atom of the donor molecule and O_A and O_B are the oxygen atoms of the initial and final acceptor, respectively. For the purposes of the calculation, the value used for $R_{H_d\cdots O_B}$ is based on the oxygen atom that, aside from the current acceptor oxygen, is closest to H_d. The reaction coordinate is illustrated in Fig. 2.10. From this picture, it can be seen that ΔR implicitly includes the two key elements of an H-bond jump, the approach of the new acceptor with a decrease in $R_{O_d\cdots O_B}$ and the rotation of H_d from O_A to O_B. The probability distribution $p(\Delta R)$ based on this reaction coordinate is calculated from the trajectories and converted into a reaction free energy,

$$\Delta A(\Delta R) = -k_B T \ln p(\Delta R). \tag{2.11}$$

The free energy profile for each of the four butanols is shown in Fig. 2.11. Note that they are all symmetric about the transition state, $\Delta R^{\ddagger} = 0$.

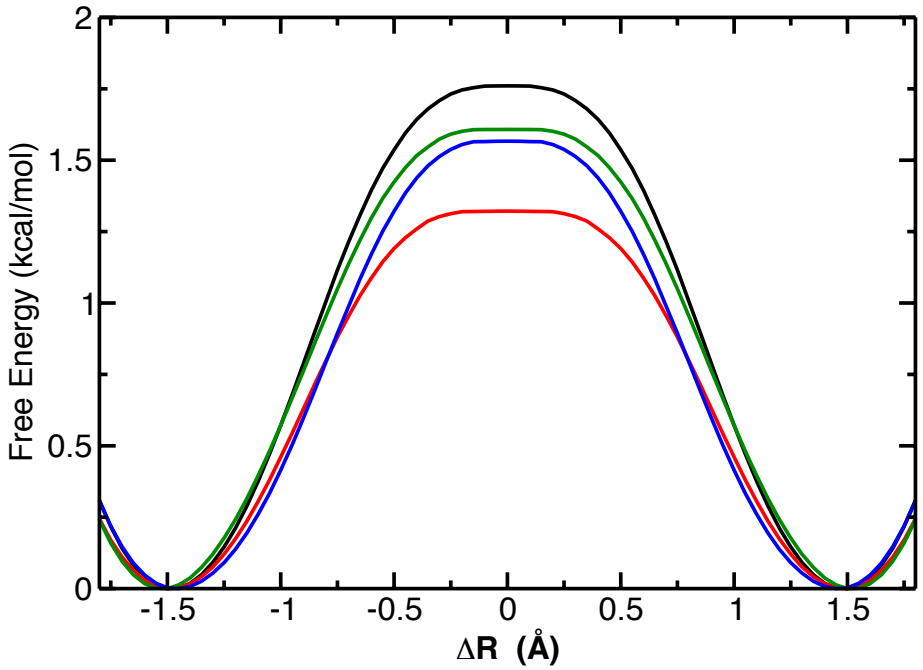

Figure 2.11: Free energy profile for H-bond exchanges as a function of the reaction coordinate, ΔR, shown in Fig. 2.10. Colors are the same as in Fig. 2.2.

The free energy barrier, $\Delta A^{\ddagger} = \Delta A(\Delta R = 0) - \Delta A(\Delta R_0)$ where ΔR_0 is the equilibrium value in the reactant (or, by symmetry, product) state, $\approx \pm 1.5$ Å. (Given the finite histogram bin width, this means that the transition state is effectively identified by $\Delta R < 0.05$ Å). Interestingly, the barrier is found to increase in the order *iso*-, *tert*-, *sec*-, and *n*-butanol; the values are provided in Table 2.3. The magnitude of the free energy barriers, 1.33-1.75 kcal/mol, are consistent with that previously found for water, 2.0 kcal/mol, by a different reaction coordinate.[19] An average $R_{O_A \cdots O_d} = R_{O_B \cdots O_d}$ distance of 3.5 Å is found at the transition state, consistent with previous studies on water and other alcohols.[14, 19] This is similar to the location of the first minimum in $g_{OO}(r)$, shown in Fig. 2.7, that represents the location of the barrier for molecules moving between the first and second solvation shells. This average $R_{O_A \cdots O_d}$ distance is thus indicative of a rate determining step that involves $O_A \cdots O_d$ extension and exchange of H-bond partners between different solvation shells.

The quality of the reaction coordinate can also be estimated from the transmission coefficient, κ. The transmission coefficient was determined by following trajectories from the transition state until they reach H-bonding partners on the product and reactant side of the transition state. The transmission coefficient gives the fraction of reactants that successfully make it to the product side without returning to its initial reactant state. The values of κ calculated this way are given in Table 2.4 and range from 0.26 for *tert*-butanol to 0.48 for *n*-butanol. The absolute values of these transmission coefficients are consistent with the $\kappa = 0.53$ previously found for water at 300 K using a different reaction coordinate,[19] and indicate the present reaction coordinate is a reasonable one. The transmission coefficient values show that transition state recrossing generally increases with steric bulk, $\kappa_n \gtrsim \kappa_{iso} > \kappa_{sec} \gtrsim \kappa_{tert}$. This trend is clearly different from that for the free energy barriers and analysis shows that a TST-based description alone does not fully describe the trends among the butanol isomers. This suggests that dynamical effects are important in addition to the thermodynamics (or, perhaps, that an accurate TST description requires a more sophisticated reaction coordinate than that used here despite its apparent reasonableness.)

2.3.2.2 Contributions to the Jump Activation Energies

One of the interesting observations from the Results is that the activation energy for H-bond jumps increases with steric bulk around the α-carbon of the alcohol (Fig. 2.5). We can examine the origins of this result by noting that the activation energy can be expressed using eq. 2.10:

$$E_a = -R\frac{d(\ln k)}{d(1/T)} = -R\frac{\partial(\ln \kappa)}{\partial(1/T)} - T\frac{\partial(\Delta A^{\ddagger})}{\partial T} + \Delta A^{\ddagger}, \tag{2.12}$$

assuming that ω_s is independent of temperature. We can note that $\Delta A^{\ddagger} = \Delta U^{\ddagger} - T\Delta S^{\ddagger}$, where U and S represent the internal energy and entropy, respectively. It is typically a good approximation to assume that $\Delta U^{\ddagger}$ and $\Delta S^{\ddagger}$ are independent of temperature, in which case it is straightforward to

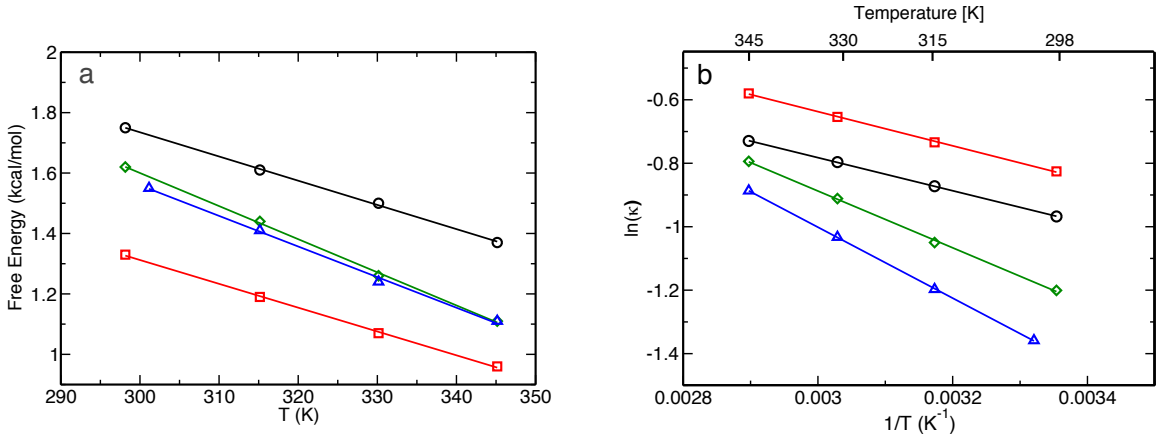

Figure 2.12: Temperature dependence of (a) $\Delta A^{\ddagger}$, and (b) the transmission coefficient, κ for the four butanol isomers. Colors are the same as in Fig. 2.2.

show that the second term in eq. 2.12 is $+T\Delta S^{\ddagger}$ and thus the last two terms sum to $\Delta U^{\ddagger}$ such that

$$E_a = -R\frac{\partial(\ln\kappa)}{\partial(1/T)} + \Delta U^{\ddagger}. \tag{2.13}$$

Using eqs. 2.12 and 2.13, we can decompose the activation energy into contributions that are energetic, entropic, and due to transition state recrossing, *e.g.*, the temperature dependence of κ.

The temperature dependence of the free energy barrier, $\Delta A^{\ddagger}$, is shown in Fig. 2.12a for all four butanols. As expected, the free energy barrier varies linearly with temperature such that the slope yields the activation entropy $\Delta S^{\ddagger}$; the values are given in Table 2.3. The general trend is that the activation entropy is lowest for the the two primary alcohols and higher for the more sterically constrained ones: $\Delta S^{\ddagger}_{n} \approx \Delta S^{\ddagger}_{iso} < \Delta S^{\ddagger}_{tert} \approx \Delta S^{\ddagger}_{sec}$. Similarly, the transmission coefficient is shown in an Arrhenius plot in Fig. 2.12b and the first term in eq. 2.12 determined from the slope for each butanol; the dependence of $\ln\kappa$ on $1/T$ is well described by a straight line and the values for the κ contribution to E_a are given in Table 2.3. The activation energy component due to the temperature dependence of κ (see Table 2.4) is similar for *iso*- and *n*-butanol, 1.04 and 1.07 kcal/mol, respectively). The contributions for *sec*- and *tert*-butanol are roughly twice as large, 1.78 and 2.29 kcal/mol, respectively, suggesting a role for the steric bulk at the α-carbon, as was observed for κ itself.

Table 2.3: Comparison of the results of the activation energy determined from its various components defined in eq. 2.12, from the model based on $g_{OO}(r)$, and calculated directly from the temperature dependence of the jump time, τ_0. Energies are in kcal/mol, $\Delta S^{\ddagger}$ is in cal/(mol K).

Molecule	$\Delta A^{\ddagger}$	$\Delta S^{\ddagger}$	$T\Delta S^{\ddagger}$	$\Delta U^{\ddagger}$	$-R\frac{\partial(\ln\kappa)}{\partial(1/T)}$	E_a (eq. 2.10)	E_a^{OO} (eq. 2.19)	E_a (from τ_0)
n-butanol	1.75	8.0	2.39	4.14	1.04	5.18	5.38	4.71
iso-butanol	1.33	7.9	2.36	3.69	1.07	4.76	4.83	4.59
sec-butanol	1.62	11.0	3.27	4.89	1.78	6.67	6.49	6.34
tert-butanol	1.55	10.3	3.10	4.71	2.29	6.86	6.76	6.90

This data provides a fuller picture of the origins of the differences in H-bond jump activation energy between the four isomers. The estimates of the activation energy from eqs. 2.12 and 2.13 are in reasonable agreement from those calculated directly from the temperature dependence of the jump times and, more importantly, capture the trend among the four isomers; see Table 2.3. Consider first the two primary alcohols, *iso*- and *n*-butanol. They have essentially identical contributions to the activation energy from transition state recrossing (κ) and entropy. A difference is only observed in the internal energy barrier, $\Delta U^{\ddagger}$, which is 0.45 kcal/mol larger for *n*-butanol; this gap is preserved in the activation free energy and activation energy. On the other hand, $\Delta U^{\ddagger}$ is larger for *sec*- and *tert*-butanol compared to the primary alcohols by $\sim 0.75-1.2$ kcal/mol and the temperature dependence of the transmission coefficient makes a greater contribution to E_a with increasing steric bulk, adding another $\sim 0.7-1.2$ kcal/mol. These two effects combine to yield a larger activation energy for the secondary and tertiary alcohols. The transition state recrossing factor is larger for *tert*-butanol compared to *sec*-butanol, so that the higher activation energy for *tert*-butanol can be attributed to this factor.

This analysis shows that the variation in the jump activation energy among the alcohols cannot be interpreted solely as a change in the barrier for H-bond exchanges, but includes a significant dynamical component associated with transition state recrossing. The energetic barrier itself, $\Delta U^{\ddagger}$, has larger values for these alcohols than the 3.5, 3.1, and 3.7 kcal/mol found for water, methanol, and ethanol.[14, 19] Given that the OPLS-AA force field used in these simulations has the same charge on O, H, and the α-carbon group, this result suggests that the *arrangement* of the steric

bulk affects the H-bond strength.

2.3.2.3 Predicting Trends in Jump Times

This insight into the relative activation energies for H-bond jumps for the four isomeric butanols can assist in thinking about the trends in the relative values of the jump times themselves. It is first interesting to examine estimates of the absolute and relative jump times based on eq. 2.10. The required transmission coefficient, κ, and free energy barrier $\Delta A^{\ddagger}$ are given in Tables 2.3 and 2.4, respectively. The attempt frequency, ω_S, is not as easily obtained, but as noted above a first-order estimate is to use the librational frequency, such that $\omega_S \approx \tau_{libr}^{-1}$; the librational times from fitting the $C_2(t)$ correlation functions in Fig. 2.2 are given in Table 2.4. We note that such an approach for water ($\kappa = 0.53$,[19] $\Delta G^{\ddagger}$=2.0 kcal/mol,[19] and $\tau_{libr} \approx 0.15$ ps[84, 85]) gives $\tau_0 \approx 2.3$ ps, in fair agreement with the 3.3 ps calculated from MD simulations.[19] The resulting estimates of τ_0 from eq. 2.10 for the isomeric butanols, while not in quantitative agreement with values obtained from the stable states calculations, Table 2.2, reasonably capture the relative trends among the alcohols.

These trends can be expressed by the ratio of the jump times of *n*-butanol and one of the other isomers, denoted X. Using eq. 2.10, this ratio can be written as

$$\frac{\tau_0^X}{\tau_0^n} = \left(\frac{\kappa_n}{\kappa_X}\right)\left(\frac{\omega_{S,n}}{\omega_{S,X}}\right)\left(e^{-(\Delta U_n^{\ddagger} - \Delta U_X^{\ddagger})/RT}\right)\left(e^{(\Delta S_n^{\ddagger} - \Delta S_X^{\ddagger})/R}\right), \tag{2.14}$$

using $\Delta A^{\ddagger} = \Delta U^{\ddagger} - T\Delta S^{\ddagger}$. The parentheses in eq. 2.14 are included to emphasize the decomposition of this ratio into dynamical, energetic, and entropic contributions that can be individually examined to gain insight into the trend in jump times. (See Table 2.4)

We can first consider the factors leading to the faster H-bond exchange time for *iso*-butanol relative to *n*-butanol. The transmission coefficient and entropic factors are effectively the same for the two isomers. The key differences are found in the attempt frequency estimate and the larger internal energy barrier for *n*-butanol. The latter is the key difference found in the jump activation energy as well; the crude estimate of the attempt frequency likely contributes to the

Table 2.4: Estimates of absolute jump times from eq. 2.10 and their values relative to *n*-butanol (τ_0^X/τ_0^n) are compared to relative jump times estimated from eq. 2.17 and calculated from the Stable States calculations. Contributions to the jump time estimates (κ, τ_{libr}) and relative energetic and entropic contributions in eq. 2.14 are also provided.

[a]From eq. 2.10 using the $\Delta A^{\ddagger}$ in Table 2.3
[b]From eq. 2.17 using thermodynamic quantities derived from the free energy profile resulting from the radial distribution function
[c]From the Stable States picture jump times given in Table 2.2

Molecule (X)	κ	τ_{libr} (ps)	τ_0 [a]	$e^{-(\Delta U_n^{\ddagger}-\Delta U_X^{\ddagger})/RT}$	$e^{(\Delta S_n^{\ddagger}-\Delta S_X^{\ddagger})/R}$	τ_0^X/τ_0^n [b]	τ_0^X/τ_0^n [a]	τ_0^X/τ_0^n [c]
n-butanol	0.48	4.2	167	1	1	1	1	1
iso-butanol	0.44	1.7	37	0.47	1.05	0.4	0.22	0.67
sec-butanol	0.30	4.7	243	3.6	0.22	1.7	1.5	2.1
tert-butanol	0.26	5.6	293	2.6	0.31	1.9	1.8	2.6

underestimation of the ratio of jump times, τ_0^{iso}/τ_0^n by a factor of 3 compared to the stable states result; see Table 2.4.

For the more sterically congested isomers, *sec*- and *tert*-butanol the picture is somewhat different. Those isomers have slightly lower attempt frequencies than *n*-butanol along with larger internal energy barriers and lower transmission coefficients. All three of these factors contribute to longer jump times for these branched alcohols relative to *n*-butanol. The entropic contribution competes with these effects – the activation entropy for *sec*- and *tert*-butanol is larger than that for *n*-butanol, lowering the activation free energy and shortening the jump time. Ultimately, the entropic effect, while significant, is not the dominant one and the branched alcohols have slower H-bond dynamics than the primary alcohols.

2.3.2.4 Predictions Based on Liquid Structure

It is useful to consider the components that contribute to the barrier for H-bond exchange. A useful perspective is to think of an exchange as composed of two parts: 1) the approach of a new acceptor, and 2) the breaking of the current H-bond. The former involves the new acceptor moving from the second solvation shell of the donor molecule to the transition state for H-bond exchange while the latter involves the current acceptor moving from its position in the first solvation shell to

the transition state. The free energy changes associated with these rearrangements can be derived from the $O\cdots O$ radial distribution functions shown in Fig. 2.7 via the associated potential of mean force,

$$\Delta A_{OO}(r) = -k_B T \ln g_{OO}(r). \tag{2.15}$$

Specifically, this gives the activation free energies for H-bond breaking – that for a molecule to move from the first solvation shell represented by the first peak in $g_{OO}(r)$ to the transition state geometry, the $O-O$ distance of which is given by the first local minimum in $g_{OO}(r)$ – and H-bond formation – that for a molecule in the second solvation shell represented by the second peak in $g_{OO}(r)$ to the same transition state geometry. Thus, the free energy barrier for H-bond exchange can be approximated as

$$\Delta A^{\ddagger}_{OO} = \Delta A^{break}_{OO} + \Delta A^{make}_{OO} = [\Delta A_{OO}(r^{\ddagger}) - \Delta A_{OO}(r_1)] + [\Delta A_{OO}(r^{\ddagger}) - \Delta A_{OO}(r_2)], \tag{2.16}$$

where r_1, r_2, and $r^{\ddagger}$ represent the $O-O$ distances in the first and second solvation shells and transition state, respectively.

This free energy barrier can then be used to estimate the jump rate constant as

$$k^{OO}_{jump}(T) = \frac{1}{\tau^{OO}_0(T)} = \kappa(T)\,\omega_S\, e^{-\Delta A^{\ddagger}_{OO}/RT}. \tag{2.17}$$

along with the transmission coefficient and attempt frequency values already given. The relative trends in jump times among the isomeric butanols obtained in this way are given in Table 2.4. They are in reasonable agreement from those determined directly from the MD simulations through the Stable States picture calculation of the jump times. They are also in quite good agreement with the estimates from eq. 2.10 using the relative energetic and entropic contributions from the temperature dependence of the jump times. This supports the simple picture of the free energy barrier as arising from partially breaking the original H-bond and partially making the new H-bond.

These two contributions can be further examined by decomposing them into energetic and

Table 2.5: Comparison of the thermodynamic energies required to partially "break" the original H-bond and partially "make" the new H-bond based on the $O\cdots O$ radial distribution function; see eqs. 2.16 and 2.18. Energies are in kcal/mol.

Molecule	ΔA_{OO}^{break}	ΔU_{OO}^{break}	$T\Delta S_{OO}^{break}$	ΔA_{OO}^{make}	ΔU_{OO}^{make}	$T\Delta S_{OO}^{make}$	$\Delta A_{OO}^{\ddagger}$	$\Delta U_{OO}^{\ddagger}$	$T\Delta S_{OO}^{\ddagger}$
n-butanol	1.86	2.44	0.58	0.72	1.90	1.19	2.58	4.34	1.77
iso-butanol	1.74	2.31	0.56	0.57	1.46	0.89	2.31	3.77	1.45
sec-butanol	2.03	2.69	0.66	0.74	2.02	1.28	2.77	4.71	1.94
tert-butanol	1.86	2.44	0.58	0.58	2.02	1.45	2.44	4.46	2.03

entropic factors as

$$\Delta A_{OO}^{\gamma} = \Delta U_{OO}^{\gamma} - T\Delta S_{OO}^{\gamma}, \tag{2.18}$$

where $\gamma =$ "make" or "break" based on the definitions in eq. 2.16. The results of these decompositions, obtained from the temperature dependence of the ΔA_{OO}^{γ}, are given in Table 2.5. We first note that the estimates of the H-bond exchange free energy barrier are systematically overestimated, ranging from $\Delta A_{OO}^{\ddagger} = 2.31$-$2.77$ kcal/mol compared to those from the free energy profiles in Fig. 2.11 and Table 2.3 of $\Delta A^{\ddagger} = 1.33$-$1.75$ kcal/mol. However, the trends in the activation energy are well captured, even semi-quantitatively, with the main difference being that $\Delta A_{OO}^{\ddagger}$ is larger for *sec*-butanol compared to *n*-butanol, a reversal from the direct results for the free energy barrier. This agreement is quite good considering the simplicity of the underlying model.

The results in Table 2.5 provide insight into the contributions to the free energy. We can first examine the total activation internal energy and entropy obtained from this simple model and compare them to the values from simulation provided in Table 2.3. The model predicts the internal energy barrier nearly quantitatively, such that the trends among the isomers are the same in $\Delta U_{OO}^{\ddagger}$ and $\Delta U^{\ddagger}$ and the values differ by only 0.08-0.20 kcal/mol. This indicates that the the energetics of the H-bond exchange process can be accurately obtained from the radial distribution function, $g_{OO}(r)$. The contributions to this internal energy barrier are smaller but with larger variations for the H-bond making component, *i.e.*, the energy required to bring a new acceptor from the second solvation shell. In particular, ΔU_{OO}^{make} follows the trend *iso* < *n* < *sec* = *tert*, indicative

of mediation by the steric congestion around the H-bond. The energetic barrier for the H-bond breaking component is larger in absolute value but exhibits somewhat smaller changes among the butanol isomers. It increases in the trend *iso* < *n* = *tert* < *sec*. Thus, the energetic barrier for both H-bond making and breaking is largest for *sec*-butanol and smallest for *iso*-butanol, with *tert*-butanol having an intermediate barrier that is slightly larger than that for *n*-butanol. These trends are not straightforwardly rationalized by steric bulk around the α-carbon as others have been, such as κ and E_a; it is possible that the steric effects are modulated by the properties of the H-bond networks, *e.g.*, proportions and sizes of the H-bonded rings and chains, which is currently being investigated.

The excellent agreement between $\Delta U^{\ddagger}_{OO}$ and $\Delta U^{\ddagger}$ combined with the consistent overestimation of the free energy barriers by $\Delta A^{\ddagger}_{OO}$ suggests that the discrepancy arises in the activation entropy. Indeed, $T\Delta S^{\ddagger}_{OO}$ underestimates the calculated $T\Delta S^{\ddagger}$ given in Table 2.3 by $0.62 - 1.33$ kcal/mol, accounting for the bulk of the difference between $\Delta A^{\ddagger}_{OO}$ and $\Delta A^{\ddagger}$. Because these estimates are based on the *OO* radial distribution function alone, this suggests that this simple model is missing an entropic factor due to the disorder of the H atoms at the transition state for H-bond exchange. The trend in $T\Delta S^{\ddagger}_{OO}$ is *iso* < *n* < *sec* $\lesssim$ *tert*, which is only in rough agreement with that observed in the calculated $T\Delta S^{\ddagger}$ where *n* $\approx$ *iso* < *sec* $\approx$ *tert*. These point to avenues for improving this simple model in the future.

In any case, it is interesting to examine the decomposition of the entropic effects predicted from $g_{OO}(r)$. The H-bond breaking component is smaller in magnitude, $T\Delta S^{\ddagger}_{OO} \sim 0.6$ kcal/mol, and is effectively the same for *n*-, *iso*-, and *tert*-butanol and only ~ 0.1 kcal/mol larger for *sec*-butanol, suggesting a small role for the alcohol structure. In contrast, the H-bond making component that is associated with a new acceptor moving in from the second solvation shell is larger, by more than a factor of two in some cases, and exhibits greater variation. The trend in $T\Delta S^{make}_{OO}$ is *iso* < *n* < *sec* < *tert*, indicating that the steric congestion that limits the approach of new acceptors increases the entropy of the transition state for H-bond exchange, serving to lower the free energy barrier.

Finally, we note that the internal energy barriers within this model can be combined with the transition state recrossing component to obtain an estimate of the activation energy for H-bond

exchanges as,

$$E_a^{OO} = -R\frac{\partial(\ln \kappa)}{\partial(1/T)} + \Delta U_{OO}^{\ddagger}. \tag{2.19}$$

The values calculated this way are given in Table 2.3 where they are compared to those directly calculated from the temperature dependence of the jump time and E_a determined from eqs. 2.12 and 2.13. The results are in good agreement with the calculated E_a. The trend among the alcohols, *iso* < *n* < *sec* < *tert*, is correctly predicted and the values are in reasonable quantitative agreement, within 0.24 kcal/mol except for *n*-butanol where E_a^{OO} is 0.67 kcal/mol too large.

These comparisons of the activation energies, free energies, internal energies, and entropies lends credence to the molecular level description of H-bond exchange as a combination of partial H-bond making and breaking determined straightforwardly from $g_{OO}(r)$. The activation entropy is not fully reproduced, due presumably to proton disorder in the H-bond network at the transition state for H-bond exchange, but the accuracy of the predictions of this simple model are encouraging for developing a predictive microscopic picture based on liquid structure. It is important to note however, that the dynamical effects encompassed in κ and ω_S are significant and we do not currently have a model for predicting them without MD simulations, an interesting avenue for future research.

2.3.3 Frame Reorientation Factors

A microscopic theory for frame reorientation does not currently exist, unlike that for jump times. Thus, rationalizing the trends in τ_2^{frame} among the butanols is more challenging. One factor influencing the frame reorientation is presumed to be the viscosity of the liquid. However, the measured values of the viscosity for the butanol isomers are *iso*-butanol ($\eta = 3.435$ cP), *n*-butanol (2.56 cP), *sec*-butanol (3.035 cP), and *tert*-butanol (3.355 cP).[86] The viscosities clearly do not account for the trends in frame reorientation, particularly the fact that *iso*-butanol exhibits the fastest frame reorientation or that *n*-butanol has a longer frame reorientation time than *sec*-butanol. A factor modulating the effect of viscosity is the size and shape of the reorienting H-bonded pair. For these

isomers, the overall size is presumably constant while the shape varies based on the arrangement of the steric bulk for each alcohol. The issue is likely more complicated, however, because the butanols are networked liquids such that H-bonded pairs are not isolated but rather occur in chains of H-bonded molecules or in H-bonded rings (typically tetrameric). The relation between the H-bonded cluster characteristics and the frame reorientation time (as well as jump time) is currently a topic of investigation in our laboratory.

2.4 Summary

A detailed analysis based on molecular dynamics simulations of the OH reorientation in the bulk liquid for four isomeric butanols that differ only in the arrangement of their steric bulk has been presented. These molecules include two primary alcohols, *n*- and *iso*-butanol, the former of which generally exhibits more symptoms of steric congestion due to the greater chain flexibility, along with secondary and tertiary butanols. The OH reorientation dynamics are interpreted within the extended jump model, that assumes two contributions to reorientation, large angle jumps associated with exchanges of H-bonding partners and diffusive, "frame," reorientation of intact H-bonded pairs of molecules. The EJM is shown here to quantitatively describe the OH reorientation for the butanols.

The arrangement of steric bulk matters as the reorientation times, τ_2, vary by as much as a factor of 2.5, with *iso*-butanol exhibiting the fastest dynamics and *tert*-butanol the slowest. The other two isomers, *n*- and *sec*-butanol have identical OH reorientation times, which analysis shows is due to a fortuitous cancellation between faster H-bond exchanges for *n*-butanol and faster frame reorientation for *sec*-butanol.

The long-term goal of work such as this is to develop predictive models for reorientation times in alcohols and other H-bonded systems. To this end, we examined the origins of the trends in OH reorientation, particularly through the H-bond jump time, to gain new physical insight and test such initial models. There are multiple factors that affect the OH reorientation. We note first that the contribution to the reorientation from OH jumps is larger than that due to frame reorientation

for the primary alcohols, but the reverse is true for *sec*- and *tert*-butanol. There is still not a microscopic theory for predicting, even qualitatively, the frame reorientation in H-bonded systems and this remains a topic of ongoing work.

The jump times can be more directly analyzed. However, the timescale for H-bond jumps reflects variations in the transition state recrossing probability, changes in the energetic and entropic barriers for H-bond exchange, and even apparent differences in the attempt frequency for H-bond jumps. We show that the trend in jump time can be reasonably reproduced from the separately calculated free energy barrier and the transmission coefficient using a crude approximation of the attempt frequency based on the librational timescale. Moreover, the activation energy can be described by contributions from the internal energy barrier and a dynamical term associated with the transition state recrossing. Together this analysis shows that the jump times are determined by both energetic and entropic factors, $\Delta U^{\ddagger}$ and $\Delta S^{\ddagger}$, and dynamical ones, κ and ω_S. Thus, no single factor dominates, indicative of the complexity of predicting H-bond dynamics in what might, at first glance, appear to be simple systems.

We show that a simple model based on the *OO* radial distribution function can quantitatively predict the internal energy barriers for H-bond exchanges and semi-quantitatively describe the trends in free energy barrier and activation energy. The notion is that the barrier to a switch of H-bond partners can be described by two components, the partial breaking of the existing H-bond and the partial making of the new H-bond; the contributions of each of these can be estimated from $g_{OO}(r)$. This provides a simple way to understand and predict the barriers to H-bond exchange in the isomeric butanols and, combined with dynamical information from simulation, the relative H-bond jump times. We are currently examining the applicability of this model to other alcohols and H-bonded systems. A remaining challenge is to develop models that describe the dynamical effects associated with transition state recrossing that are important in defining the trends among the butanol isomers. This may require consideration of more sophisticated definitions of the reaction coordinate for H-bond exchanges than that used here, which is in most ways both physically intuitive and reasonable, based, for example, on the transition state recrossing probabilities.

Chapter 3

Removing the Barrier to the Calculation of Activation Energies

It is now common to calculate reaction rate constants using time-correlation functions (TCFs) evaluated from molecular dynamics (MD) simulations that capture reactive trajectories. [81, 82, 87–92] However, further information about the reaction is generally obtained by additional simulations. A key example is the corresponding reaction activation energy that is typically obtained by constructing an Arrhenius plot based on the rate constant, $k(T)$, calculated from simulations at different temperatures. However, this approach belies the fact that the ensemble of reactive trajectories obtained in a MD simulation actually contains considerably more information.

Dellago and Bolhuis[93] have shown that the activation energy can be calculated directly in the context of transition path sampling calculations. They applied it to a model isomerization reaction and others have employed it to determine the activation energy in other systems using transition path sampling.[94–96] In this work, we extend this approach by showing that the activation energy can be obtained directly from the trajectories used to obtain the rate constant at a single temperature using other TCFs. In addition, the same tactic can be applied to calculate the activation energy within quantum mechanical TCF formulations of the reaction rate constant. Thus, these approaches can be implemented in the context of nearly any method for calculating a rate constant. We apply the results to determining the activation energy of the one-dimensional Eckart barrier, described in terms of both classical and quantum mechanics, and the classical hydrogen-bond (H-bond) exchange dynamics in liquid water.

3.1 Time correlation functions and activation energy

3.1.1 Classical

For the purposes of illustration, we first consider the reactive flux (or flux-side) TCF expression for the rate constant:

$$k = \lim_{t \to long} C_{fs}(t) = \lim_{t \to long} \langle F_s(0)\, \theta[s(t) - s^{\ddagger}] \rangle. \tag{3.1}$$

Here a dividing surface at $s = s^{\ddagger}$ is assumed to separate reactants ($s < s^{\ddagger}$) and products ($s > s^{\ddagger}$), $F_s(0) = \delta[s(0) - s^{\ddagger}] v_s(0)$ is the classical flux through the dividing surface at $t = 0$ with v_s the velocity in the reaction coordinate, s, direction, and $\theta(s)$ is the Heaviside step function. The rate constant is given by the "long"-time limit, which indicates times long enough for trajectories initiated at the dividing surface to have reached the products, but shorter than the timescale for the products formed to convert to reactants *via* the reverse reaction.[91]

The activation energy is given by the temperature dependence of the rate constant as

$$E_a = -\frac{d \ln k}{d\beta}, \tag{3.2}$$

which, using Eq. (3.1), gives

$$E_a = -\frac{1}{k} \lim_{t \to long} \frac{dC_{fs}(t)}{d\beta}. \tag{3.3}$$

It is important to note that E_a, which is defined by Eq. (3.2), is distinctly different from the free energy barrier for the reaction. We can write the TCF in a more explicit form as

$$C_{fs}(t) = \frac{1}{Q_r} \mathrm{Tr} \left[e^{-\beta H} F_s(0)\, \theta[s(t) - s^{\ddagger}] \right], \tag{3.4}$$

where Q_r is the reactant partition function, Tr represents an average over all phase space initial conditions, $\beta = 1/k_b T$, and H is the Hamiltonian. Then, it is clear from this expression that $C_{fs}(t)$

depends on temperature, and hence β, only through Q_r and the Boltzmann factor, $e^{-\beta H}$. Thus,

$$\begin{aligned}\frac{dC_{fs}(t)}{d\beta} &= -\frac{1}{Q_r}\mathrm{Tr}\left[e^{-\beta H}H(0)\,F_s(0)\,\theta[s(t)-s^{\ddagger}]\right] \\ &- \frac{d\ln Q_R}{d\beta}C_{fs}(t). \end{aligned} \tag{3.5}$$

However, $-d\ln Q_R/d\beta = \langle H\rangle_r$ is the average reactant energy, which allows the two terms in the above equation to be combined as

$$\frac{dC_{fs}(t)}{d\beta} = -\langle \delta H(0)\,F_s(0)\,\theta[s(t)-s^{\ddagger}]\rangle, \tag{3.6}$$

where $\delta H(0) = H(0) - \langle H\rangle_r$ is the fluctuation of the energy from the average reactant value. This gives the activation energy as

$$E_a = \frac{1}{k}\lim_{t\to long}\langle \delta H(0)\,F_s(0)\,\theta[s(t)-s^{\ddagger}]\rangle. \tag{3.7}$$

This is the result derived previously by Dellago and Bolhuis[93] and it shows that the activation energy can be obtained directly from a TCF that can be evaluated in the same simulation as that used to obtain the rate constant itself. The physical meaning is also clear as what is required is the addition of the energy fluctuation (relative to that of the reactants) at the transition state dividing surface to the reactive flux correlation function, Eq. (3.1). In this way, the present result echoes the interpretation of the activation energy first proposed by Tolman nearly a century ago.[97]

This approach for obtaining direct time correlation function expressions for the activation energy is general. An analogous result can be obtained for the flux-flux TCF,

$$C_{ff}(t) = \langle F_s(0)\,F_s(t)\rangle, \tag{3.8}$$

the integral of which gives the rate constant:

$$k = \int_0^\infty C_{ff}(t)\, dt. \tag{3.9}$$

An expression for the activation energy is obtained, using Eq. (3.2) and the same approach applied above for the flux-side TCF, as

$$E_a = \frac{1}{k} \int_0^\infty \langle \delta H(0)\, F_s(0)\, F_s(t) \rangle\, dt, \tag{3.10}$$

in close analogy to Eq. (3.7).

The same approach can be applied to the rate constant obtained within the Stable-States picture[81, 82] in which the rate constant is obtained from the side-side[90] TCF

$$\begin{aligned} C_{rp}(t) &= \langle n_r(0)\, n_p(t) \rangle, \\ &= \frac{1}{Q_r} \mathrm{Tr} \left[e^{-\beta H}\, \theta[s_r - s(0)]\, \theta[s(t) - s_p] \right], \end{aligned} \tag{3.11}$$

where, r and p represent reactants and products, respectively. Here, $n_r(0) = \theta[s_r - s(0)] = 1$ when the system is in the reactant well at time $t = 0$ and $n_r(0) = 0$ otherwise; $n_p(t) = \theta[s(t) - s_p] = 1$ when the system is in the product well at time t and $n_p(t) = 0$ otherwise. Thus, $C_{rp}(t)$ is zero at $t = 0$ and rises to one with the timescale for converting reactants to products. The rate constant is equal to the time derivative of $C_{rp}(t)$ at times long relative to the timescale for passing between the two dividing surfaces but much shorter than $1/k$.[90, 91] In practice, however, the rate constant is often obtained by the more global description, $1 - C_{rp}(t) = e^{-kt}$, a form that is rigorously obeyed only for times longer than the transit time between the reactant and product regions.[98] In many (but certainly not all) cases, however, this single exponential form is found to be a good approximation for all times and we will adopt it in the following for the purposes of illustration. The rate constant can then be obtained as

$$k^{-1} = \int_0^\infty [1 - C_{rp}(t)]\, dt, \tag{3.12}$$

such that the activation energy is given by

$$E_a = -k \int_0^\infty \frac{dC_{rp}(t)}{d\beta}\, dt. \tag{3.13}$$

Using Eq. (3.11) then gives the activation energy as

$$E_a = k \int_0^\infty \langle \delta H(0)\, n_r(0)\, n_p(t) \rangle\, dt, \tag{3.14}$$

in close correspondence to the results for the reactive flux TCFs derived above.

3.1.2 Quantal

The quantum mechanical reaction rate constant can be obtained by analogous time-correlation functions,[89, 90] including a flux-side TCF,

$$\begin{aligned} k_{qm} &= \lim_{t \to long} \mathscr{C}_{fs}(t) \\ &= \lim_{t \to long} \frac{1}{\mathscr{Q}_r} \mathrm{Tr} \left[e^{-\beta \hat{H}}\, \hat{F}_s\, \hat{\mathscr{P}}(t) \right]. \end{aligned} \tag{3.15}$$

Here, $\mathscr{C}_{fs}(t)$ is the quantum mechanical flux-side TCF, Tr is now a quantum mechanical trace, $\hat{H}$ is the Hamiltonian operator, $\mathscr{Q}_r$ is the quantum mechanical reactant partition function, and $\hat{F}_s = i[\hat{H}, \theta(\hat{s} - s^\ddagger)]/\hbar$ is the flux operator through the dividing surface separating reactants and products. The operator $\hat{\mathscr{P}}(t)$ projects onto reactive space and can take various forms.[89, 90] The one most analogous to Eq. (3.1) is

$$\hat{\mathscr{P}}(t) = e^{i\hat{H}t/\hbar}\, \theta(\hat{s} - s^\ddagger) e^{-i\hat{H}t/\hbar}. \tag{3.16}$$

It is convenient to use the fact that, in the long-time limit, $[\hat{H}, \hat{\mathscr{P}}(t)] = 0$,[90] so that, at long times,

$$\mathscr{C}_{fs}(t) = \frac{1}{\mathscr{Q}_r} \mathrm{Tr} \left[e^{-\beta \hat{H}/2}\, \hat{F}_s\, e^{-\beta \hat{H}/2}\, \hat{\mathscr{P}}(t) \right], \tag{3.17}$$

where $\hat{F}_s(\beta) = e^{-\beta\hat{H}/2}\,\hat{F}_s\,e^{-\beta\hat{H}/2}$ is the Boltzmannized flux operator that is of low rank.[99, 100] It is then straightforward to show that the quantum mechanical activation energy is given by a formula analogous to the classical result in Eq. (3.7):

$$E_{a,qm} = \frac{1}{k_{qm}} \lim_{t\to long} \mathscr{C}_{Hfs}(t), \tag{3.18}$$

where

$$\begin{aligned} \mathscr{C}_{Hfs}(t) &= \frac{1}{2}\langle\, [\delta\hat{H}, \hat{F}_s(\beta)]_+\, \hat{\mathscr{P}}(t)\rangle_{qm}, \\ &= \frac{1}{2}\langle\, \hat{F}_s(\beta)\, [\delta\hat{H}, \hat{\mathscr{P}}(t)]_+\rangle_{qm}, \end{aligned} \tag{3.19}$$

where $\langle\cdot\rangle_{qm} = \mathrm{Tr}[\cdot]/\mathscr{Q}_r$ and $\delta\hat{H} = \hat{H} - \langle\mathscr{E}\rangle_r$. Here, $[\hat{A},\hat{B}]_+ = \hat{A}\hat{B} + \hat{B}\hat{A}$ indicates the anti-commutator and $\langle\mathscr{E}\rangle_r = -\partial \ln \mathscr{Q}_r/\partial\beta$ is the average reactant energy. That is, the activation energy is once again given by a TCF that involves the addition of the fluctuation in the energy at the dividing surface relative to the average reactant energy to the flux-side TCF. The TCF $\mathscr{C}_{Hfs}(t)$ is symmetrized by our use of the Boltzmannized flux operator in Eq. (3.17).

The same approach can be used to derive the activation energy based on the rate constant calculated from the quantum mechanical flux-flux TCF,

$$k_{qm} = \int_0^\infty \mathscr{C}_{ff}(t)\, dt, \tag{3.20}$$

where

$$\mathscr{C}_{ff}(t) = \frac{1}{\mathscr{Q}_r}\,\mathrm{Tr}\left[\hat{F}_s(\beta)\,\hat{F}_s(t)\right]. \tag{3.21}$$

Then the activation energy is

$$\begin{aligned} E_{a,qm} &= \frac{1}{k_{qm}}\int_0^\infty \frac{1}{2}\langle [\delta\hat{H}, \hat{F}_s(\beta)]_+\, \hat{F}_s(t)\rangle_{qm}, \\ &= \frac{1}{k_{qm}}\int_0^\infty \frac{1}{2}\langle \hat{F}_s(\beta)\, [\delta\hat{H}, \hat{F}_s(t)]_+\rangle_{qm}. \end{aligned} \tag{3.22}$$

The integrand is a TCF that we will denote as $\mathscr{C}_{Hff}(t)$.

Finally, the activation energy can be obtained from a side-side TCF formulation of the quantum mechanical rate constant,[90]

$$\begin{aligned} k_{qm} &= \lim_{t\to long} \frac{d}{dt} \mathscr{C}_{ss}(t) \\ &= \lim_{t\to long} \frac{d}{dt} \langle e^{-\beta\hat{H}}\, \theta(s^{\ddagger} - \hat{s})\, \hat{\mathscr{P}}(t) \rangle_{qm}, \end{aligned} \tag{3.23}$$

where $\theta(s^{\ddagger} - \hat{s})$ projects onto the reactant space. Symmetrizing the Boltzmann operator as for $\mathscr{C}_{fs}(t)$ and $\mathscr{C}_{ff}(t)$ above gives the activation energy as

$$E_{a,qm} = \frac{1}{k_{qm}} \lim_{t\to long} \frac{d}{dt} \mathscr{C}_{Hss}(t), \tag{3.24}$$

where

$$\begin{aligned} \mathscr{C}_{Hss}(t) &= \frac{1}{2} \langle\, [\delta\hat{H}, \theta_{\beta}(s^{\ddagger} - \hat{s})]_{+}\, \hat{\mathscr{P}}(t) \rangle_{qm}, \\ &= \frac{1}{2} \langle\, \theta_{\beta}(s^{\ddagger} - \hat{s})\, [\delta\hat{H}, \hat{\mathscr{P}}(t)]_{+} \rangle_{qm}, \end{aligned} \tag{3.25}$$

with $\theta_{\beta}(s^{\ddagger} - \hat{s}) = e^{-\beta\hat{H}/2}\, \theta(s^{\ddagger} - \hat{s})\, e^{-\beta\hat{H}/2}$. We noted above for the classical TCF that the rate constant is equal to the time derivative of $C_{rp}(t)$ for times longer than that required to convert from reactants to products, but we adopted a more global approach to obtaining k from $C_{rp}(t)$. In the quantum mechanical approach described here, the time-derivative is used (as it can be for the classical case as well).

3.2 Eckart barrier

We first consider the application of these approaches to direct calculation of the activation energy for a simple test system. The Eckart barrier potential,

$$V(s) = V_0 \,\mathrm{sech}^2(s/a), \tag{3.26}$$

represents a standard problem in one-dimensional scattering theory; the potential is asymptotically zero at $s \to \pm\infty$ with a barrier of height V_0 at $s = 0$. The classical rate constant is straightforwardly determined analytically as

$$k(T) = \sqrt{\frac{k_b T}{2\pi m}}\, e^{-\beta V_0}, \tag{3.27}$$

which gives the classical activation energy as $E_a = V_0 + k_b T/2$. An exact solution for the quantum mechanical transmission probability is available[101] from which the rate constant and activation energy can be obtained by the appropriate Boltzmann averaging.

3.2.1 Classical Dynamics

For this case we present results for the flux-side approach to calculating the rate constant and activation energy. The flux-side time correlation function, $C_{fs}(t)$, is shown for three different choices of the dividing surface, $s^\ddagger$, in Fig. 3.1. In each calculation, 5×10^6 trajectories are initiated from $s(0) = s^\ddagger$ and propagated using the velocity Verlet algorithm at a constant energy that is determined for each trajectory by initial velocities selected from a Boltzmann distribution. These trajectories were then used to evaluate C_{fs} and $C_{Hfs}(t) = \langle \delta H(0)\, F_s(0)\, \theta[s(t) - s^\ddagger] \rangle$. In the present simulations we took $V_0 = 2.5 k_b T$, $a = 1$ Å, and $m = 1$ g/mol; this gives $k = 5163$ cm molecule^{-1} s^{-1} and $E_a = 1.79$ kcal/mol at 300 K.

Choosing the dividing surface at $s^\ddagger = 0$, *i.e.*, at the top of the barrier, yields $C_{fs}(t) = k$ for all $t > 0$ because there is no recrossing for this simple one-dimensional potential. This is illustrated in Fig. 3.1. For $s^\ddagger = -2.5$ or -5 Å, however, there is significant recrossing of the (poorly chosen)

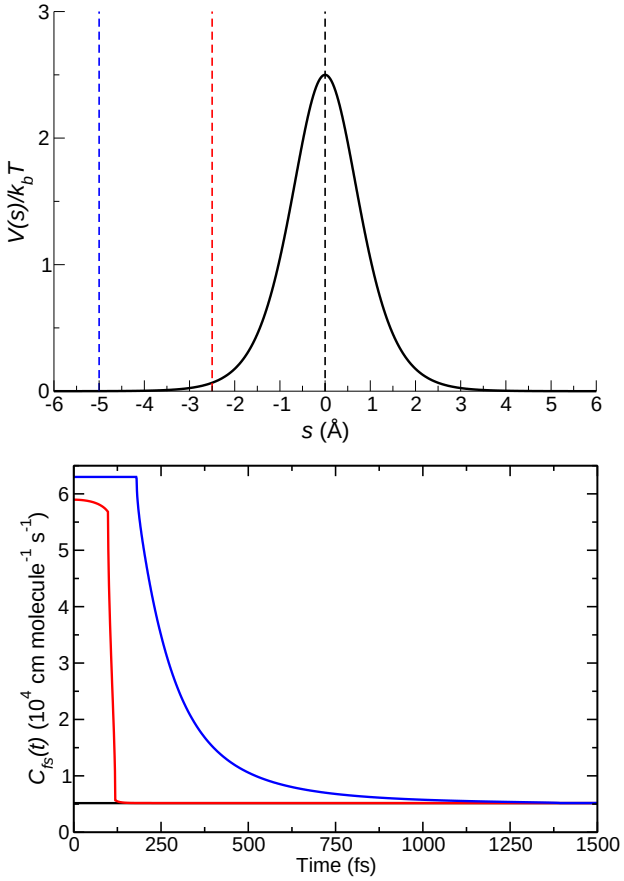

Figure 3.1: Top: The Eckart barrier potential is plotted (solid black line) and the three dividing surfaces, $s^{\ddagger} = 0$, -2.5, and -5 Å are shown (vertical dashed black, red, and blue lines, respectively). Bottom: The flux-side TCF, $C_{fs}(t)$, for the one-dimensional Eckart barrier is plotted against time for three choices of the dividing surface: $s^{\ddagger} = 0$, -2.5, and -5 Å (shown as black, red, and blue lines, respectively).

dividing surface, which can be seen in Fig. 3.1 by the large initial flux followed by recrossing dynamics that lower the value of $C_{fs}(t)$ at longer times. The recrossing naturally occurs at shorter times for $s^{\ddagger} = -2.5$ Å compared to -5 Å as the trajectories reach (and are reflected by) the barrier more quickly. The rate constant, given by the long-time limit of $C_{fs}(t)$ is, however, independent of the choice of the dividing surface.

The activation energy can be calculated from the same trajectories from Eq. (3.7), *i.e.*, it is the long-time limit of $C_{Hfs}(t)/k$, which is plotted in Fig. 3.2 for the three choices of dividing surface location. As with the flux-side TCF itself, $C_{Hfs}(t)$ exhibits different dynamics depending on the dividing surface. In the absence of recrossing ($s^{\ddagger} = 0$) it takes a constant value for all

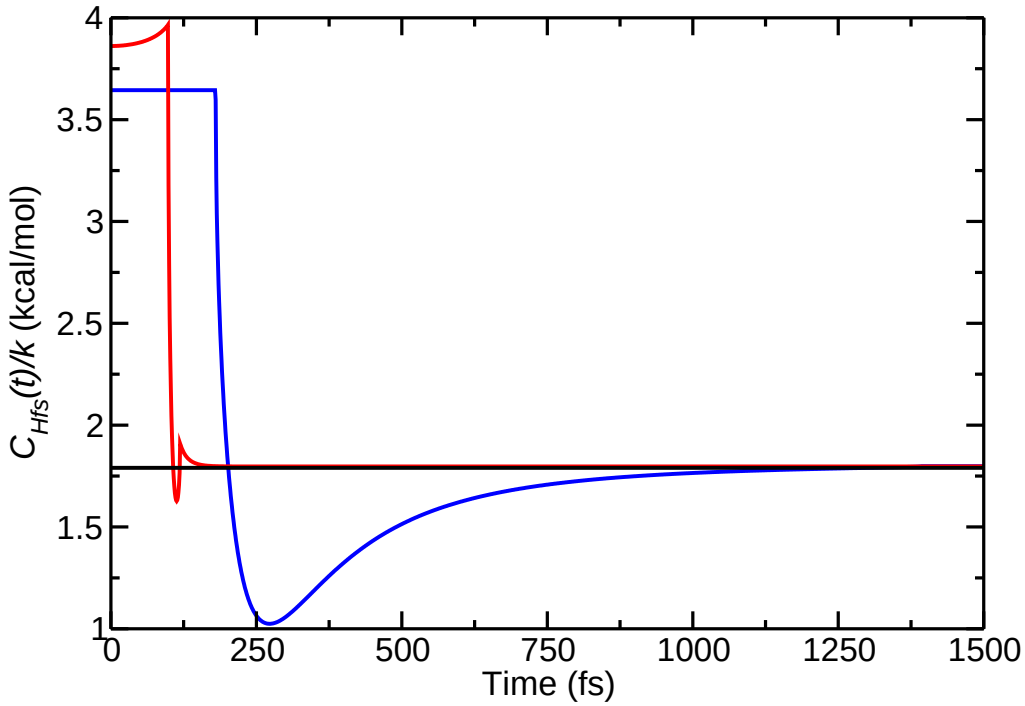

Figure 3.2: $C_{Hfs}(t)/k$ for the one-dimensional Eckart barrier is plotted against time for three choices of the dividing surface: $s^{\ddagger} = 0$, -2.5, and -5 Å (shown as black, red, and blue lines, respectively). Normalization by the rate constant in this way means this TCF has a long-time limit equal to the activation energy.

$t > 0$. In contrast, for $s^{\ddagger} = -2.5$ and -5 Å, the dividing surface recrossing leads to dynamics on shorter timescales. Specifically, $C_{Hfs}(t)/k$ is constant at a value of $\langle H \rangle_r = V(s^{\ddagger}) + k_b T/2$ at short times before the trajectories reach the barrier, are reflected, and recross the dividing surface. The trajectories with the highest kinetic energies recross the dividing surface first, leading to a dip in $C_{Hfs}(t)/k$, which then rises steadily to the final value of E_a as the trajectories with lower kinetic energy also recross at longer times. It is noteworthy, however, that the activation energy converges on approximately the same timescale as the rate constant. In addition, the same activation energy of 1.79 kcal/mol is obtained for all choices of $s^{\ddagger}$, in excellent agreement with the analytical result given above.

3.2.2 Quantum Dynamics

To illustrate the direct calculation of the quantum mechanical activation energy for the Eckart barrier, standard parameters intended to mimic the H+H_2 reaction are used, $V_0 = 0.425$ eV, $a = 1$ a.u. $= 0.529$ Å, and $m = 1061$ a.u. $= 0.5820$ g/mol. The rate constant and activation energy are obtained from the flux-flux TCF formulation, Eqs. (3.20)-(3.22). Practically, the low-rank of the Boltzmannized flux operator is used to advantage by finding the two non-zero eigenvalues and eigenvectors,

$$\hat{F}_s(\beta)\,|f_n\rangle = f_n\,|f_n\rangle, \tag{3.28}$$

to provide a basis for evaluating the quantum mechanical trace. Then, the flux-flux TCFs $\mathscr{C}_{ff}(t)$ and $\mathscr{C}_{Hff}(t)$ are obtained as

$$\mathscr{C}_{ff}(t) = \frac{1}{\mathscr{Q}_r}\sum_n f_n\,\langle f_n|\,\hat{F}_s(t)\,|f_n\rangle, \tag{3.29}$$

and

$$\mathscr{C}_{Hff}(t) = \frac{1}{2\mathscr{Q}_r}\sum_n f_n\,\langle f_n|\,[\hat{H},\hat{F}_s(t)]_+\,|f_n\rangle. \tag{3.30}$$

Note that $\langle f_n|\,\hat{F}_s(t)\,|f_n\rangle = \langle f_n(t)|\,\hat{F}_s\,|f_n(t)\rangle$ so that the rate constant evaluation involves the time propagation of the eigenvectors $|f_n\rangle$ for which $f_n \neq 0$. The only additional work required to obtained $C_{Hff}(t)$, and hence $E_{a,qm}$, is a single additional Hamiltonian multiplication since $\langle f_n|\,[\hat{H},\hat{F}_s(t)]_+\,|f_n\rangle = \langle f_n(t)|\,\hat{H}\hat{F}_s + \hat{F}_s\hat{H}\,|f_n(t)\rangle$.

The calculations were completed using a sinc-function discrete variable representation basis[102] between $s = -10$ and 10 a.u. with a quartic complex absorbing potential starting at $|s| = 6$ a.u. with a height of 8 eV. The grid spacing was taken to be 15 times the thermal de Broglie wavelength, giving 67 grid points at 300 K and 117 at 900 K. The Boltzmannized flux eigenvalues and eigenvectors were obtained using a Lanczos algorithm[103] and the time evolution was carried out with a split-operator propagator with a timestep of 0.127 fs.

The results for the activation energy, $E_{a,qm}$ as a function of temperature are given in Fig. 3.3 and

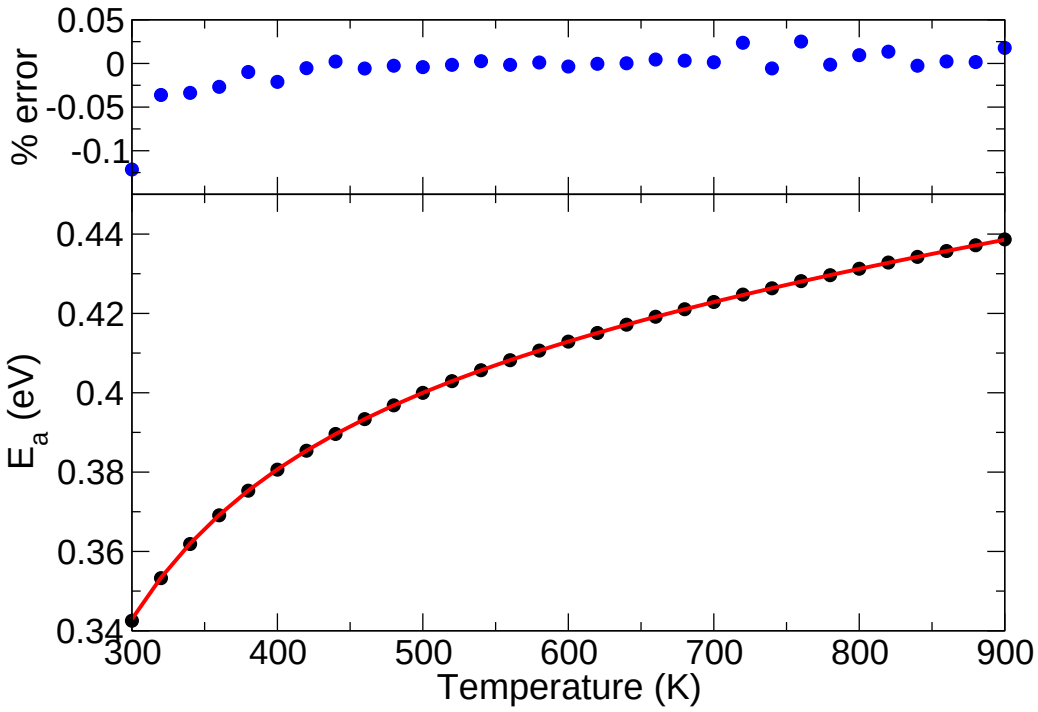

Figure 3.3: Bottom: The activation energy for the Eckart barrier calculated using Eq. (3.22) (black circles) is plotted as a function of temperature and compared with the exact activation energy (red line). Top: The percent-error at each temperature is shown (blue circles).

compared to the exact results; the error is also shown. The activation energy rises monotonically with temperature beginning from a value below the Eckart potential barrier height ($V_0 = 0.425$ eV). This reduced activation energy can be attributed to quantum mechanical tunneling which occurs due to the low mass used in the calculations. At higher temperatures the activation energy slightly exceeds V_0. The activation energy calculated directly from Eq. (3.22) is in excellent agreement with the exact values, differing by less than 0.15% for all temperatures.

3.3 H-bond exchanges in water

The final application we consider is the rate constant associated with H-bond exchanges, or “jumps," between different H-bond acceptors in liquid water.[104, 105] Here, the Stable-States time correlation function, Eq. (3.11), is evaluated from a single long trajectory that captures a large number of these events. Specifically, TCFs are calculated from a 1 ns NVT classical MD simulation of 343

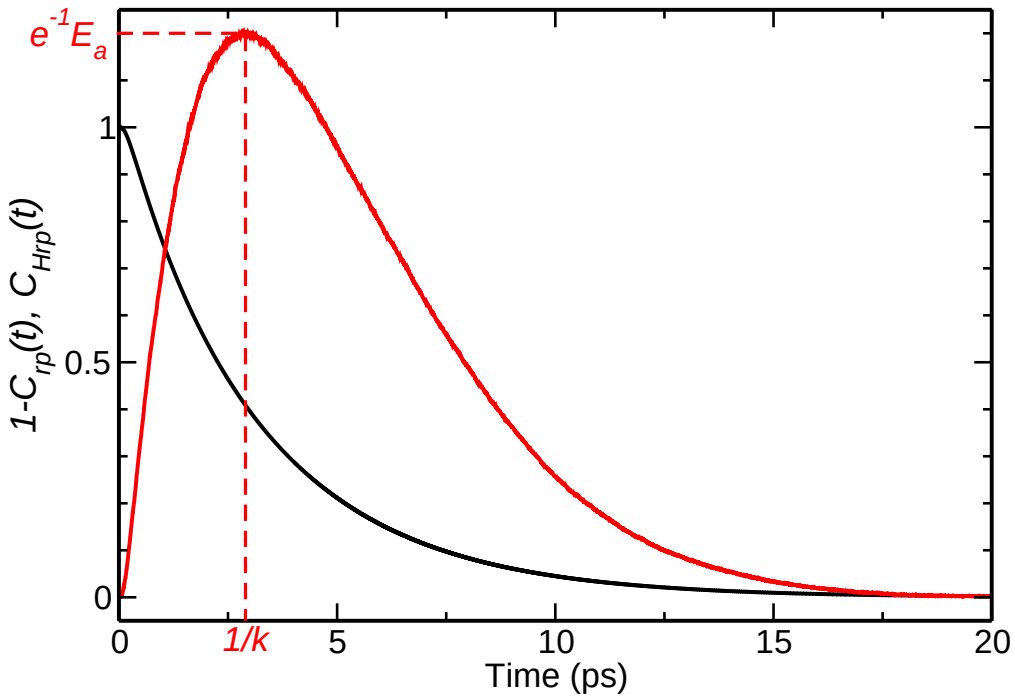

Figure 3.4: The Stable-States or side-side, reactive TCFs $1-C_{rp}(t)$ (black line) and $C_{Hrp}(t)$ (red line) are plotted as a function of time for H-bond exchanges in liquid water.

water molecules carried out using the LAMMPS software[74, 106] with the SPC/E water force field.[107] The integration timestep was 1 fs and configurations were saved every 2 fs. Coulombic and Lennard-Jones interactions were evaluated within a cut-off radius of 10.5 Å. The long-range electrostatic interactions were included using three-dimensional periodic boundary conditions and an Ewald summation with a tolerance of 1×10^{-4}. The production stage was preceded by 1 ps velocity rescaling and 0.25 ns NVT equilibration periods. For this system, the reactant state is taken to be a H-bond between a given OH donor and a particular O atom H-bond acceptor and the product state is the same OH H-bonded to a different acceptor; an H-bond is defined geometrically as $R_{OO}\leq 3.5$ Å, $r_{H\cdots O}\leq 2.45$ Å, and $\theta_{OOH}\leq 20^{\circ}$ and absorbing boundary conditions are used in the product state.

In Fig. 3.4, we show the reactive time correlation function, $1-C_{rp}(t)$, which decays at longer times with a time constant of $\tau=1/k=3.1$ ps, which is consistent with previous determinations of the H-bond jump time in water.[14, 105] Also shown is the $C_{Hrp}(t)\equiv\langle\delta H(0)\,n_r(0)\,n_p(t)\rangle$ TCF

that gives the activation energy *via* Eq. (3.14). The shape of this $C_{Hrp}(t)$ correlation function can be examined by considering the temperature- and time-dependence of $C_{rp}(t)$. It is straightforward to show that if the approximate relationship $1 - C_{rp}(t) \simeq e^{-kt}$ holds, then

$$\frac{d}{d\beta}[1 - C_{rp}(t)] = \langle \delta H(0)\, n_r(0)\, n_p(t) \rangle \simeq -t \frac{dk}{d\beta} e^{-kt}. \tag{3.31}$$

This indicates that $C_{Hrp}(t)$ is generally positive (assuming k decreases with increasing β, *i.e.*, decreasing T). Moreover, it initially increases with time before decreasing back to zero, with a maximum occurring at $t_{max} = 1/k$. The value of $C_{Hrp}(t)$ at this maximum is easily seen to be

$$C_{Hrp}(t_{max}) \simeq -\frac{1}{k} e^{-1} \frac{dk}{d\beta} = e^{-1} E_a. \tag{3.32}$$

Thus, both the rate constant and the activation energy can be directly, if approximately, obtained from the $\langle \delta H(0)\, n_r(0)\, n_p(t) \rangle$ correlation function using the location and magnitude of the maximum value. The $C_{Hrp}(t)$ in Fig. 3.4 has a maximum of 1.19 kcal/mol at $1/k \simeq 2.9$ ps, yielding $E_a \simeq 3.2$ kcal/mol. This is in good agreement with the rate constant given above and the activation energy value of $E_a = 2.9 \pm 0.1$ kcal/mol derived from the temperature dependence of the H-bond jump time in water obtained from separate simulations at multiple temperatures.

3.4 Summary

We have shown that the activation energy for a chemical reaction can be calculated directly within nearly any approach for calculating the rate constant. Because the technique represents a simple extension of standard TCF rate constant computations, it is easily implemented in current classical *and* quantum mechanical methodologies. More generally, these approaches illustrate how additional information can be directly extracted from reactive trajectories (or quantum dynamics) obtained in simulations.

Chapter 4

A "Universal" Spectroscopic Map for the OH Stretching Mode in Alcohols

Alcohols are of wide importance in chemistry. They are commonly used as solvents for chemical reactions and separations because of their ability to hydrogen-bond (H-bond), their miscibility with other solvents, and the potential for tunability of their properties through modification of the alkyl group.[108] Alcohols are also interesting from a fundamental perspective due to the importance of the H-bonding network in their structure and dynamics.[28] They can be thought of as a series of H-bonding liquids with the structure R–OH in which the quantity and arrangement of the steric bulk, R, can be varied from R = H (water) to large linear and branched alkyl groups. In this context, the dynamics of alcohols can be treated with many of the same theoretical frameworks that are used for water. It has been previously shown that OH reorientation in alcohols can be described by an extended jump model[14, 109] that was originally developed for water.[104, 105] However, the steric bulk gives rise to different mechanisms, *i.e.*, the dominant contribution to OH reorientation in water is "jumps" between H-bond partners but it is the rotation of intact, H-bonded partners in methanol and ethanol.[14] Furthermore, the arrangement of the steric bulk, not just the total quantity, also has a significant impact on the reorientation dynamics timescales and mechanism, due primarily to entropic effects.[109]

The vibrational spectroscopy of liquid alcohols in the OH stretching region has been the subject of numerous experimental studies,[3, 8, 28, 50, 110–125] but has received comparatively little theoretical attention.[3, 26, 126–128] This situation sits in strong contrast to the case of liquid water where linear and nonlinear vibrational spectroscopies have advanced in concert with theoretical

descriptions to advance our understanding of its structure and dynamics.[129] This indicates the significant potential that exists to analogously expand our insight into the behavior of alcohols. Among the many approaches that have been applied to describe the vibrational spectroscopy of water is the empirical map approach developed by Skinner and co-workers.[1, 2, 130–133] This method provides a balance between rigor and computational cost by identifying a quantity (usually an electric field component) that is easily accessed from a molecular dynamics trajectory but is strongly correlated with the vibrational frequency. The correlation is quantitatively established by a (relatively) small number of electronic structure calculations.

In this chapter, an empirical spectroscopic map is developed for the OH stretching frequencies of monohydroxy alcohols. Specifically, density functional theory calculations are carried out for methanol, ethanol, *n*-propanol, and *n*-butanol and maps are constructed based on the results for each alcohol separately and the collected data from all alcohols (a "universal" map). Within each map the transition frequencies, dipole derivative, and position matrix elements required to calculate the linear and nonlinear IR spectra are expressed in terms of the electric field on the hydrogen atom of interest along the OH bond due to the liquid. The universal map is compared to those derived individually for each alcohol as well as a standard map for water.[1, 2]

The remainder of this chapter is organized as follows. First, the details of the MD simulations and the approach to deriving the empirical maps are described. Second, the derived maps are presented and simulations of the linear IR spectra of the four alcohols are shown and compared to experimental spectra,[3] where available, along with results from other maps. The spectra are discussed in the context of the structure and dynamics of the liquids. Third, the 2D-IR spectra simulations are presented and discussed. Finally, some concluding remarks and comments are offered on future opportunities and challenges for these approaches.

4.1 Simulation Details

4.1.1 Molecular Dynamics Simulations

Classical molecular dynamics (MD) simulations were carried out using the LAMMPS software.[74] The optimized potentials for liquid simulations-all atom (OPLS-AA) force field[134, 135] was used to describe the interactions for all four alcohols. The intermolecular potential involves Lennard-Jones interactions for all non-hydrogen atoms along with Coulombic interactions for all atoms. A spherical cuttoff of 12.0 Å was used for all interactions; the long-range electrostatics were included using three-dimensional periodic boundary conditions and an Ewald summation with a tolerance of 1×10^{-4}. The Lennard-Jones and Coulombic interactions between sites on the same molecule were neglected for sites separated by one or two bonds, weighted by half for those separated by three bonds, and fully included otherwise. The molecules are fully flexible with an intramolecular potential that is based on harmonic bonds and angles along with the OPLS dihedral potential.[135] For all four alcohols, 40 ns trajectories with an initial 1 ns equilibration period were propagated for each alcohol and configurations were saved every 100 fs. The temperature is maintained by velocity rescaling during the equilibration period and a Nosé-Hoover thermostat[136, 137] with a 100 fs time constant was used during the production stage. These trajectories were used to build the empirical maps.

In order to calculate the infrared spectra the same simulation parameters mentioned above were used but finer time resolution is required. In these simulations the equilibriated trajectories from the 40 ns runs were used as the starting configurations from which a 1 ns trajectory was propagated for each alcohol with configurations saved every 2 fs.

4.1.2 Building the Empirical Spectroscopic Map

Individual and a common, "universal," spectroscopic map are developed for the first four linear alcohols from methanol to butanol using the approach developed for water by Skinner and co-workers.[130, 133] Both OH and OD stretches were considered. Resonant vibration-vibration

coupling between OH modes on different molecules can influence the spectra as has been found in water[2, 138] and methanol.[3, 8, 118, 126] This problem is avoided experimentally by isotopic dilution, *e.g.*, using CH_3OH dilute in CH_3OD and analogously for the OD stretch. Our simulations do not include any effect of intermolecular vibrational coupling and are thus intended to represent these isotopically isolated OH and OD stretching modes.

The procedure is as follows. From the 40 ns classical MD trajectory described above, a molecule was chosen randomly from snapshots 5 ps apart. A cluster of molecules centered on this randomly chosen molecule was then extracted. The number of such clusters for all alcohols were, 500 configurations for methanol, 250 each for ethanol and propanol, and 150 for butanol, making a total of 1150 different configurations in all.

Each cluster contains an inner sphere of molecules where the atoms are explicitly represented and an outer sphere where the atoms are represented as point charges in the electronic structure calculations. The inner sphere of methanol and ethanol contained the eight closest molecules based on the distance from the hydrogen atom in the OH bond of interest to the O atom of the surrounding alcohol molecules. The propanol and butanol clusters involved had seven solvating molecules. An outer sphere radius of 8.5 Å was used for all four alcohols. These values were obtained by converging the transition frequency and transition dipole moment obtained for sample clusters of each of the alcohols by increasing the explicit cluster size and the outer sphere radius.

The clusters were used to obtain density functional theory (DFT)-based values for the OH (and OD) stretching frequency of the central alcohol for all 1150 configurations. In order to compute the dipole moment derivative and anharmonic potential energy curve, the OH bond of the central alcohol molecule in each cluster was stretched from 0.6372 to 1.8272 Å in intervals of 0.085 Å, leading to 15 single-point energy DFT calculations. We verified that this was sufficient by comparison with calculations for methanol in which the OH bond was stretched in intervals of 0.02 Å, giving 60 grid points. Individual molecules were treated as pseudodiatomics,[130, 133] with H(D) acting as one half of the diatomic and the OR group, where R is the different alkyl groups on the alcohol, being the other half of the diatomic.

The potential energy curves for the OH (OD) stretch in these alcohols were determined from these DFT calculations using the B3LYP functional[139] and a 6-311++G** basis set.[140] The DFT calculations were carried out using the NWCHEM package.[141] The one-dimensional potential energy curve derived from the DFT calculations was fit to an 8th-order polynomial. This fit was used as the potential in a sinc-function discrete variable representation[102] (DVR) calculation to determine the vibrational frequencies, eigenfunctions, and position matrix elements for the $0 \rightarrow 1$ and $1 \rightarrow 2$ transitions for the OH (OD) stretch in the alcohols. The grid in the DVR calculation was determined using a potential cut-off (V_{cut}) of 3 eV using ten grid points per deBroglie wavelength. This gave between 40-60 points in the DVR grid for OH and 55-85 for OD. In addition, we calculated a scaling factor for the vibrational frequencies of the clusters by comparing the calculated gas phase vibrational frequency for all four alcohols to its corresponding experimental value. These scaling factors were used to scale the DVR-calculated vibrational frequencies of the OH (OD) stretch in the clusters. Experimental gas-phase values for the OH stretching frequency of methanol, ethanol, propanol, and butanol were obtained from the NIST Chemistry WebBook,[142, 143] while corresponding values were calculated using anharmonic potential energy curves for an isolated alcohol obtained from B3LYP/6-311++G** DFT calculations followed by a DVR calculation of the frequencies. The scaling factors (Experiment/Theory) are 1.0158, 1.0209, 1.014, and 1.0229 for methanol, ethanol, propanol, and butanol, respectively. In order to compute the dipole derivative for the stretching vibration at the equilibrium bond length, we took a numerical derivative of values of the dipole moments at the equilibrium bond distance derived from the DFT calculations.[133]

4.2 Results

4.2.1 The Empirical Spectroscopic Map

In Table 4.1, we present the universal empirical map equations for ω_{01}, ω_{12}, x_{01}, x_{12}, and μ' for the OH and OD stretching modes in the alcohols. Note that by "universal" we mean that the data

Table 4.1: "Universal" empirical map equations for OH (OD) transition frequencies (ω_{nm}), coordinate matrix elements (x_{nm}), and dipole derivatives (μ') for alcohols. Frequencies are in cm^{-1}, while coordinates, the dipole derivative, and the electric field ($\mathscr{E}$) are in atomic units.

Map Equation for OH	RMSD
$\omega_{01} = 3744 - 7239\,\mathscr{E} - 52826\,\mathscr{E}^2$	70
$\omega_{12} = 3619 - 7917\,\mathscr{E} - 91634\,\mathscr{E}^2$	83
$x_{01} = 0.1912 - 1.7158 \times 10^{-5}\,\omega_{01}$	3.9×10^{-4}
$x_{12} = 0.2665 - 2.3947 \times 10^{-5}\,\omega_{12}$	5.6×10^{-5}
Map Equation for OD	
$\omega_{01} = 2737 - 5732\,\mathscr{E} - 20013\,\mathscr{E}^2$	47
$\omega_{12} = 2675 - 6561\,\mathscr{E} - 60155\,\mathscr{E}^2$	55
$x_{01} = 0.1598 - 1.9219 \times 10^{-5}\,\omega_{01}$	7.0×10^{-4}
$x_{12} = 0.2249 - 2.7283 \times 10^{-5}\,\omega_{12}$	9.6×10^{-5}
Map Equation for OH and OD	
$\mu' = 0.1053 + 16.02\,\mathscr{E}$	0.077

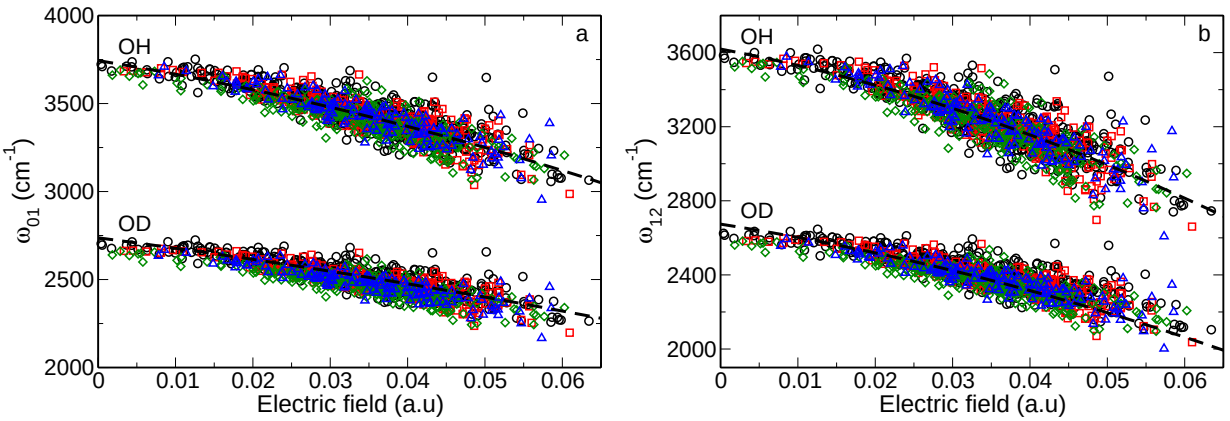

Figure 4.1: The transition frequencies (a) ω_{01} and (b) ω_{12} of the OH and OD stretch of alcohols determined from DFT electronic structure calculations (symbols) are plotted against the electric field at the H (or D) atom projected along the OH (or OD) bond due to the surrounding liquid. Black, red, green,and blue symbols represent methanol, ethanol, propanol, and butanol, respectively. The map equations are also shown (dashed black lines).

to which these equations were fit were the combination of the data for all four alcohols. (The maps derived for each alcohol individually are given in the Appendix.)

The calculated transition frequencies ω_{01} and ω_{12} for all four alcohols, obtained from the DVR calculations on the DFT-derived potential energy curves for clusters extracted from the MD simulations, are shown in Fig. 4.1 for both OH and OD as a function of the electric field, $\mathscr{E}$, on the H (or D) atom of interest projected along the OH (or OD) bond. Note that the OPLS-AA force field used in this work has non-zero charges on the methylene and methyl groups of the alcohol alkyl chains.[135] The data for each alcohol are represented with a different symbol and color and the universal map equations given in Table 4.1 are plotted as dashed lines for comparison. These results indicate that there is not a clear difference between the results for the different alcohols, supporting the use of a single, "universal" map for all the alcohols. As noted in Table 1, the RMSD for the full data set with respect to the universal map is 70 and 83 cm^{-1} for ω_{01} and ω_{12}, respectively. This level of accuracy for the map is quite comparable to those previously developed for water, where corresponding RMSDs of 63-70 and 76-85 cm^{-1} have been reported,[1, 2, 131–133] depending on the water model and simulation parameters. Similarly, the accuracy of the OD maps, RMSDs of 47 cm^{-1} (ω_{01}) and 55 cm^{-1} (ω_{12}), respectively, are comparable with the existing water

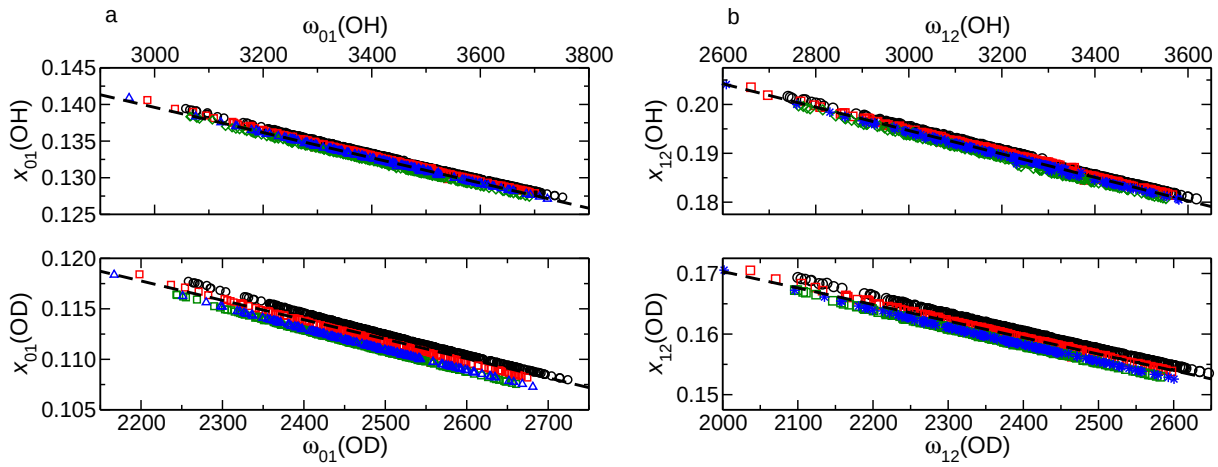

Figure 4.2: The position matrix elements (a) x_{01} and (b) x_{12} of the OH and OD stretch of alcohols determined from DFT electronic structure calculations (symbols) are plotted against the transition frequency of the OH and OD bonds. Symbols and lines are same as for Fig. 4.1.

maps[131–133] with RMSDs of 45-47 and 49-52 cm^{-1} for ω_{01} and ω_{12}, respectively.

The values of the position matrix elements, x_{01} and x_{12}, obtained from the DVR calculations are plotted as a function of the relevant frequency for both OH and OD in Fig. 4.2. Both matrix elements display a linear dependence on the frequency with a slope that is independent of the alcohol considered. There is a small difference in the intercept of the linear behavior for the four alcohols, which is slightly more pronounced for x_{12} than for x_{01}. However, "universal" fits to the entire data set yield map equations that are quite accurate, as is evident from the small RMSDs for the matrix elements (see Table 4.1). Note that the linear behavior of x_{nm} with ω_{nm} reflects that x_{nm} is a measure of the anharmonicity of the bond which varies with the modulation of the frequency due to the H-bonding environment. With respect to the IR intensity, which depend on x_{01}^2, the relatively weak dependence on the frequency leads to only a $\sim 10\%$ difference in intensity across the full-width half-maximum (FWHM) of the frequency distribution.

Finally, the dipole derivative is shown plotted against the electric field $\mathscr{E}$ in Fig. 4.3 and the corresponding empirical map equation is given in Table 4.1. As with the transition frequencies, the dipole derivative data show no clear differences between the four alcohols and the full data set is well fit by a line. The resulting slope (see Table 4.1) is indicative of the significant non-Condon effect, *i.e.*, the large magnitude indicates that the IR intensity is sensitive, through the transition

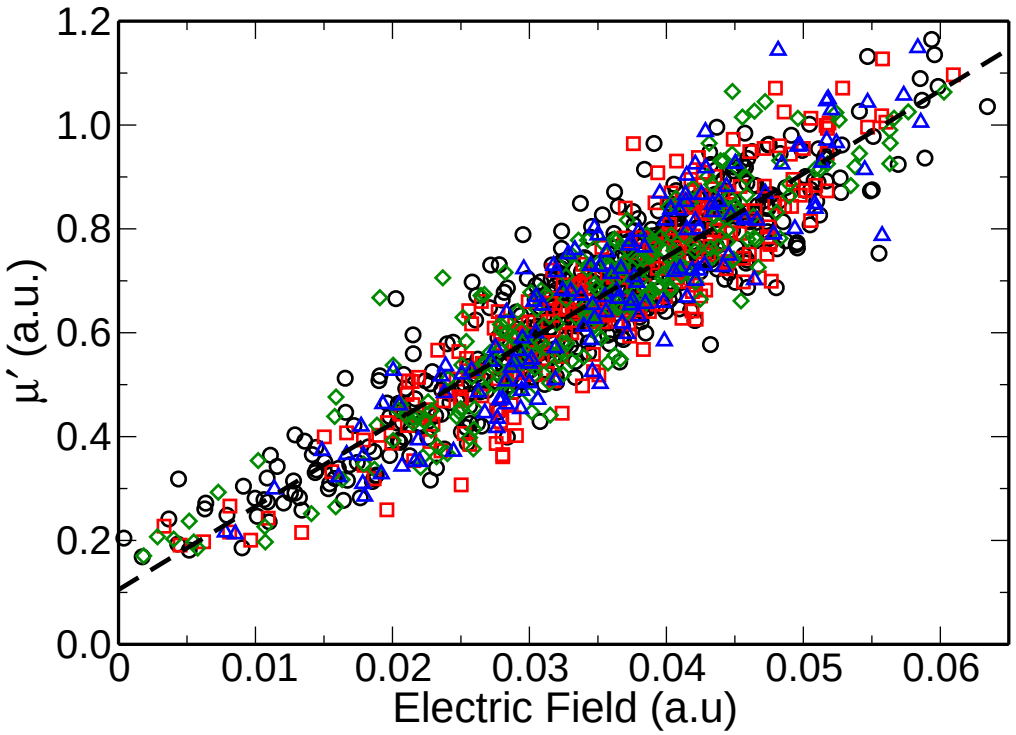

Figure 4.3: The dipole derivative μ' of the OH (OD) stretch of alcohols determined from DFT electronic structure calculations are plotted against the electric field at the H (or D) atom projected along the OH (or OD) bond.

dipole moment, to the H-bonding state of the OH (or OD) bond of interest. Quantitatively, for the IR spectrum which depends on $|\mu'|^2$, this non-Condon effect leads to a change in intensity of a factor of nearly 5.5 across the FWHM of the OH frequency distribution (with the intensity increasing for decreasing frequency).

Previously, Shi *et al.* developed an empirical spectroscopic map for methanol[126] (CH_3OH) and applied it to the calculation of both IR and Raman spectra including resonant vibrational coupling. Their map was derived from a sample of 100 cluster configurations drawn from an MD simulation using similar criteria to those employed here. However, in that work, the potential energy curves used were Morse potentials fit to DFT computations.

4.2.2 Simulated IR Spectra

The infrared spectra of the OH stretch in all four isotopically dilute alcohols were determined using the universal empirical map given in Table 4.1. Specifically, the IR lineshape is given as the Fourier transform,

$$I(\omega) = \frac{1}{2\pi}\int_{-\infty}^{\infty} dt\; e^{-i(\omega-\langle\omega_{01}\rangle)t}\,\phi(t). \tag{4.1}$$

Here, $\phi(t)$ is the response function that involves (with one exception) only quantities that are described within the empirical map equations given in Table 4.1,

$$\phi(t) = e^{-|t|/2T_1}\left\langle \underline{\mu}_{01}(0)\cdot\underline{\mu}_{01}(t)\; e^{i\int_0^t d\tau\,\delta\omega_{01}(\tau)}\right\rangle, \tag{4.2}$$

where $\delta\omega_{01}(t) = \omega_{01}(t) - \langle\omega_{01}\rangle$ is the instantaneous fluctuation in the transition frequency, and $\underline{\mu}_{01}(t) = \underline{e}(t)\,\mu'(t)\,x_{01}(t)$ is the transition dipole moment vector. Here, $\underline{e}(t)$ the unit vector along the OH (or OD) bond, $\underline{\mu}'(\mathscr{E})$ is the dipole derivative calculated using the empirical map, and x_{01} which is the coordinate matrix element between vibrational states $n = 0$ and 1. Also, T_1 is the vibrational lifetime that is taken from experimental measurements; the vibrational lifetimes used were 630 fs for methanol, 720 fs for ethanol, 990 fs for propanol, and 990 fs for butanol.[3] The propanol and butanol values are assumed to be the same as for *iso*-propanol; there are some results indicating that for alcohols the lifetime does not change drastically with increasing length of the alkyl chain.[8]

In Fig. 4.4, the calculated IR spectra of the alcohols are shown. For comparison, the results from the individual maps, *i.e.*, those separately constructed from the data for each alcohol, and from a water map developed for water by the Skinner group[1, 2] are presented as well. The simulated spectra are nearly Lorentzian, suggesting that motional narrowing influences the lineshape (*vide infra*). The universal map gives peak maxima at 3367, 3353, 3356, and 3356 cm^{-1} for methanol, ethanol, propanol, and butanol, respectively, indicating that, after methanol, the peak position is relatively insensitive to the size of the alkyl chain. These results are in reasonable agreement with the available experimental data, displaying only a small blue-shift. Recently, Shinokita

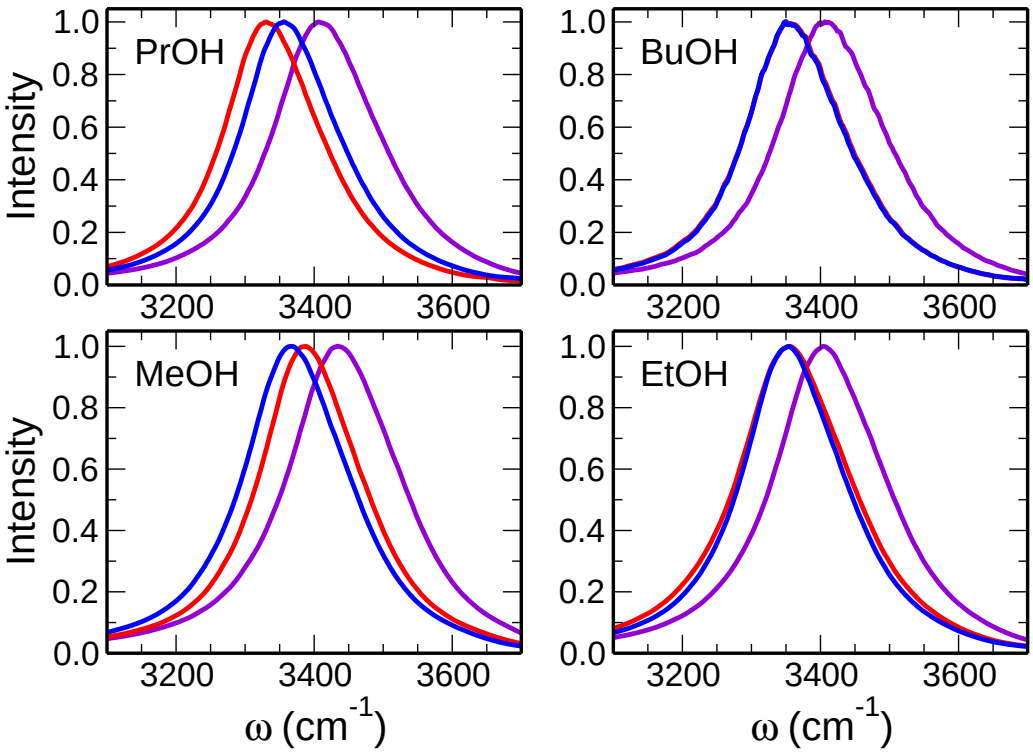

Figure 4.4: Simulated IR spectra of the OH stretch of methanol (MeOH), ethanol (EtOH), propanol (PrOH), and butanol (BuOH). Results obtained using the universal empirical map (blue lines), independent maps developed using data strictly from each alcohol (red lines), and a map developed for water by Auer *et al.*[1, 2] (violet lines).

et al.[3] reported the IR spectra of isotopically diluted methanol and ethanol and found broad maxima at ~ 3350 cm^{-1}. They also found the same peak position for *iso*-propanol, suggesting it is largely independent of the alkyl chain size, at least for lower alcohols. Earlier, Uemura *et al.* examined the effect of isotopic dilution and found that the OH average frequency in the IR spectra of methanol and ethanol increases slightly upon dilution;[111] they obtained average frequencies of ~ 3338 and 3335 cm^{-1} for methanol and ethanol, respectively. Other experiments on neat alcohols (which necessarily include some effect of resonant vibrational coupling not present in the simulations) yield maxima between 3323-3350 cm^{-1} for methanol,[112–115] 3323-3346 cm^{-1} for ethanol,[114, 116] 3319-3320 cm^{-1} for *n*-propanol,[114, 117] and 3309-3332 cm^{-1} for *n*-butanol.[114, 116] The independent maps for each alcohol give spectra in excellent agreement with the universal map for both ethanol and butanol. For methanol, the independent map leads to a

spectrum blue-shifted from the universal map result by ~ 20 cm^{-1}, while for propanol a red-shift of ~ 25 cm^{-1} is found.

In contrast, using the map developed for water leads to a significant blue-shifting of the spectrum in all cases. Relative to the universal map this shift is 68, 52, 53, and 52 cm^{-1} for methanol, ethanol, propanol, and butanol, respectively. This is qualitatively consistent with the simulations of Shinokita *et al.*, which were based on the same water map;[3] they shifted all of their simulated spectra for methanol, ethanol, and *iso*-propanol to the red by 130 cm^{-1} to better agree with measurements.

The linewidths of the simulated spectra, measured by the FWHM, are 179, 173, 167, and 166 cm^{-1} for methanol, ethanol, propanol, and butanol, respectively. These values are smaller than those obtained from the experimental spectra in the case of isotopically dilute methanol and ethanol where linewidths of 236 and 222 cm^{-1}, respectively, were observed.[3] Moreover, Shinokita *et al.* found (by including results for *iso*-propanol) that the peak width narrows with increasing size of alcohol alkyl group, which is consistent with the present results. Interestingly, the linewidths are only moderately sensitive to the map that is used. The individual map spectra given linewidths of 173, 187, 165, and 169 cm^{-1} for methanol, ethanol, propanol, and butanol, respectively, and the water map 191, 187, 180, and 182 cm^{-1}. Thus, the water map gives somewhat broader linewidths than the universal alcohol map, but the same basic trend, while the individual maps are consistent with the universal map in showing a small effect of the alkyl chain length, but do not display not the same ordering among the alcohols. Note that all the spectra for each alcohol are obtained from the same MD simulations. The narrower linewidths, compared to experiments, that are found for all of the maps may arise from an underestimation of the inhomogeneous broadening or overestimation of the dynamics that lead to motional narrowing; both effects are examined below.

4.2.2.1 Contributions from OH Reorientation Dynamics

As is seen from Eq. 4.1, the reorientational dynamics of the OH bond is an important component that can influence the IR spectrum of the OH stretching vibration. We have investigated this

contribution by calculating OH reorientation times in terms of the reorientational autocorrelation function,

$$C_2(t) = \langle P_2[\mathbf{e}_{OH}(0) \cdot \mathbf{e}_{OH}(t)] \rangle. \tag{4.3}$$

Here, P_2 is the second Legendre polynomial and $\mathbf{e}_{OH}(t)$ is the unit vector along the OH bond of interest at time t. The $C_2(t)$ correlation function is of interest because it can be directly measured by IR pump-probe anisotropy experiments[3, 8, 118] and the average reorientation time, defined by

$$\langle \tau \rangle = \int_0^\infty C_2(t)\, dt, \tag{4.4}$$

can be obtained by NMR.[9–13] As we showed previously,[14, 109] the OH reorientation in alcohols can be described by the extended jump model (EJM) which was originally developed for water.[104, 105] The EJM assumes that the OH reorients by two mechanisms: large angular "jumps" associated with exchanges of the H-bond acceptor of the OH group of interest and "frame" reorientation that involves diffusive motion of the intact H-bonded partners between exchanges. In the case of water the jump contribution dominates over the frame reorientation. However, we showed that for methanol and ethanol, the H-bond exchanges are slowed by the steric bulk of the alcohols that prevents the approach of potential new H-bond acceptors. As a result, the frame reorientation becomes the largest contribution to the OH reorientation time. This is not true for all alcohols and depends on the arrangement, as well as the overall quantity, of the steric bulk of the alkyl group.[109] Of particular relevance to the present study is the fact that the jump time is faster than the frame time for *n*-butanol.[109]

The $C_2(t)$ OH reorientational correlation functions for the four alcohols are plotted versus time in Fig. 4.5. It is immediately clear that the OH reorientation is strongly affected by the size of the alkyl group in these linear alcohols that leads to significantly slower dynamics with increasing steric bulk. This is consistent with previous work on water, methanol, and ethanol.[14] Note that the reorientation dynamics occur on multiple time scales. At very short times, ≤ 500 fs, the OH group undergoes inertial (or ballistic) motion associated with its instantaneous angular velocity.

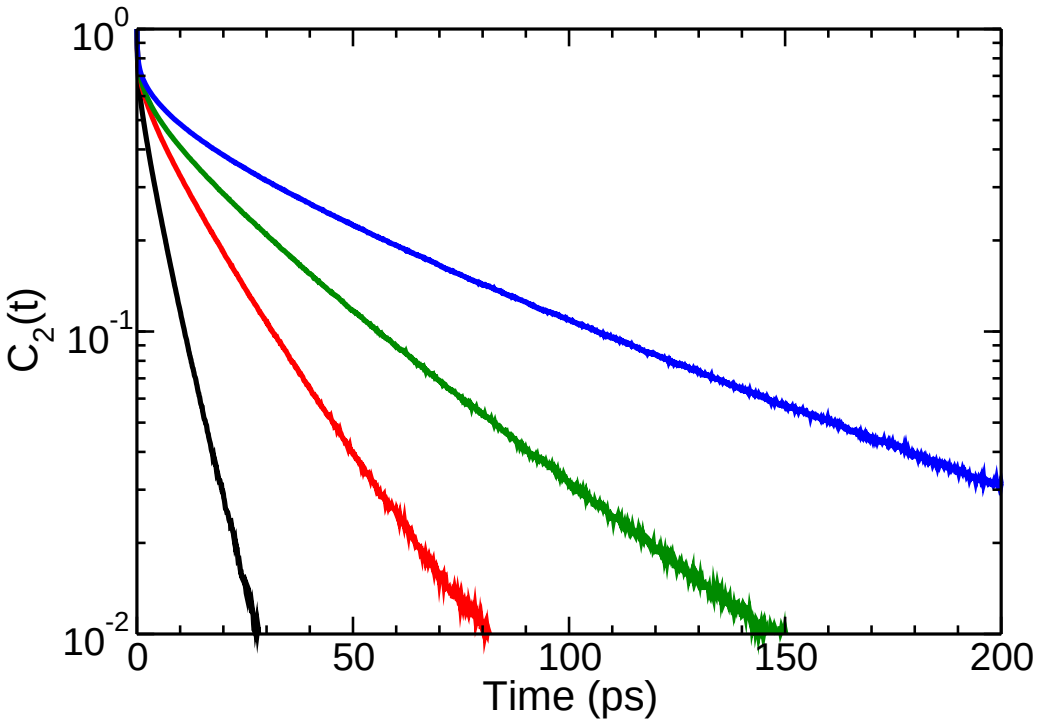

Figure 4.5: Reorientational autocorrrelation function, $C_2(t)$, for OH reorientation in methanol (black), ethanol (red), propanol (green), and butanol (blue) is plotted as a function of time.

Subsequently, the interactions with the H-bond acceptor for the OH group leads to librational motion of the OH within its H-bond. Finally, at longer times complete reorientation of the OH group is affected through frame reorientation and H-bond exchanges, or jumps, as discussed above.

The relatively short (< 1 ps) vibrational lifetime of the OH stretches of the alcohols considered in this work make it challenging to measure the full reorientation dynamics by IR pump-probe anisotropy. Deng *et al.* recently reported the results of anisotropy experiments on isotopically diluted ethanol that yielded a single-exponential reorientation time (following inertial dynamics) of 8.1 ps for the OD bond.[118] This is shorter than the ~ 20 ps longest timescale for ethanol in the $C_2(t)$ dynamics shown in Fig. 4.5, as well as the 12.1 ps we previously obtained with a different molecular model[14, 144] and the 12 ps reported by others.[3] Mazur *et al.* have also reported pump-probe anisotropy measurements of methanol, ethanol, *n*-propanol, and *n*-butanol.[8] They fit their data to a combined heat-diffusion/rotation model that used time constants from dielectric relaxation measurements (scaled by a factor of 1/3.4) for the longest of two timescales. They found

Table 4.2: Average OH reorientation time and the values reported from NMR experiments. (All times are in ps.)

[a] Ref. 9 [b] Ref. 10 [c] Ref. 11 [d] Ref. 12 [e] Ref. 13

Molecule	$\langle\tau\rangle_{MD}$	$\langle\tau\rangle_{NMR}$
Methanol	3.9 ± 0.2	5.1,[a,b] 4.22[c]
Ethanol	11.1 ± 0.5	18,[a,d] 12.1,[e] 9.89[c]
n-Propanol	18.8 ± 0.4	33,[a,d] 19.09[c]
n-butanol	36.3 ± 0.7	51[b]

the shorter timescale increased roughly linearly with the number of CH_2 groups in the alkyl chain from 0.9 ps for methanol to 4 ps for butanol. In our simulations, we find that, following inertial dynamics, there is a timescale of 0.4, 1.3, 1.8, and 3.1 ps in $C_2(t)$ for methanol, ethanol, propanol, and butanol, respectively, that is typically attributed to librational motion. This result is in general agreement with that of Mazur *et al.* However, we do not find the longest times to be consistent with a simple scaling of the dielectric relaxation times that is derived from the ratio of the longest $C_2(t)$ decay time, τ_2, in water to the Debye time, τ_D.[145] This assumption gives them average times of $\langle\tau\rangle$ = 8 ± 1, 18 ± 1, 40 ± 9, and 52 ± 11 ps for methanol, ethanol, propanol, and butanol, respectively. These times are in good agreement with early NMR measurements,[9, 10] but not the present results, more recent NMR data,[11, 13] nor the IR anisotropy measurements of Deng *et al.*[118] While $\tau_D/\tau_2 \simeq 3.4$ has been found experimentally for water,[145] our simulations yield a ratio of $\sim 5-7$ for the alcohols considered here.

It is convenient to also examine the average times given by Eq. 4.4, which average this longest decay time with the inertial and librational components. These have been measured in NMR experiments[9–13] and the results from the present simulations are compared to the measured values in Table 4.2. There is some variation in the measured values that makes a definitive comparison difficult. However, the present results are significantly shorter than the earliest reported measurements,[9, 10, 12] but are in quite good agreement with more recent NMR experiments.[11, 13] We note that the force field used in the MD simulations can affect the observed reorientation times.[144]

Interestingly, the changes in the timescale and mechanism of molecular reorientation in these alcohols, which is associated with both frame reorientation and H-bond exchange dynamics, do not have a significant impact on the IR spectra of these alcohols. Indeed, the timescale for OH reorientation in *n*-butanol is an order-of-magnitude longer than for methanol yet the FWHM of the IR lineshape differs only slightly (by $\sim 8\%$). Moreover, as the alkyl chain is lengthened the reorientational dynamics slow which, in the motionally narrowed regime, would generally be to lead to broader linewidths; instead, the reverse is observed. Thus, these results indicate that reorientational dynamics have at best a minor effect on the IR lineshape.

4.2.2.2 Frequency Distributions and Spectral Densities

In order to further dissect the contributions to the IR spectra, we have calculated the distribution of transition frequencies,

$$P(\omega) = \langle \delta(\omega - \omega_{01}) \rangle, \tag{4.5}$$

and the spectral density,

$$P_\mu(\omega) = \langle |\mu_{01}|^2 \, \delta(\omega - \omega_{01}) \rangle. \tag{4.6}$$

In these expressions, ω_{01} is the fundamental frequency, evaluated *via* the empirical map, that is a function of the classical coordinates of the liquid. The frequency distribution, $P(\omega)$, provides information about the range of environments experienced by OH groups in the alcohol as reported by the vibrational frequency. The spectral density, $P_\mu(\omega)$, provides additional insight through the transition dipole-weighted frequency distribution that accounts (partially) for the intensity in the IR spectrum. The difference between $P_\mu(\omega)$ and the IR spectrum are the dynamical effects, including spectral diffusion, non-Condon dynamics, and reorientational dynamics. Above, we have shown the last of these has a small effect.

The frequency distribution, spectral density, and IR spectrum are compared for each alcohol in Fig. 4.6. We first note that, for each of the four alcohols, the spectral density and IR spectrum are centered around nearly the same maximum frequency. The major difference between the two

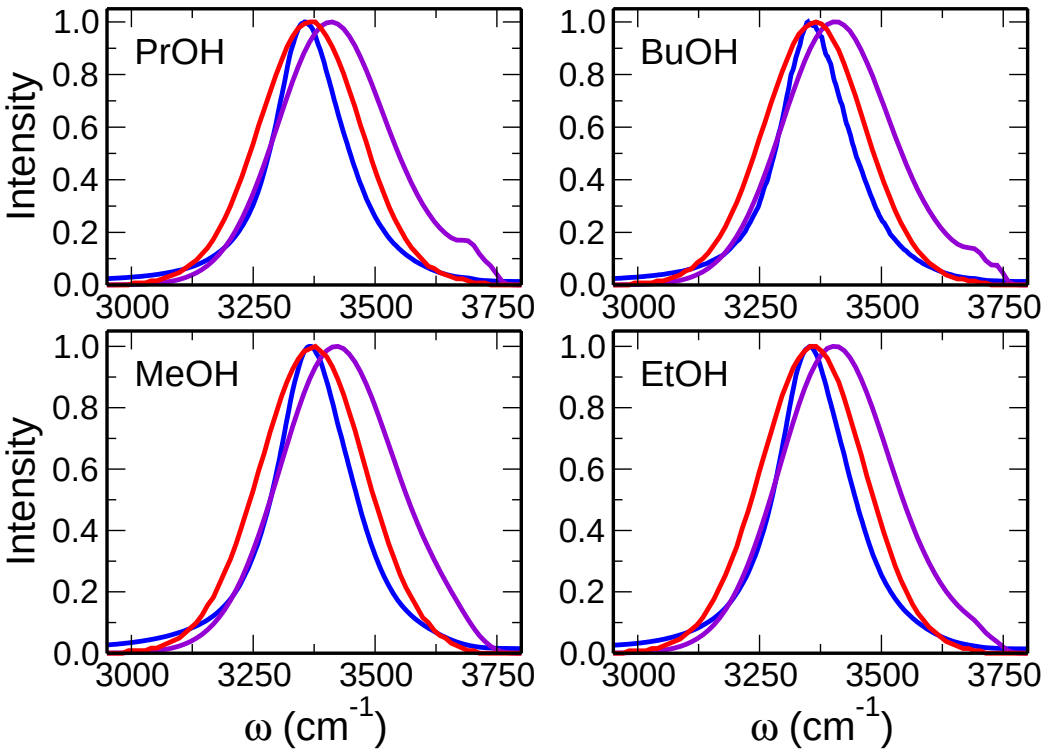

Figure 4.6: The calculated frequency distribution, $P(\omega)$, (violet lines) and spectral density, $P_\mu(\omega)$, (red lines) are compared to the simulated IR spectra (blue lines) for the four alcohols.

is that the spectral density is broader than the IR spectra, indicating how the dynamics of the OH bond leads to a narrowing of the spectra through motional narrowing. As noted above, the OH reorientational dynamics associated with exchanges of H-bond partners are not a key component of these dynamical effects; this indicates that spectral diffusion, which is discussed below, is the primary origin of motional narrowing in the simulations.

The frequency distribution is substantially blue-shifted relative to the IR spectrum by 57, 50, 56, and 50 cm^{-1} for methanol, ethanol, propanol, and butanol, respectively, in contrast to the spectral density, which peaks at frequencies that are only 10, 6, 15, and 10 cm^{-1} higher than the spectrum maximum, respectively. That this blue-shift largely disappears in the spectral density, when the frequencies are weighted by the transition dipole moment, shows that a major contribution to the IR spectra is the non-Condon effect. That is, the peak maximum is primarily determined by the combination of the H-bonding environments experienced by the OH groups and the greater

Table 4.3: Full-width half maximums (FWHMs) for the $0 \rightarrow 1$ frequency distribution, $P(\omega)$, spectral density, $P_\mu(\omega)$, and simulated and experimental[3] IR spectrum, $I(\omega)$ for the four alcohols. (All values are in cm^{-1}.)

Molecule	$P(\omega)$	$P_\mu(\omega)$	$I_{sim}(\omega)$	$I_{expt}(\omega)$
Methanol	283	255	179	236
Ethanol	273	251	173	222
n-Propanol	268	246	167	–
n-Butanol	266	244	166	–

IR intensity of the OH modes that are more strongly H-bonded. This non-Condon effect is evident in the empirical map, which shows that as the OH frequency decreases (with increasing electric field) indicative of stronger H-bonding interactions, the dipole derivative and hence the transition dipole moment increases; this can be seen in Figs. 4.1a and 4.3a and Table 4.1.

A more minor difference between the frequency distributions and spectral densities is observed most clearly for propanol and butanol. For these two alcohols, and to a lesser extent ethanol, a minor peak is observed on the high-frequency site of $P(\omega)$ at ~ 3695 cm^{-1}. These features are not observed in either the spectral densities or the IR spectra, indicating that they correspond to configurations in which the OH group has a small transition dipole moment. That this is the case is expected for higher OH stretching frequencies based on the map equations (Table 4.1). These features are examined in greater detail below.

The simulated IR linewidths are presented in Table 4.3 and compared to the available experimental results[3] as well as the FWHM values for the frequency distributions and spectral densities. As noted above in the discussion of the IR spectra, the simulations give linewidths for methanol and ethanol that are too narrow compared to measurements by $\sim 20-25\%$. The FWHM of the frequency distributions and the spectral densities are larger than that for the measured IR spectra of methanol and ethanol. This makes it unclear whether the smaller simulated IR linewidths are due to underestimating the inhomogeneous broadening, *i.e.*, the width of the frequency distribution, or due to dynamical effects. There are, however, some notable features of these data. First, we note

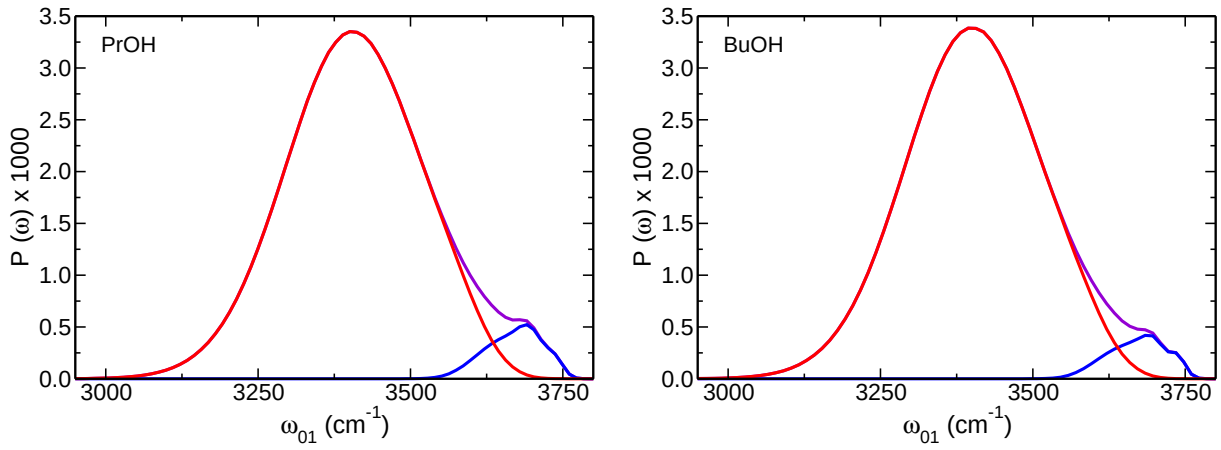

Figure 4.7: The frequency distribution of propanol (PrOH) and butanol (BuOH) for all molecules (violet) and for molecules that are (red) and are not (blue) donating an H-bond.

that for each alcohol the spectral density has a smaller FWHM than the frequency distribution, showing that the non-Condon effect acts to reduce the inhomogeneous broadening represented in the IR spectrum. The magnitude of this effect is nearly uniform as the FWHM of $P_\mu(\omega)$ is 22 cm^{-1} less than that of $P(\omega)$ in all cases but methanol, for which the difference is 28 cm^{-1}. Second, the simulated IR spectra are substantially narrower than the spectral density, by 64-79 cm^{-1}, indicating that dynamical effects significantly influence the spectra. Third, the FWHM of both the frequency distribution, spectral density, and simulated IR spectra monotonically decrease with increasing alkyl chain length. This is consistent with the measured spectra reported for methanol, ethanol, and *iso*-propanol.[3]

It is notable that the change in the inhomogeneous broadening along the series of alcohols is generally reflected in the IR spectral width. That is, the frequency distribution narrows by 10, 5, and 2 cm^{-1} upon addition of a CH_2 group to methanol, ethanol, and propanol, respectively, which is similar to the 4, 5, and 2 cm^{-1} narrowing observed in the spectral density. Similarly, the FWHM of the IR spectrum reduces by 6, 6, and 1 cm^{-1} for the same series upon each addition of a CH_2 group. This suggests that the differences between the IR linewdith for the alcohols in the series is primarily associated with a reduction in the inhomogeneous broadening as measured by the spectral density.

4.2.2.3 Contributions from Dangling OH Bonds

The empirical map for the dipole derivative shows a strong sensitivity to the the solute environment. As a consequence, the IR spectrum does not show features of the high frequency OH stretches observed in the frequency distribution. However, the Raman spectra, which depend on the transition polarizabilities, probe different ensembles of OH groups, which is particularly notable in minor peaks around 3630 cm^{-1} observed in the Raman spectra of larger alcohols.[50, 110, 117, 119, 123] To explore this further, we have decomposed the total frequency distributions into the contributions from OH groups that are and are not donating an H-bond to another molecule. Stringent geometric criteria of $R_{OO} \leq 3.1$ Å, $r_{H\cdots O} \leq 2.0$ Å, and $\theta_{HOO} \leq 20^{\circ}$ were used to define H-bonds.[14] The results are shown in Fig. 4.7 for propanol and butanol. The results show that the shoulder present in the frequency distributions is due to molecules not involved in hydrogen bonds, *i.e.*, dangling OH bonds. These are often referred to as α and β molecules, the former meaning molecules that are engaged in no H-bonds and the latter functioning only as an H-bond acceptor but not a donor.[28] Note that this peak is not observable in the frequency distribution for methanol shown in Fig. 4.6 and is only barely discernable in the ethanol distribution.

It is interesting to examine the structure around these dangling OH bonds. We have done this by calculating the oxygen-oxygen radial distribution functions (RDFs), $g_{OO}(r)$, and associated coordination numbers, $N_{OO}(r)$, separately for molecules with OH stretching frequencies less than and greater than 3630 cm^{-1}. The results are shown in Fig. 4.8 for propanol and butanol. For both alcohols it is immediately apparent that the peak of the first solvation shell of the oxygen-oxygen RDFs of the molecules with OH stretching frequencies greater than 3630 cm^{-1} is substantially reduced, by a factor of $\sim 3-4$, relative to that for molecules with frequencies less than this value. The coordination number, *e.g.*, $N_{\mathrm{OO}}(r) = \int_0^r \rho g_{\mathrm{OO}}(r) 4\pi r^2 dr$, indicates that this is associated with the H-bonding configuration. Namely, for an OH group with a stretching frequency less than 3630 cm^{-1} there is an average of two oxygens in the first solvation shell, but only one oxygen for an OH with $\omega_{01} \geq 3630$ cm^{-1}. This is further support for the identification of these higher OH stretching frequencies as dangling OH bonds.

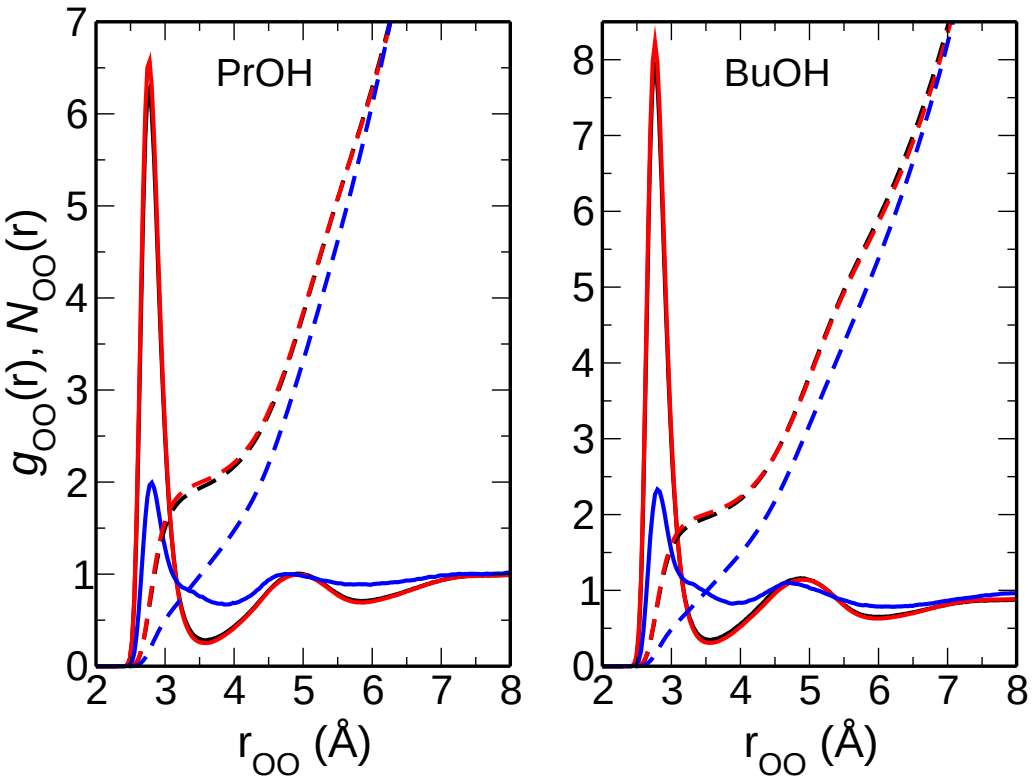

Figure 4.8: Oxygen-oxygen radial distribution functions, $g_{OO}(r)$, (solid lines) and coordination numbers, $N_{OO}(r)$, (dashed lines) for propanol and butanol. Results are shown for all molecules (black lines), molecules with $\omega_{01} \leq 3630$ cm^{-1} (red lines), and molecules with $\omega_{01} \geq 3630$ cm^{-1} (blue lines).

4.2.3 2D-IR Photon Echo Spectra

Third-order nonlinear response functions are used to calculate the 2D-IR photon echo spectra.[146] The 2D-IR photon echo experiment probes the liquid dynamics by examining how the initial vibrational frequency of an oscillator evolves as it interacts in the liquid environment. Briefly, the experiment works by using two laser pulses to label the initial frequency, ω_1, of an OH stretch in the alcohol. Following this, each OH mode evolves with the liquid dynamics for a variable waiting time, T_w, during which the frequency evolves due to the interactions with surrounding molecules. A third laser pulse then is used to instigate the emission of a photon echo from which the new vibrational frequency of the OH stretch can be determined.[147] At very short waiting times the initial and final OH frequency are strongly correlated since the environment of the OH mode in the liquid has not changed much. At very long waiting times, in contrast, there will be no correlation

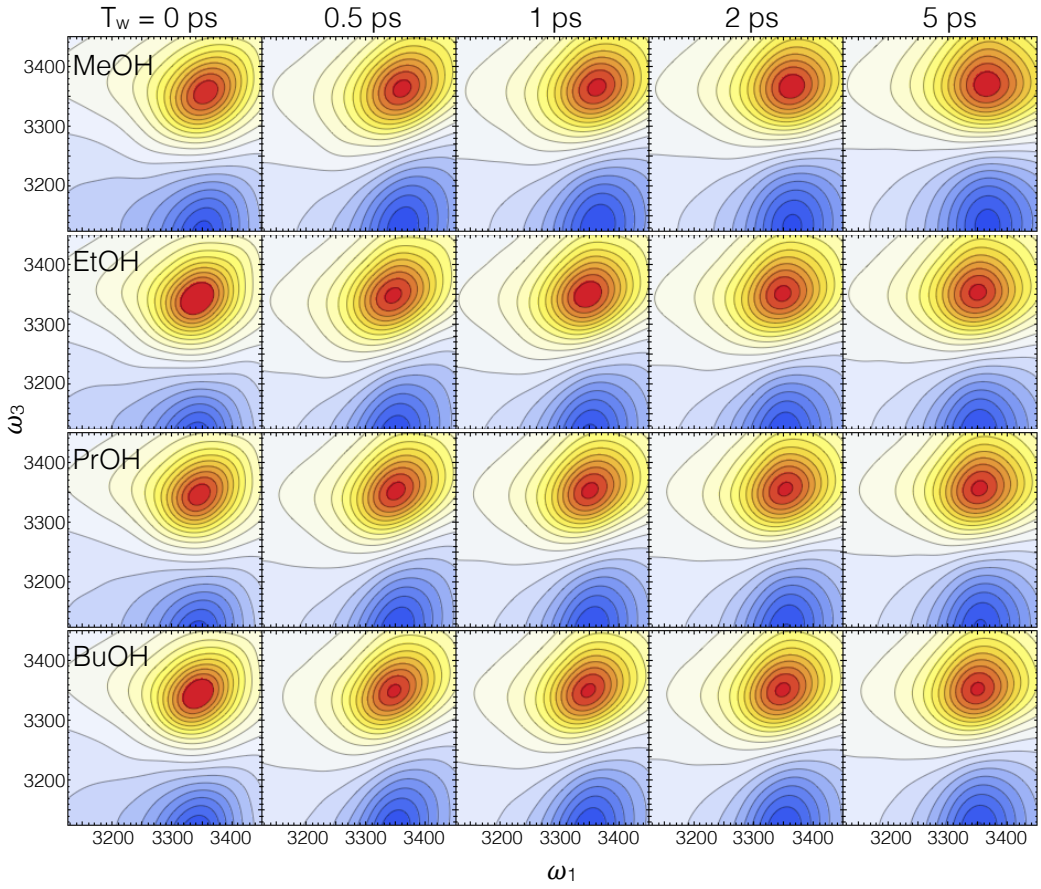

Figure 4.9: The simulated 2D-IR photon echo spectra of methanol (MeOH), ethanol (EtOH), propanol (PrOH), and butanol (BuOH) are plotted for different waiting times. For each waiting time, T_w, 20 contours are shown at even intervals between 110% of the minimum and maximum intensities.

between the initial and final frequency. In this way, the 2D-IR spectrum reports on the dynamics of the OH frequency in the liquid, *i.e.*, its spectral diffusion.

The simulated 2D-IR photon echo spectra are shown in Fig. 4.9 for waiting times from 0 to 5 ps for the four alcohols. In each spectrum there are two peaks apparent, the first is a positive peak (increasing in magnitude from yellow to red) and corresponds to the $0 \rightarrow 1$ transition while the second is a negative peak (colored blue) at lower final frequency, ω_3, that represents the $1 \rightarrow 2$ transition. We will focus on the positive-going peak in our discussion and begin with the generic features that are present for all of the alcohols. With no waiting time, $T_w = 0$ ps, a strong correlation is observed between the initial (ω_1) and final (ω_3) frequencies that is evident from the elliptical

shape of the peak that goes from low to high frequencies. As the waiting time increases, this elliptical peak shape rounds such that at the longer times the peak cross-section is more circular, indicative of an absence of correlation between the initial and final frequencies. The timescale for the evolution of the peak shape reports on the dynamics of the spectral diffusion for the OH modes in the alcohol.

In comparing the 2D-IR spectra for the different alcohols, we see that the spectra are generically the same except for the timescale on which the correlated, elliptical peak shape evolves into a rounded peak indicating a loss of correlation between the initial and final frequencies. Specifically, by $T_w = 5$ ps the peak is almost completely rounded for methanol but there is still some remaining correlation that is clearly observable in the other alcohols. Indeed, the correlation between the initial and final frequencies appears to increase with the alkyl chain length.

4.2.3.1 Spectral Diffusion

A quantitative measure of spectral diffusion is the center-line-slope (CLS),[147] that measures the change in the 2D-IR peak shape that, as noted above, reports on the dynamical changes in the OH frequency. The CLS is defined as the slope of the line connecting the maximum value of the final frequency, ω_3, for each value of the initial frequency, ω_1. In this way, it measures the correlation between the two frequencies. Kwak *et al.*[148] have shown that the CLS, under conditions that are frequently observed, is equal to the frequency-frequency correlation function,

$$C_\omega(t) = \frac{\langle \delta\omega_{01}(0)\, \delta\omega_{01}(t) \rangle}{\langle \delta\omega_{01}^2 \rangle}, \tag{4.7}$$

where $\delta\omega_{01}(t) = \omega_{01}(t) - \langle \delta\omega_{01} \rangle$ is the instantaneous fluctuation in the transition frequency at time t. In simulations the correlation function $C_\omega(t)$ can be directly calculated and the CLS can be obtained as a function of the waiting time from analysis of the 2D-IR spectra.[149] The results for both are shown in Fig. 4.10 and compared to the CLS measured for isotopically diluted methanol and ethanol by Shinokita *et al.*[3]

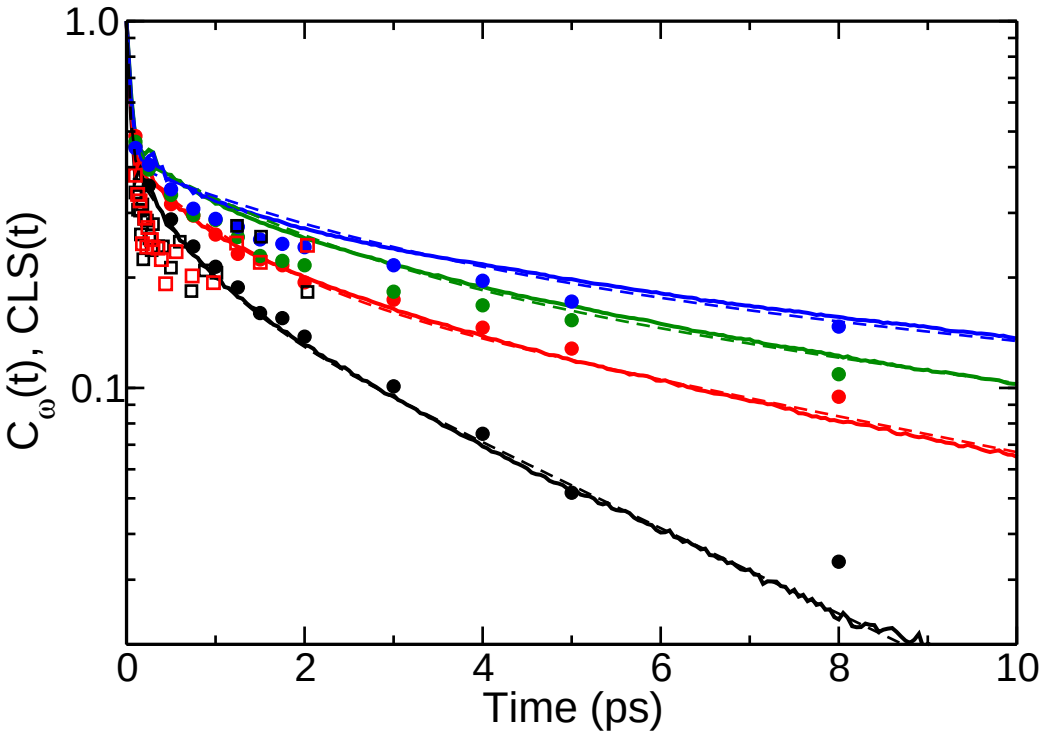

Figure 4.10: The normalized frequency autocorrelation function, $C_\omega(t)$, (solid lines) are compared to the simulated (filled circles) and experimental[3] (open squares) CLS function. Results are shown for methanol (black), ethanol (red), propanol (green), and butanol (blue). Tri-exponential fits to $C_\omega(t)$ are also shown (dashed lines).

The frequency autocorrelation function and the simulated CLS are in generally good agreement, as is expected.[148] The primary difference is that the CLS underestimates $C_\omega(t)$ slightly for propanol and butanol. Both the frequency correlation function and the CLS show that the spectral diffusion slows as the alkyl chain length increases, such that methanol exhibits the fastest dynamics and butanol the slowest. This can be quantified by fitting the $C_\omega(t)$ correlation function to a tri-exponential form; the timescales, from fastest to slowest, can be generally assigned to inertial dynamics, librational motions of the OH within an H-bond, and exchanges of H-bond partners.[129] The fastest inertial timescale is effectively the same, $\sim 35-55$ fs, for all four alcohols, but the other two slow with the size of the alkyl group. The longest timescale is 3.7, 8.9, 14.0, and 21.3 ps for methanol, ethanol, propanol, and butanol, respectively, while the intermediate one is 0.6, 1.1, 1.9, and 2.5 ps for the same series. The trend in the longer timescale is consistent

with the reorientation dynamics discussed above, which is explicitly related to a combination of jumps between H-bond acceptors and rotation of intact H-bonded pairs. However, the reorientation takes place on slower absolute timescales suggesting that the OH frequency changes on timescales faster than H-bond exchanges, *i.e.*, an OH group does not have to change H-bond partners to explore (most of) the range of vibrational frequencies. Note that the timescale for H-bond jumps has previously been calculated to be 14, 30, and 79 ps in methanol, ethanol, and *n*-butanol, respectively.[14, 109]

The spectral diffusion found in the simulations from both the frequency autocorrelation function and the center-line-slope analysis, are not in agreement with the measured CLS reported by Shinokita *et al.*[3] Where the simulations find slower dynamics for longer-chain alcohols, the experiments yield a CLS that is quite similar for methanol and ethanol, as shown in Fig. 4.10; the short vibrational lifetimes make it difficult to measure spectral diffusion dynamics to times longer than ~ 2 ps. They also examined *iso*-propanol and, in concert with simulations that used the water empirical map, concluded that the sub-picosecond dynamics slowed with increasing alkyl group size.[3] This is generally consistent with the present results, though the direct comparison of the full CLS results in Fig. 4.10 is less promising. The origin of the disagreement is not clear at present. Finally, we note that their simulations found the longest timescales in the CLS to be 4 and 7 ps for methanol and ethanol, respectively, in good agreement with the values of 3.7 and 8.9 ps found in the present simulations.

4.3 Summary

A "universal" spectroscopic map based on the linear alcohols from methanol through butanol has been developed. The correlation between the OH vibrational frequency determined by DFT calculations on clusters extracted from MD simulations and the electric field at the H atom directed along the bond does not depend strongly on the identity of the alcohol. The results are promising in suggesting that a single empirical map be adequate to describe the vibrational spectroscopy of a broad range of alcohols.

The simulated IR spectra with the universal spectroscopic map are in generally good agreement with measurements for isotopically diluted methanol and ethanol. The key differences are that they are slightly blue-shifted and somewhat narrower than the experimental spectra. As with water, the non-Condon effects associated with H-bonding have significant consequences for the position and shape of the IR spectrum. This is particularly evident for the longer-chain alcohols propanol and butanol which exhibit dangling OH bonds that are silent in the IR spectrum due to their small transition dipole moment.

In addition to non-Condon effects, dynamics also play an important role in the IR spectra, which are motionally narrowed. However, the IR linewidths do not appear to be particularly sensitive to the significant change in the longest reorientational and spectral diffusion timescales, associated with H-bond breaking and making, which lengthen by factors of ~ 10 and 5 from methanol to butanol, respectively. Over the series of alcohols the inhomogeneous distribution of OH stretching frequencies and the IR linewidth both change by less than 10%. Thus, the relevant dynamical motions are more likely associated with spectral diffusion of OH groups within an intact H-bond.

The spectral diffusion can be directly probed experimentally through the 2D-IR photon echo spectra, which we have also simulated. The spectral diffusion dynamics can be quantified by the center-line-slope, which is often equivalent to the frequency autocorrelation function;[148] we find that this is the case in the present simulations. The simulations show slower spectral diffusion with increasing alkyl chain length. This is expected as the H-bond exchange dynamics is known to slow. However, it is interesting that the spectral diffusion occurs on timescales faster than that for the H-bond jumps and the related OH reorientation. The simulated CLS are not in agreement with reported measurements for methanol and ethanol[3] that show faster dynamics and little difference between the two systems, an issue that requires further investigation. Additional experiments on longer-chain alcohols would be helpful in this context.

The spectroscopic maps presented in this work may be useful in studies on a wider range of alcohols, which is a focus of ongoing work. It remains to be seen if they possess the transferability to inhomogeneous systems that has been observed for water maps,[133, 150] that would signifi-

cantly extend their applicability to the wide range of fundamental and applied contexts in which alcohols are important.

Chapter 5

Vibrational Spectra of the OH Stretching Mode of Isomeric Butanols

In the previous chapters, the importance of alcohols as solvents in the chemical industry and the role played by hydrogen bonds present in the alcohol during chemical separation and reactions was discussed. [20–23]

In our groups on-going efforts to have a molecular level understanding of the mechanism of reorientation in alcohols, I have applied the previously discussed extended jump model (EJM) to study molecular reorientation of isomeric butanols[109], linear alcohols[14] while also probing the structure and dynamics of linear alcohols using vibrational spectroscopy. The work on isomeric butanols showed that the different arrangement of steric bulk led to changes in the reorientation mechanism that are due to a combination of dynamic and entropic factors.[109] A better understanding of the structure and dynamics of the isomers of butanol is now sought through the simulation of IR, Raman, and 2D-IR spectra. Even though the use of vibrational spectroscopy to study the structure and dynamics of butanols is not new,[8, 45–55] there has been no systematic study of isomeric butanols.

The empirical map approach of Skinner and coworkers[1, 2, 130–133] is employed to simulate the spectra of the isomers of butanol. The empirical map used here is our recently developed “universal" empirical map for alcohols that was used to simulate the spectra of the first four linear alcohols from methanol to *n*-butanol. The sections of this chapter are arranged as follows. Details of the simulations used to obtain the spectra are forst discussed. A comparison of the simulated IR spectra of the alcohols is made by discussing the striking features while looking into the origin of

differences present in the spectra of the isomers. Thereafter, the Raman spectra is introduced and compared to the IR spectra of the alcohols. We conclude with a discussion of the 2D-IR spectra of the alcohols, and then examine the rate and mechanism of spectral diffusion in the different isomers.

5.1 Simulation Details

Classical molecular dynamics (MD) simulations were carried out using the LAMMPS software.[74] The optimized potentials for liquid simulations-all atom (OPLS-AA) force field[134, 135] was used to describe the interactions for all four alcohols. The intermolecular potential involves Lennard-Jones interactions for all non-hydrogen atoms along with Coulombic interactions for all atoms. A spherical cuttoff of 12.0 Å was used for all interactions; the long-range electrostatics were included using three-dimensional periodic boundary conditions and an Ewald summation with a tolerance of 1×10^{-4}. The Lennard-Jones and Coulombic interactions between sites on the same molecule were neglected for sites separated by one or two bonds, weighted by half for those separated by 3 bonds, and fully included otherwise. The molecules are fully flexible with an intramolecular potential that is based on harmonic bonds and angles along with the OPLS dihedral potential.[135] For all four isomeric butanols, 40 ns trajectories with an initial 1 ns equilibration period were propagated for each alcohol and configurations were saved every 100 fs. The temperature is maintained by velocity rescaling during the equilibration period and a Nosé-Hoover thermostat[136, 137] with a 100 fs time constant. In order to calculate the infrared spectra the same simulation parameters mentioned above were used but finer time resolution is required. In these simulations the equilibriated trajectories from the 40 ns runs were used as the starting configurations after which a 1 ns trajectory was propagated for each isomer with configurations saved every 2 fs.

5.2 Results and Discussions

5.2.1 Simulated IR Spectra, Frequency Distribution, and Spectral Densities

The infrared spectra of the OH stretch in all four isotopically dilute isomers of butanol were determined using our universal empirical map for alcohols. The IR lineshape is determined by taking the Fourier transform of a response function.

$$I(\omega) = \frac{1}{2\pi}\int_{-\infty}^{\infty} dt\; e^{-i(\omega-\langle\omega_{01}\rangle)t}\,\phi(t). \tag{5.1}$$

Here, $\phi(t)$ is the response function that mainly involves quantities that are described within our empirical map for alcohols

$$\phi(t) = e^{-|t|/2T_1}\left\langle \underline{\mu}_{01}(0)\cdot\underline{\mu}_{01}(t)\; e^{i\int_0^t d\tau\,\delta\omega_{01}(\tau)}\right\rangle, \tag{5.2}$$

where $\delta\omega_{01}(t) = \omega_{01}(t) - \langle\omega_{01}\rangle$ is the instantaneous fluctuation in the transition frequency, and $\underline{\mu}_{01}(t) = \underline{e}(t)\,\mu'(t)\,x_{01}(t)$ is the transition dipole moment vector, with $\underline{e}(t)$ the unit vector along the OH (or OD) bond the only quantity not accounted for in our maps and mainly derived from our 1 ns trajectory files. Also, T_1 (vibrational lifetime) is a phenomenological quantity that is taken from experimental measurements; we used the vibrational lifetime of *iso*-propanol[3] (990 fs) for all four isomers. The vibrational lifetime is assumed to be the same as that for *iso*-propanol because previous work has indicated that changing the size of the alkyl chain does not lead to drastic changes in T_1.[8] It is possible that this assumption does not hold for cases where we have alcohols with the same size of alkyl chain but changing arrangement (different branching) of this alkyl chain which is the case with isomeric butanols. Also, $\delta\omega(\tau)$ is the fluctuation in the transition frequency calculated using the empirical map, $\underline{\mu}(t)$ is the time dependent transition dipole moment for the bond, $\underline{e}(t)$ is the unit vector along the OH (OD) bond, $\underline{\mu}'(\mathscr{E})$ is the dipole derivative calculated using the empirical map, and x_{01} which is the coordinate matrix element between vibrational states $n = 0$ and 1.

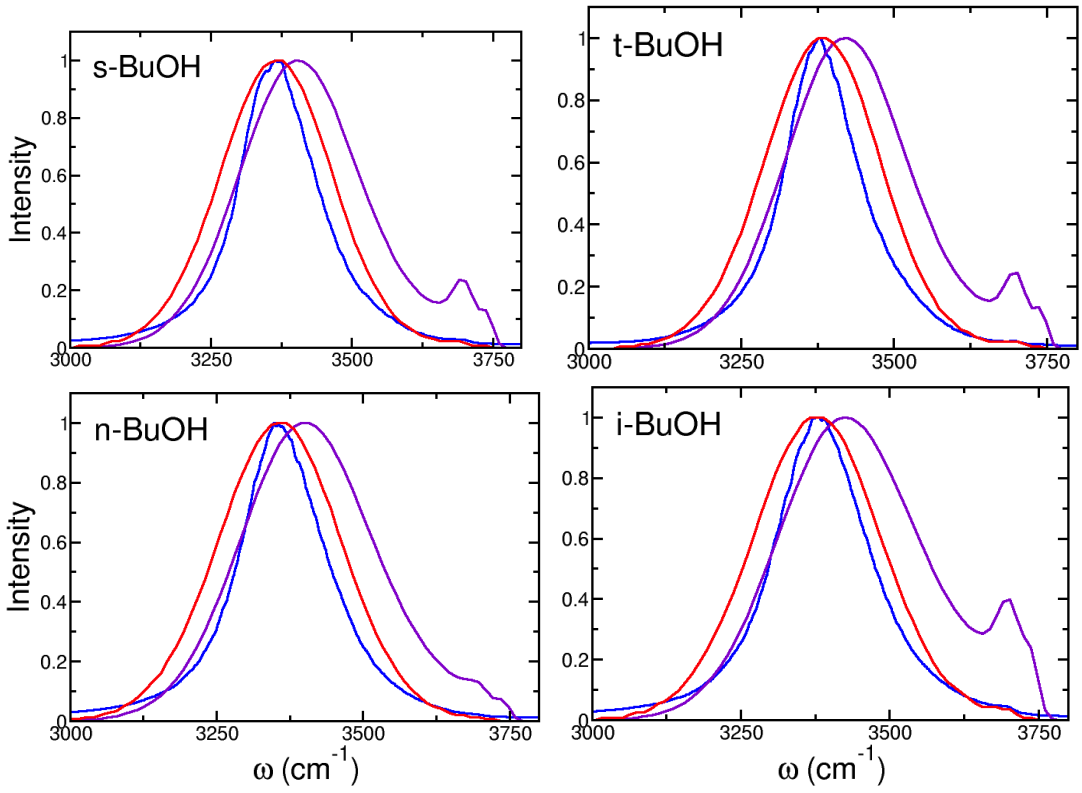

‘

Figure 5.1: The Simulated IR spectra (blue), frequency distribution (red), and spectral densities (violet) of *n*-butanol (n-BuOH), *iso*-butanol (i-BuOH), *sec*-butanol (s-BuOH), and *tert*-butanol (t-BuOH).

In Fig. 5.1, we show the calculated IR spectra of the alcohols as well as the distribution of vibrational frequencies and spectral densities. We start by first compare the IR spectra of all four butanol isomers, before we compare them to the frequency distribution and spectral densities.

The simulated spectra have peak maxima at 3356, 3377, 3363, and 3378 cm^{-1} for *n*-butanol, *iso*-butanol, *sec*-butanol, and *tert*-butanol respectively where the branched alcohols (*iso*-butanol, *sec*-butanol, and *tert*-butanol) are seen to have higher vibrational frequency compared to the linear alcohol (*n*-butanol). As we will soon point out, the fact that *iso*-butanol, *sec*-butanol, and *tert*-butanol have a large proportion of dangling OH bonds might be responsible for higher OH vibrational frequency in these isomers . When compared to experiments, these results are slightly in line where *n*-butanol has peak maxima values between 3309-3332 cm^{-1}[114, 116]. It should be noted that this experiment spectra were for the neat alcohols.

The linewidths of the simulated spectra, measured by the FWHM, are 166, 178, 157, and 141 cm^{-1} for *n*-butanol, *iso*-butanol, *sec*-butanol, and *tert*-butanol respectively. These values show a narrowing of the linewidth with increased branching around the α-carbon in the order *n*-butanol $\rightarrow$ *sec*-butanol $\rightarrow$ *tert*-butanol. *Iso*-butanol which has the fastest reorientation time[109] among the four isomers has the broadest linewidth. In our previous work on linear alcohols, we observed that the simulated spectra for methanol and ethanol have linewidths narrower than what was seen in experiments but there are no experiments on isotopically dilute isomers of butanol to compare these FWHMs. The narrowing of the linewidths with increased branching around the α-carbon is consistent with the narrowing of the linewidths with increasing OH reorientation times in linear alcohols. It is possible that the narrowing of the linewidths that is found for *sec*-butanol, and *tert*-butanol is due to significant non-Condon effect for the secondary and tertiary alcohols or changing dynamics that lead to motional narrowing; in the next sections we will look into both effects.

In an attempt to further probe the contributions to the IR spectra, we have calculated frequency distributions,

$$P(\omega) = \langle \delta(\omega - \omega_{01}) \rangle, \tag{5.3}$$

and the spectral density,

$$P_{\mu}(\omega) = \langle |\mu_{01}|^2 \, \delta(\omega - \omega_{01}) \rangle. \tag{5.4}$$

In the preceding expressions, ω_{01} is the fundamental frequency and it is evaluated using the universal empirical map that we developed for alcohols. The frequency distribution, $P(\omega)$, gives us an idea of the nature of hydrogen bond networks experienced by OH groups of the butanol isomers which is in essence the inhomogeneuos limit. The spectral density, $P_{\mu}(\omega)$, is essentially the transition dipole-weighted (*i.e.,* non-Condon effect) frequency distribution that accounts (partially) for the intensity in the IR spectrum. The difference between $P_{\mu}(\omega)$ and the IR spectrum are the dynamical effects, (*i.e.,*spectral diffusion, non-Condon dynamics, and reorientational dynamics) which are not present in the frequency distribution.

The frequency distribution, spectral density, and IR spectrum are compared for each alcohol in

Table 5.1: Full-width half maximums (FWHMs) for the $0 \rightarrow 1$ frequency distribution, $P(\omega)$, spectral density, $P_\mu(\omega)$, and simulated IR spectrum, $I(\omega)$ for the four alcohols. (All values are in cm^{-1}.)

Molecule	$P(\omega)$	$P_\mu(\omega)$	$I_{sim}(\omega)$
n-butanol	266	244	166
iso-butanol	280	252	178
sec-butanol	250	234	160
tert-butanol	237	223	141

Fig. 5.1. It is imperative to note that for each of the four isomers of butanol, the spectral density and IR spectrum are centered around nearly the same maximum frequency. The major difference being that the spectral density is broader than the IR spectra, which indicates that dynamics of the OH bond leads to a narrowing of the spectra through motional narrowing. Furthermore, the frequency distribution is substantially blue-shifted relative to the IR spectrum by 50, 47, 37, and 50 cm^{-1} for *n*-butanol, *iso*-butanol, *sec*-butanol, and *tert*-butanol respectively, in contrast to the spectral density, which peaks at frequencies that are only 10, -12, 2, and 0.2 cm^{-1} relative to that of the spectrum maximum. The noticeable disappearance of the blue-shift in the spectral density when the frequencies are weighted by the transition dipole moment, especially in the case of *iso*-butanol, shows that a major contributor to the IR spectra is the non-Condon effect. The evidence of this non-Condon effect is in the empirical map, which shows that as the OH frequency decreases (with increasing electric field) (*i.e.,* indicative of stronger H-bonding interactions), the transition dipole derivative increases. The peak maximum is therefore primarily determined by the H-bonding environments.

The simulated IR linewidths are presented in Table 5.1 and compared to the FWHM values for the frequency distributions and spectral densities. For each alcohol the spectral density has a smaller FWHM when compared to the frequency distribution, this further indicates that the non-Condon effect acts in such a way that it reduces the inhomogeneous broadening represented in the frequency distribution. The magnitude of this effect is largest for *iso*-butanol where the FWHM of

$P_\mu(\omega)$ is 28 cm^{-1} less than that of $P(\omega)$, and it decreases in the order *n*-butanol, *sec*-butanol, and *tert*-butanol where the values are 22 cm^{-1}, 16 cm^{-1}, and 14 cm^{-1} respectively. We also note that the simulated IR spectra are substantially narrower than the spectral density, by 74-82 cm^{-1} thus revealing the great influence of dynamical effects on the spectra. The magnitude of the narrowing of linewidths among the different alcohols follows the same order for the frequency distribution, spectral density and IR spectra. This observation indicates that the narrowing of the linewidths in the IR spectra as we move from the primary to secondary and tertiary alcohols follows the inhomogeneous distribution of vibrational OH frequencies.

The FWHM of both the frequency distribution, spectral density, and simulated IR spectra monotonically decrease as we move from primary alcohols (*iso*-butanol and *n*-butanol) to secondary (*sec*-butanol) and tertiary alcohol (*tert*-butanol). While the frequency distribution narrows by 14, 30, and 43 cm^{-1} for *n*-butanol, *sec*-butanol, and *tert*-butanol respectively relative to *iso*-butanol, the spectral density narrowing caused by non-Condon effects are 8, 18, and 29 cm^{-1} for the same series of isomers relative to *iso*-butanol. However, the FWHM of the IR spectrum reduces by 12, 18, and 37 cm^{-1} for the same series. This suggests that the differences between the IR linewdith for the alcohols in the series is due to a combination of the reduction in inhomogeneous broadening due to non-Condon effects as measured by the spectral density and dynamical features like spectral diffusion and OH reorientation dynamics for especially *tert*-butanol and mostly non-Condon effects for *n*-butanol and *sec*-butanol.

Finally, all four alcohols have a peak at the high-frequency side of $P(\omega)$ at $\sim$ 3695 cm^{-1}. This secondary peak is most pronounced in *iso*-butanol and least pronounced in *n*-butanol but the peak is absent in the spectral densities or the IR spectra. This indicates that this high frequency peak corresponds to configurations in which the OH group has a small transition dipole moment which is in line with the dependence of the transition dipole moment on the electric field (See Map Equation in Chapter on Universal Maps of Alcohols). The origin of these features will be discussed in Section 5.2.1.2.

5.2.1.1 Influence of OH Reorientation on IR Spectra

The reorientation dynamics of the OH bond is an important component that influences the IR spectrum of the OH stretching vibration and this is apparent in Eq. 5.1. The contribution of OH reorientation times can be investigated by examining the reorientational autocorrelation function,

$$C_2(t) = \langle P_2[\mathbf{e}_{OH}(0) \cdot \mathbf{e}_{OH}(t)] \rangle. \tag{5.5}$$

Here, P_2 is the second Legendre polynomial and $\mathbf{e}_{OH}(t)$ is the unit vector along the OH bond of interest at time t. The $C_2(t)$ correlation function is of interest because it can be directly measured by IR pump-probe anisotropy experiments[3, 8] and the average reorientation time, defined by

$$\langle \tau \rangle = \int_0^\infty C_2(t)\, dt, \tag{5.6}$$

can be obtained by NMR.[9–13] In our previous study of the reorientation dynamics of these isomers of butanol[109] the OH reorientation in the isomers was described by the extended jump model (EJM) which was originally developed for water.[104, 105] The EJM assumes that the OH reorients by two mechanisms: large angular “jumps" associated with exchanges of the H-bond acceptor of the OH group of interest and “frame" reorientation that involves diffusive motion of the intact H-bonded partners between exchanges.

In that work, we showed that the primary butanols (*n*-butanol and *iso*-butanol) reorients primarily by jumps while the secondary and tertiary butanols (*sec*-butanol and *tert*-butanol) reorients through the diffusive motion of the intact H-bonded partners. Overall, *iso*-butanol reorients the fastest (40 ps) followed by *sec*-butanol and *n*-butanol with similar reorientation times (75 ps), and then *tert*-butanol reorients slowest (104 ps), where all the times reported here are ${\tau_2}^{EJM}$. Similar reorientation times for *n*-butanol and *sec*-butanol is consistent with the analysis in the previous section that the narrowing of their linewidths relative to *iso*-butanol is mainly due to non-Condon effects.

Furthermore, we should note that as previously reported, *tert*-butanol H-bond clusters are primarily made up of ring like structures[68, 71, 83] while *n*-butanol has tends to form linear chains[39, 73] leading to changing reorientation mechanism. As noted in the previous section, this point is important because unlike the case with linear alcohols, the changes in the timescale and mechanism of molecular reorientation in these alcohols, which is associated with both frame reorientation and H-bond exchange dynamics, has a significant impact on the difference in the IR spectra of *tert*-butanol compared to the other alcohols.

5.2.1.2 Unraveling the Origin of Secondary Peaks in The Frequency Distribution and their Disappearance in the IR Spectra

A look at the empirical map for the dipole derivative from the chapter on linear alcohols shows that it has a strong sensitivity to the electric field on the OH bond due to solute environment leading to a IR spectrum that does not show features of the high frequency OH stretches observed in the frequency distribution. However, previous studies[50, 110, 117, 119, 123] have shown that the Raman spectrum shows different ensembles of OH groups, which is particularly notable in minor peaks around 3630 cm^{-1} observed in the Raman spectra of larger alcohols.

Investigating this further, we have decomposed the total frequency distributions into contributions due to OH groups that are and are not donating an H-bond to another molecule. We used tight geometric criteria[14] of $R_{OO} \leq 3.1$ Å, $r_{H\cdots O} \leq 2.0$ Å, and $\theta_{HOO} \leq 20^{\circ}$ to define H-bonds. The results for all four isomers of butanol are shown in Fig. 5.2. The results clearly show that the secondary peak present in the frequency distributions is due to molecules not involved in hydrogen bonds, *i.e.*, dangling OH bonds. The broader distribution of dangling OH bonds in the branched alcohols (most especially *iso*-butanol) compared to *n*-butanol which is a linear alcohol indicates a high proportion of these dangling OH bonds are present in these alcohols.

We decided to investigate the structure around the dangling OH bonds by calculating the oxygen-hydrogen radial distribution functions (RDFs), $g_{OH}(r)$, and associated coordination numbers, $N_{OH}(r)$, separately for molecules with OH stretching frequencies less than and greater than

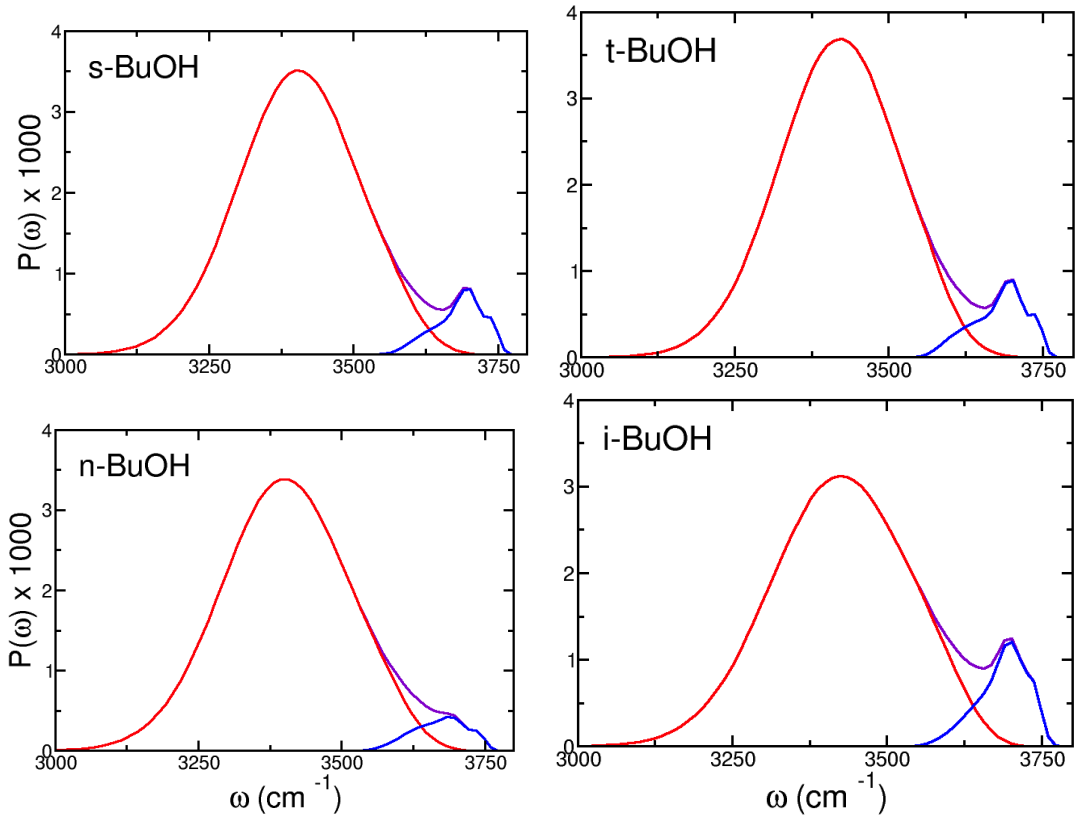

Figure 5.2: The frequency distribution of *n*-butanol (n-BuOH), *iso*-butanol (i-BuOH), *sec*-butanol (s-BuOH), and *tert*-butanol (t-BuOH) for all molecules (violet) and for molecules that are (red) and are not (blue) donating an H-bond.

3630 cm^{-1}. The results for all four isomers of butanol are shown in Fig. 5.3.

For all four isomers of butanol, it is clear that the peak of the first solvation shell of the oxygen-oxygen RDFs of the molecules with OH stretching frequencies greater than 3630 cm^{-1} is substantially reduced, by a factor of $\sim 2-3$, relative to the peak for molecules with frequencies less than this value. The coordination number, *e.g.*, $N_{\mathrm{OH}}(r) = \int_0^r \rho g_{\mathrm{OH}}(r) 4\pi r^2 dr$, indicates that this is associated with the H-bonding configuration. Namely, for an OH group with a stretching frequency less than 3630 cm^{-1} there is an average of one other hydrogen in the first solvation shell, but less than one hydrogen for an OH with $\omega_{01} \geq 3630$ cm^{-1}. This observation further reinforces the identification of these higher OH stretching frequencies as dangling OH bonds.

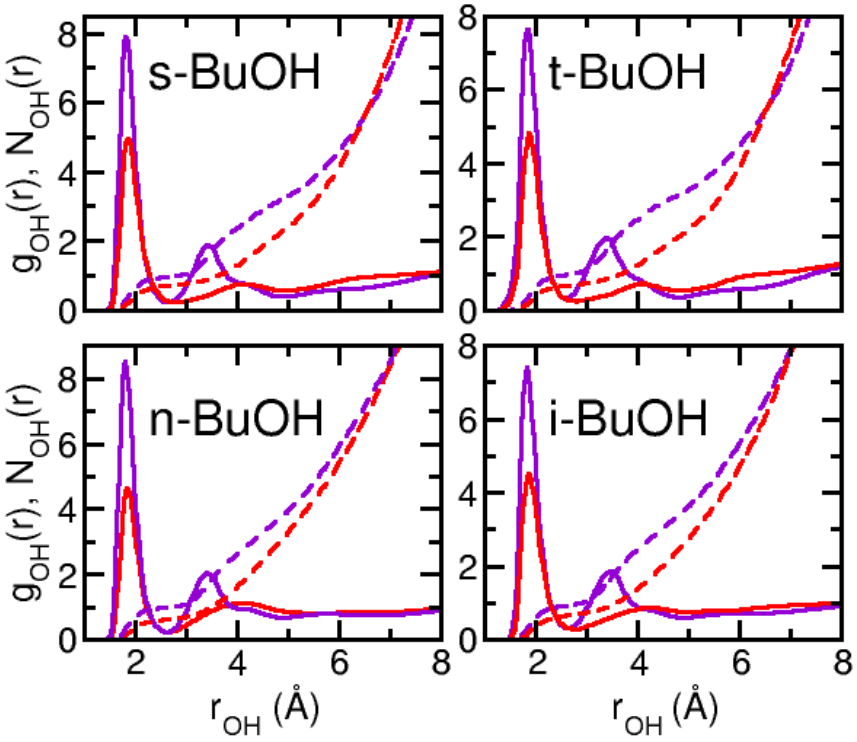

Figure 5.3: Oxygen-hydrogen radial distribution functions, $g_{\mathrm{OH}}(r)$, (solid lines) and coordination numbers, $N_{OH}(r)$, (dashed lines) for all four isomeric butanols. Results are shown for molecules with $\omega_{01} \leq 3630$ cm^{-1} (violet lines), and molecules with $\omega_{01} \geq 3630$ cm^{-1} (red lines).

5.2.2 Raman Spectra of Isomeric Butanols

In the previous section, we mentioned the strong sensitivity of the transition dipole of the OH bond to the electric field due to the surrounding solvent molecules. We also mentioned that the Raman spectrum shows different ensembles of OH groups as was evident in minor peaks around 3630 cm^{-1} in some experiments on linear alcohols.[50, 110, 117, 119, 123] The reason for this is that unlike the transition dipole, the transition polarizability is not as sensitive to surrounding electric field. In order to show this, we have used our empirical map developed based on the transition polarizability in methanol to simulate the Raman spectra of these alcohols. The major difference here is that unlike the IR spectrum the transition dipole derivative in the response function in Eq. 5.1 is replaced by the transition polarizability (α').

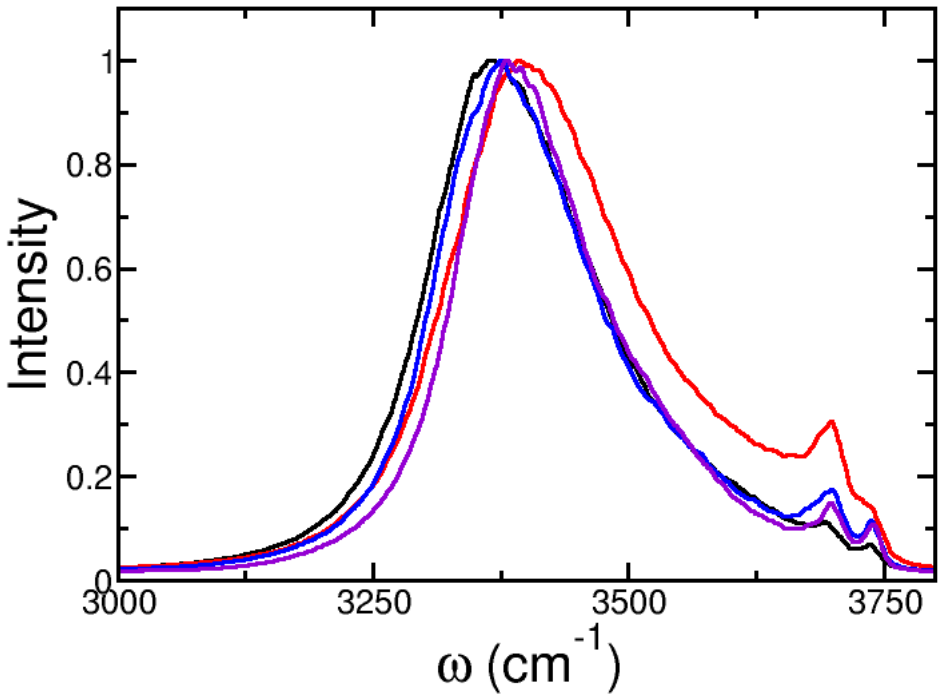

Figure 5.4: The Simulated Raman spectra of *n*-butanol (black), *iso*-butanol (red), *sec*-butanol (blue), and *tert*-butanol (violet).

The simulated Raman spectra is shown in Fig. 5.4 with *n*-butanol, *sec*-butanol, and *tert*-butanol having similar ω_{max} values at 3378, 3376, and 3380 cm^{-1} respectively while *iso*-butanol is again relatively blue-shifted compared to the others at 3392 cm^{-1}. As expected, these values are blue-shifted by 28, 14, 13, and 2 cm^{-1} for *n*-butanol (black), *iso*-butanol , *sec*-butanol, and *tert*-butanol respectively, when compared to ω_{max} values of their IR spectrum. Although less pronounced than the frequency distribution, the Raman spectra shows the presence of a peak at 3700 cm^{-1}.

The linewidths of these isomers are measured by the FWHM. *N*-butanol, *iso*-butanol, *sec*-butanol, and *tert*-butanol have FWHM values of 189, 207, 174, 162 cm^{-1} respectively. The trend in the values of the linewidths is similar to the the observed trend in our simulated IR spectra with the linewidth of the Raman much broader.

5.2.3 Spectral Diffusion Determined Using the Frequency Autocorrelation Function and the Center-Line-Slope

As was discussed in the chapter on linear alcohols, a quantitative measure of spectral diffusion is the center-line-slope (CLS)[147] which reports on the dynamical changes in the OH frequency by following the changing ellipticity of the spectra at different waiting times (T_w) thereby measuring the correlation between initial excitation frequency over time.

As previously noted, Kwak *et al.*[148] have shown that the CLS, under conditions that are frequently observed, is equal to the frequency-frequency correlation function,

$$C_\omega(t) = \frac{\langle \delta\omega_{01}(0)\,\delta\omega_{01}(t)\rangle}{\langle \delta\omega_{01}^2\rangle}, \tag{5.7}$$

where $\delta\omega_{01}(t) = \omega_{01}(t) - \langle\delta\omega_{01}\rangle$ is the instantaneous fluctuation in the transition frequency at time t. From our simulations, we calculate $C_\omega(t)$ and the CLS was also obtained as a function of the waiting time from analysis of the simulated 2D-IR spectra.[149] The results for both are shown in Fig. 5.5.

Looking at Fig. 5.5, there seems to be quantitative agreement between the frequency autocorrelation function and center-line slope for *n*-butanol but not so much for the other isomers of butanol. This might be because the assumed waiting time (990 fs) performs poorly for the other isomers of butanol. We proceeded to quantify the timescale of spectral diffusion by fitting the $C_\omega(t)$ correlation function to a tri-exponential form; the timescales, from fastest to slowest, can be generally assigned to inertial dynamics, librational motions of the OH within an H-bond, and exchanges of H-bond partners.[129]

The fastest inertial timescale is effectively the same, ~60-90 fs, for all four alcohols, but the other timescales show a different trend among the isomers. The longest timescale is 21.7, 22.5, 22.6, and 29.6 ps for *n*-butanol, *iso*-butanol, *sec*-butanol, and *tert*-butanol respectively, while the intermediate timescale is 2.83, 4.23, 1.99, and 3.1 ps for the same series. Unlike the case of linear alcohols previously studied, these timescales are similar. However, like the case of linear

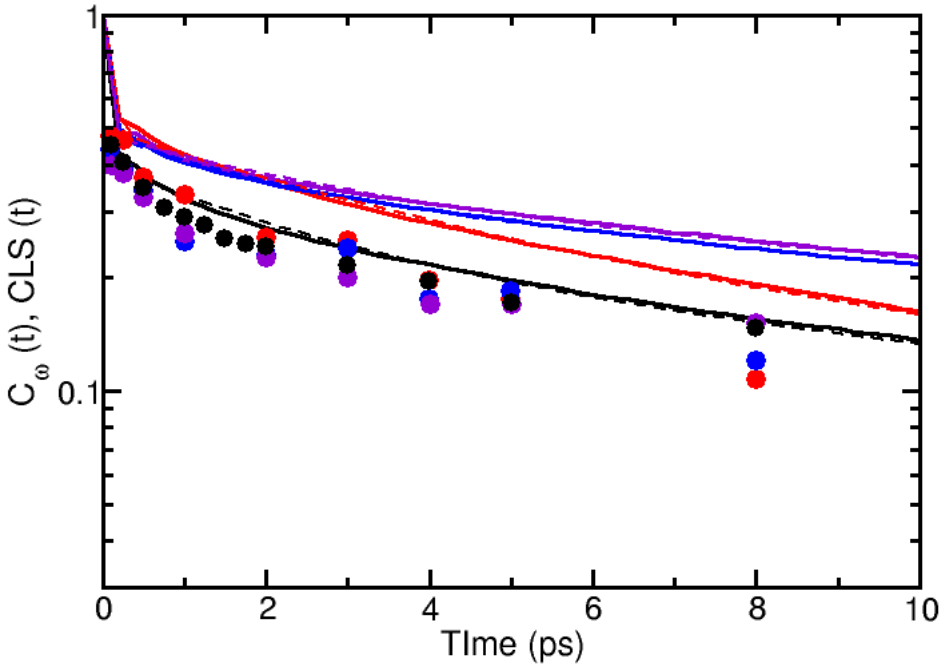

Figure 5.5: The normalized frequency autocorrelation function, $C_\omega(t)$, (solid lines) are compared to the simulated (filled circles) CLS function. Results are shown for *n*-butanol (black), *iso*-butanol (red), *sec*-butanol (blue), and *tert*-butanol (violet). Tri-exponential fits to $C_\omega(t)$ are also shown (dashed lines).

alcohols from the previous chapter, they are smaller in magnitude compared to the timescale of OH reorientation in this alcohols[109] thereby suggesting that the OH frequency changes on timescales faster than H-bond exchanges, *i.e.*, an OH group does not have to change H-bond partners to explore (most of) the range of vibrational frequencies. We should note that the similarity in the timescale of spectral diffusion for all four alcohols suggests that spectral diffusion will play similar roles on the spectra of all the isomers of butanol and that the difference in the spectral linewidth of all four alcohols is primarily due to non-Condon effects and OH reorientation dynamics in the case of *tert*-butanol.

5.3 Summary

In this work, the vibrational spectra of isomeric butanols have been simulated by applying the “universal" spectroscopic map that was developed based on linear alcohols from methanol through butanol. Even though there aren’t any experimental spectra on the isotopic dilute isomeric butanols, the simulated spectra has served as a complementary tool to investigate changing structure and dynamics among these isomers

The simulated IR and Raman spectra showed a narrowing of the linewidth as we moved from the primary alcohols (*iso*-butanol and *n*-butanol) to *sec*-butanol and *tert*-butanol. Non-Condon effects due to H-bonding were seen to play a significant role in the position and shape of both the IR and Raman spectra. The presence of an additional peak $\sim$3700 cm^{-1} in the Raman spectra was discovered to be due to dangling OH bonds that are absent in the IR spectra due to their small transition dipole moment. From the intensity of this additional peak in Raman spectra, we were able to determine that the population of these dangling OH bonds are greatest in *iso*-butanol and least in *n*-butanol.

Spectral diffusion dynamics which was determined by the center-line-slope (*i.e.,* frequency autocorrelation[148]) of the 2D-IR photon echo spectra were seen not to play a major role on the spectra of the series of isomers. This is because we found that the timescale of spectral diffusion was the same for all four alcohols. Based on this result, we believe that the motional narrowing seen in the spectral linewidth is due to the different rates of OH reorientation dynamics in the series of alcohols.

It is hoped that these results will drive experiments in this field to confirm the change in dynamical effects from linear to branched alcohols and thus justify the transferability of our “universal" map for the study of other alcohols either in the bulk or confined systems.

Chapter 6

Intermolecular Vibrational Coupling in Water and Heavy Water: Beyond The Transition Dipole Approximation

Water is commonly known as the "universal" solvent because of its ability to dissolve many substances when compared to other solvents. In water, the intermolecular interaction due to hydrogen bond accounts for the liquid phase structure but many of the properties of the liquid phase are still not fully understood.[151]

Water has a wide range of importance in chemical systems, biological systems as well as the environment and vibrational spectroscopy is a good method of investigating and unraveling the structure and dynamics of water. Infrared and Raman spectroscopy can be used to probe structure[2, 152–155], spectral diffusion in liquids can be probed by spectral hole burning,[156, 157] photon-echo peak shift spectroscopy,[158, 159] and other photon-echo experiments[160, 161], two-dimensional vibrational spectroscopy,[162–164] while rotational diffusion is probed with polarization-resolved pump-probe anisotropy measurements.[152, 165, 166]

In most of these vibrational spectroscopic methods, the ensemble average of the time dependent OH stretch vibrational frequency is a good vibrational mode to follow in order to understand the nature of the structure and dynamics of a hydrogen-bonded liquid like water. The IR spectrum of water in the OH stretch region is known to have a peak at 3400 cm^{-1} and a shoulder at 3250 cm^{-1}. The parallel-polarized (VV) Raman spectrum is bimodal with peaks around the 3250 and 3400 cm^{-1} while the perpendicular-polarized (VH) Raman spectrum has a single peak at 3460 cm^{-1}.[167–169]

A major concern with these experiments is that the vibrational spectroscopy of water can be-

come complicated because of the inter- and intramolecular vibrational coupling in these systems[2] where each individual OH stretch vibrational modes of the molecules in the liquid have (nearly) the same frequency.[170] This complication has led to studies of isotopically dilute water, *e.g.*, HOD in D_2O, where the OH stretch modes is uncoupled from other vibrational modes in the liquid.[152, 162, 163, 166] Unlike water, the parallel-polarized and perpendicular-polarized Raman spectrum of HOD/$D_2$0 in the OH stretch peaks at 3400 cm^{-1} while the IR spectrum was slightly red shifted[152, 153, 155] and the presence of a shoulder at 3625 cm^{-1} in the Raman spectrum was attributed to non-Condon effects.[131] The peak at 3250 cm^{-1} in the parallel-polarized Raman spectrum which also appears as a shoulder in the IR spectrum of water but not in the HOD/D_2O spectrum has been attributed to a number of things including : symmetric, antisymmetric vibrational modes of non-interacting water molecules, different hydrogen-bonding structures,[154, 167, 168, 171] and the excitonic nature of the collective vibrational excitations that lead to the peaks in the spectrum.[169, 172]

Skinner and coworkers have explained the presence of the peak using time domain and frequency domain arguments.[2, 170] In the time domain explanation, they argue that inter-site coupling leads to coherent energy transfer leading to a number of delocalized eigenstates. These eigenstates are seen to extend over a large number of chromophores (OH stretching modes) and the number of chromophores are about 12 near the center of the band. Based on Anderson localization[173] they suggested that a small amount of coupling goes a long way in enhancing delocalization. Because this delocalization could be due to chromophores on the same molecules or on different molecules, they determined that the 12 chromophores are over different molecules hence citing intermolecular vibrational coupling as the major complication to the vibrational spectra of water. The influence of intermolecular vibrational coupling is also known to shape the vibrational spectrum of water in biological system,[174–176] and water/vapor interface, [177–180].

Intermolecular vibrational coupling can be probed using a wide variety of vibrational spectroscopy techniques.[181, 182] and is known to be important in vibrational energy transfer[183–185] which is of utmost importance in chemical and biological processes and in the proper inter-

pretation of vibrational spectra as earlier pointed out. In previous theoretical simulations of the vibrational spectra of water,[2, 154] intermolecular vibrational coupling has been determined using the transition dipole approximation[186, 187] (TDA) and the transition charge coupling. The commonly used transition dipole approximation is known to break down at short distances where the assumption of a dipole-dipole interaction becomes inadequate.[188]

The purpose of this work is to seek a more accurate method to determine intermolecular vibrational coupling. Using an electronic structure derived anharmonic two-dimensional potential energy surface and a sinc-function discrete variable representation[102] we calculate the intermolecular vibrational coupling in water and compare our results to that of TDA. In the subsequent sections, we describe how the two-dimensional potential energy surface neccesary for the calculation of the coupled vibrational energy states is constructed from several snapshots of a molecular dynamics simulation. The combination of a discrete variable representation and a multi-dimensional curve fitting method used to evaluate the vibrational Hamiltonian is also described. In addition to water, in an effort to estimate the influence of isotopic substitution on intermolecular vibrational coupling[183], the intermolecular vibrational coupling in D_2O is detemined. The chapter is concluded by discussing the results and commenting on how the results can be used to build an empirical map where the intermolecular coupling is related to the relative orientation of the coupled OH (OD) bonds involved.

6.1 Simulation Details

6.1.1 Molecular Dynamics Simulations

We carried out a 10 ns NVT classical MD simulation of 343 water molecules using the LAMMPS software[74, 106] with the SPC/E water force field.[107] The integration timestep was 1 fs and configurations were saved every 100 fs. Coulombic and Lennard-Jones interactions were evaluated within a cut-off radius of 10.5 Å. The long-range electrostatic interactions were included using three-dimensional periodic boundary conditions and an Ewald summation with a tolerance of $1 \times$

10^{-4}.

The production stage was preceded by 1 ps and 0.25 ns NVT equilibration periods. The temperature is maintained by velocity rescaling in the former and and a Nosé-Hoover thermostat[136, 137] with a 100 fs time constant in the latter and during the production stage. The molecules are held rigid with the bond length and angle are kept fixed at 1.0 Å and 109.47° respectively using the SHAKE algorithm[189, 190] with an accuracy tolerance of 1×10^{-4} and a maximum number of 20 iterations during each SHAKE solution. Configurations extracted from this trajectory are used to build a two-dimensional potential energy surface (2D PES) that shows the change in the energy of a cluster of water molecules when the OH (OD) bonds on separate water molecules are stretched simultaneously.

6.2 Theoretical Methodology

6.2.1 Two-Dimensional Potential Energy Surface of Coupled Water Vibrations

In order to compute the intermolecular vibrational coupling between two OH (or OD) streching modes in water the anharmonic two-dimensional vibrational Hamiltonian must be evaluated. In this case, the solution of this vibrational Hamiltonian involves a combination of the 2D-PES that describes the simultaneous stretching of both OH bonds and the subsequent use of the sinc-function discrete variable representation (DVR) [102] method to calculate the vibrational eigenstates and their energies.

The 2D-PES is determined for multiple configurations extracted from the equilibrated classical MD trajectory of water described in the previous section. First, we randomly pick a molecule from out of an MD snapshot (see Fig. 6.1) and a cluster of molecules centered around this randomly chosen molecule is then extracted. Following previous work by the Skinner group,[1, 2, 130–133] only molecules whose oxygen atoms atoms are within 7.831 Å of the hydrogen atom of the random molecule are included in the cluster. A total of 988 different configurations were analyzed with the

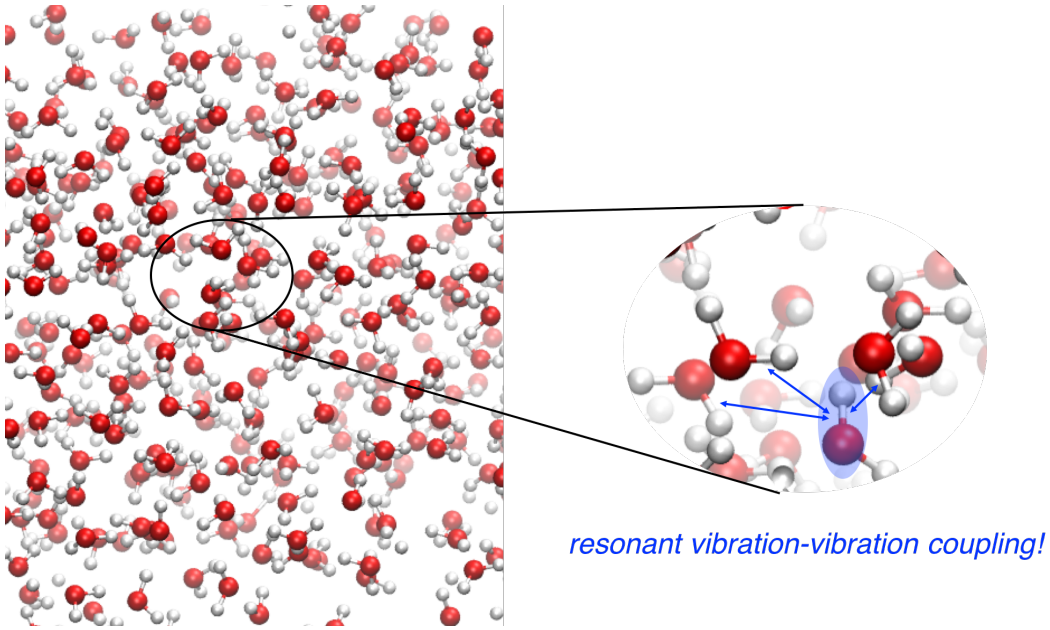

Figure 6.1: A snapshot from a molecular dynamics simulation illustrating intermolecular vibrational coupling.

snapshots being separated by 1 ps in the trajectory. Based on this distance criterion ($r_{O\cdots H}$), the total number of molecules in the cluster ranged between 54 to 63 molecules. The clusters contain an inner sphere of molecules where the atoms are explicitly represented and an outer sphere where the atoms are represented as point charges in subsequent electronic structure calculations. Molecules whose oxygen atoms are within 4 Å of the hydrogen atom of the random molecules are within the inner sphere while all other molecules between 4 Å and 7.831 Å are within the outer sphere. This resulted in the number of molecules in the inner sphere ranging from 5 - 10.

In order to compute the two-dimensional Born-Oppenheimer potential energy surface, the OH bond of the central (random) water molecule (OH_1) and another molecule (partner) (OH_2) in each of the clusters were stretched simultaneously from 0.6572 to 2.0972 Å in intervals of 0.12 Å while the center of mass and orientation of the molecule is kept fixed.[2, 130] This resulted in a total 169 single-point energy DFT calculations for each of the clusters. Individual molecules were treated as pseudodiatomics,[130, 133] with H(D) acting as one half of the diatomic and the OH(D) group being the other half of the diatomic.

The partner molecules in each of the clusters were chosen in such a way that they included

Table 6.1: The number of *Ab-initio* points in a DFT single point energy calculation of simultaneously stretched OH bonds on two water molecules and the resulting energy difference between the first (1) and second ($1'$) excited vibrational states $\Delta\omega_{11'}$ calculated using the sinc-function DVR method. These molecules are part of a cluster extracted from a MD snapshot . (All energies are in cm^{-1})

Ab-initio points	$\Delta\nu_{11'}$
100	25
169	32
225	38
400	33
625	41
1024	41
1369	40
2500	39

molecules that were directly hydrogen-bonded and others that were not bonded to the central (random) water molecule thereby mimicking H-bonding and through-space interactions. These partner molecules were chosen by ranking molecules by their $r_{O\cdots H}$ distance and then based on this ranking, only the closest to 5th closest molecules are chosen as the partner molecule. As shown in Table 6.1, we verified that the number of *ab-initio* points was sufficient by comparing the difference in vibration energy of the first (1) and second ($1'$) excited vibrational state of the coupled chromophores (*i.e.,* the two OH (D) bonds on the central and partner molecules) for calculations in which the OH bonds were stretched in intervals that resulted in 100, 169, 225, 400, 625, 1024, 1369, 2500 *ab initio* points. While the energy gap is not perfectly reproduced with 169 points, the agreement with the densest grid of calculations (2500 points) is adequate to draw conclusions with a significantly reduced computational cost.

The two-dimensional potential energy surface for the OH (OD) stretch of water were determined from DFT calculations using the B3LYP functional[139] and a 6-311++G** basis set.[140] The DFT calculations were carried out using the NWCHEM package.[141] The two-dimensional potential energy surface derived from the DFT calculations was then fit to polynomials using the

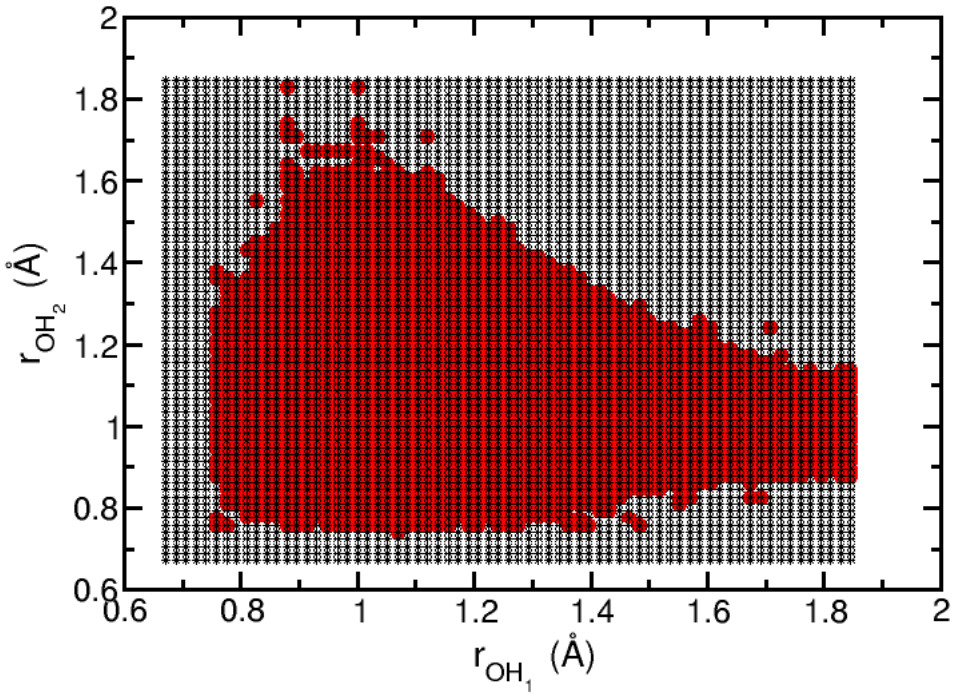

Figure 6.2: An example of a two-dimensional surface with raw grid points (black stars) and truncated grid points (red circles) after using a potential cut-off of $V_{cut} = 3$ eV.

high dimensional model representation (HDMR) of the interpolating moving least square method (IMLS).[191–193] This method is described in the next section. The IMLS fit was used as the potential in the two-dimensional sinc-function DVR calculation to determine the vibrational frequencies and eigenfunctions of the two coupled OH (OD) stretches.

The two-dimensional DVR initially had a total of 100,000 grid points based on a 100×100 grid using ten grid points per deBroglie wavelength. This "raw" grid was then truncated using a potential cut-off in which all grid points for which the potential is higher than $V_{cut} = 3$ eV are deleted. This resulted in truncated grid sizes of between 3500 - 5000 grid points for the OH bonds and 1700 - 3000 grid points for the OD bond.

An example of a two dimensional grid point with raw grid points in black stars and the truncated grid points in red circles is shown in Fig. 6.2.

The full two dimensional DVR Hamiltonian matrix for this problem is,

$$\mathscr{H}_{ij,i'j'} = \hat{\mathscr{T}}_{ii'}\delta_{jj'} + \hat{\mathscr{T}}_{jj'}\delta_{ii'} + V(r_i^a, r_j^b)\delta_{ii'}\delta_{jj'}, \tag{6.1}$$

where i and j are labels for grid points along the coordinates of each of the OH (OD) stretches (a and b). Note that the two-dimensional potential energy matrix is diagonal in the DVR. For radial coordinates like we have in this case where $a = 0$ and $b = \infty$ are the minimum and maximum values of the coordinates and the number of grid points (N) can be infinite in principle, but are made finite by the potential cut-off. The grid spacing Δr is finite and the kinetic energy matrix is given by,

$$\hat{\mathscr{T}}_{ii'} = \frac{\hbar}{2m\Delta r}(-1)^{i-i'} \begin{cases} \frac{\pi^2}{3} - \frac{1}{2i^2}, & \text{if } i = i' \\ \frac{2}{(i-i')} - \frac{2}{(i+i')}, & \text{otherwise} \end{cases}, \tag{6.2}$$

where $\hbar$ is the reduced Planck constant (*i.e.*, $\hbar = h/2\pi$) and m is the mass of the oscillator.

6.2.2 Fitting the 2D PES using the Interpolating Moving Least Squares Method

The two-dimensional Born-Oppenheimer potential energy surface is fit byusing the interpolating moving least squares (IMLS) method,[191–193] an example of which is shown in Fig. 6.3. In the IMLS method, the interpolated potential energy, $V_{fitted}(Q)$, at the nuclear configuration Q can be expressed in terms of a set of linearly independent basis functions $\{b_i(Q)\}$ as

$$V_{fitted}(Q) = \sum_{i=1}^{M} c_i(Q)\, b_i(Q). \tag{6.3}$$

Here, M is the total number of basis functions and $c_i(Q)$ are the coefficients of the basis functions.

The coefficients are determined by minimizing the weighted deviation, $\Delta V_{fitted}(Q)$, of the fitted potential from the known *ab initio* values:

$$\Delta V_{fitted}(Q) = \sum_{i=1}^{N} w_i(Q) \left[\sum_{j=1}^{M} c_j(Q) b_j(Q^i) - V(Q^i) \right]^2, \tag{6.4}$$

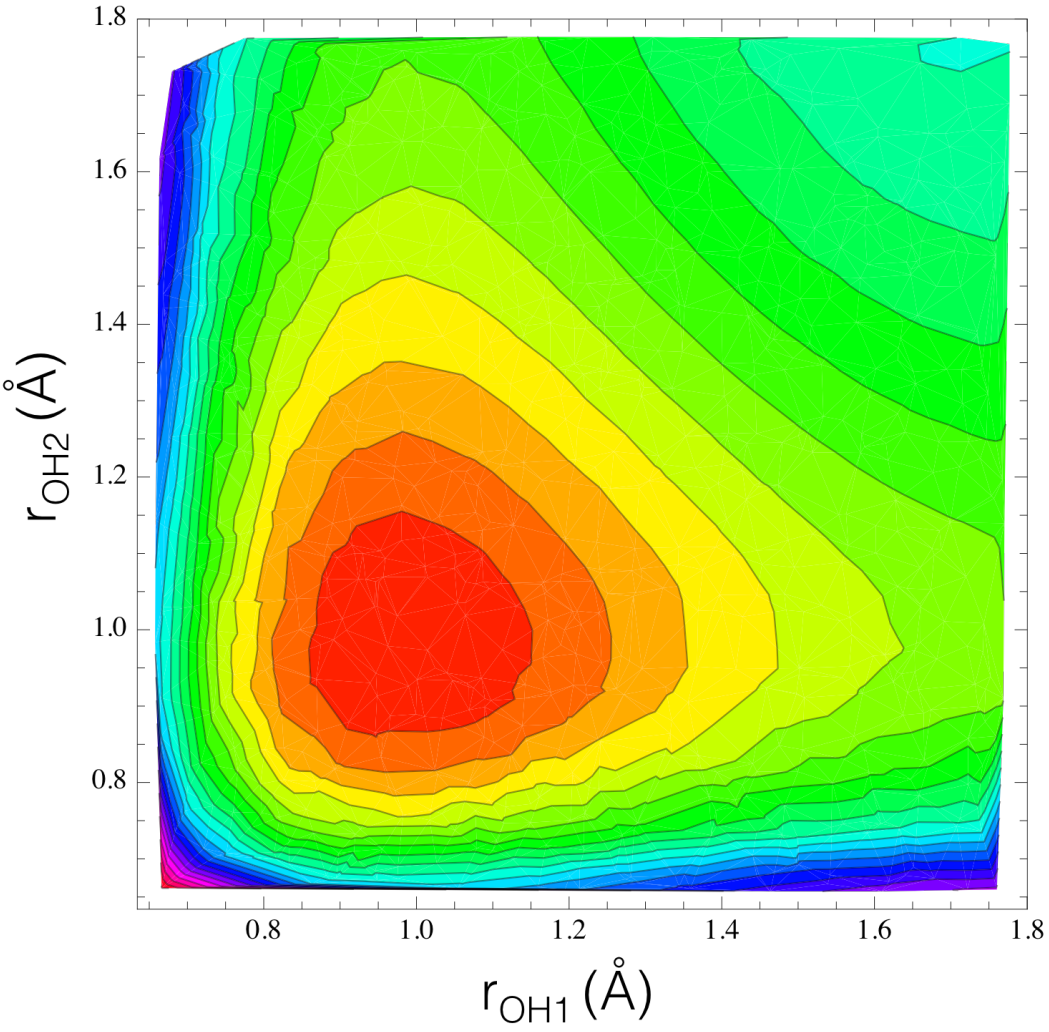

Figure 6.3: The IMLS fit of the Born-Oppenhemier two-dimensional potential energy surface of two OH bonds of different water molecules that are part of a cluster of water molecules.

where, N is the total number of *ab initio* points (169 in this work) and $w_i(Q)$ is a weight function that decays with the distance $\left|Q - Q^{(i)}\right|$ making the weight increase the closer Q is to $Q^{(i)}$. The coefficients $c_i(Q)$ are then determined by minimizing the deviation,

$$\frac{\partial \Delta V_{fitted}(Q)}{\partial c_i} = 0. \tag{6.5}$$

which gives

$$\mathbf{B^T W B c} = \mathbf{B^T W V}, \tag{6.6}$$

where $\mathbf{c} = (c, c_2, \cdots, c_M)^T$, $\mathbf{V} = V(Q^1), V(Q^2), \cdots, V(Q^N)^T$, $\mathbf{W}$ is a N $\times$ N diagonal matrix ($W_{ij} = w_i(Q)\ \delta_{ij}$, and $\mathbf{B}$ is the $N \times M$ matrix of basis functions at the *ab-initio* points ,

$$\begin{bmatrix} b_1(Q^{(1)}) & b_2(Q^{(1)}) & b_3(Q^{(1)}) & \dots & b_M(Q^{(1)}) \\ b_1(Q^{(2)}) & b_2(Q^{(2)}) & b_3(Q^{(2)}) & \dots & b_M(Q^{(2)}) \\ \vdots & \vdots & \vdots & \ddots & \vdots \\ b_1(Q^{(N)}) & b_2(Q^{(N)}) & b_3(Q^{(N)}) & \dots & b_M(Q^{(N)}) \end{bmatrix} \tag{6.7}$$

where N is again the number of *ab initio* points and M the number of basis functions. Finally, solving Eq. 6.6 will give the coefficients $\mathbf{c}$. The flexible density-dependent weight function of Dawes *et al.*[191],

$$w_i(Q) = e^{-((Q-Q_i)/d(i))^2} \Big/ \left[\left(\frac{Q-Q_i}{d(i)} \right)^{2p} + \varepsilon \right] \tag{6.8}$$

was used in this work where $\varepsilon = 10^{-14}$ and $d(i)$ is the distance from Q_i to the $4th$ nearest neighbor.

The cost of IMLS scales as NM^2, so efficient ways of reducing the number of basis functions without losing the quality of the fit is always important.[191] For this reason, the basis is constructed using Higher Dimension Model Representation (HDMR)[194–197] as

$$V^{HDMR}(q_1, q_2, \cdots, q_D) = V_0 + \sum_{i=1}^{D} V_i(q_i) + \sum_{i<j}^{J_D^2} V_{ij}(q_i, q_j) + \cdots \tag{6.9}$$

Here, V_0 is a constant, the first sum is for one coordinate terms where D is the total number of dimensions, and J_D^2 is the binomial coefficient that determines the number of unique two-coordinate terms. The HDMR is a non-redundant model representation and it performs well with a successive reduction in the basis set size where the order of polynomials can be systematically reduced with increasing higher order terms in Eq. 6.9.[191] This successive reduction in the basis leads to a better scaling of the IMLS method.

In fitting of the 2D-PES in this work, a total of 30 basis functions was used. V_0 of the HDMR was taken to be 1 and the single coordinate terms in the HDMR were made up of 6th-order polynomials which gives a total of 12 basis functions. The mixed (two) coordinate terms involving a

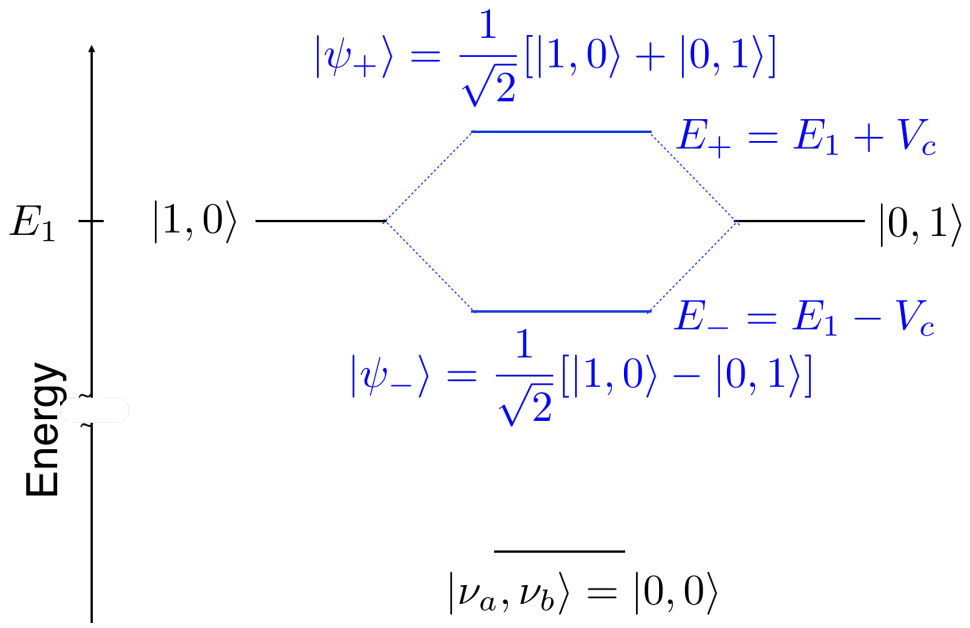

Figure 6.4: Schematic vibrational energy diagram of two resonant OH(D) bonds. The vibrationally excited states ψ_- and ψ_+ are a coherent superposition that results from states $|0,1\rangle$ and $|1,0\rangle$.

product of the OH bond for the central and 'partner' water molecules had a total of 18 basis functions as these mixed polynomials were also restricted to 6th-order. This fit was used as the potential in a sinc-function DVR calculation to determine the vibrational frequencies, eigenfunctions, and position matrix elements for the $0 \rightarrow 1$ and $0 \rightarrow 1'$ transitions for the OH (OD) stretch in water.

6.2.3 A DVR Method to Determine Intermolecular Vibrational Coupling in Water

In Fig. 6.4, we show a schematic picture of the first three vibrational energy levels ($|v_a, v_b\rangle$) of the OH stretch vibrations mode for two water molecules a and b. These three vibrational energy levels belong to the ground state $|0,0\rangle$ and two vibrationally excited states (exciton states) ψ_- and ψ_+ that are a result of the coupling of states $|0,1\rangle$ and $|1,0\rangle$ that involve excitations of single OH modes. (Note that we occasionally refer to the ψ_- and ψ_+ exciton states as the 1 and $1'$ excited states.)

The simple illustration in Fig. 6.4 provides insight into how intermolecular coupling can affect the vibrational spectroscopy of water. When we have a single molecule of water the IR intensity is

simply related to the square of the transition dipole moment matrix element, *i.e.,* $I(\omega) = |\mu_{01}|^2 = |\langle 1|\hat{\mu}|0\rangle|^2$. When two such oscillators are coupled as shown in Fig. 6.4, vibrational excitation from the ground state $|v_a, v_b\rangle$ to each of the excited states ψ_- and ψ_+ leads a loss of signal (dark state, $I_-(\omega) = 0$) for one state and a doubling of intensity for the other state (bright state, $I_+(\omega) = 2|\mu_{01}|^2$) as follows:

$$\mu_- = \frac{1}{\sqrt{2}}\left[\langle 0,1| - \langle 1,0|\right]|\hat{\mu}|0,0\rangle = 0, \tag{6.10}$$

$$\mu_+ = \frac{1}{\sqrt{2}}\left[\langle 0,1| + \langle 1,0|\right]|\hat{\mu}|0,0\rangle = \sqrt{2}\,\mu_{01}, \tag{6.11}$$

which gives $I_-(\omega) = |\mu_-|^2 = 0$ and $I_+(\omega) = |\mu_+|^2 = 2|\mu_{01}|^2$.

When computing the intermolecular coupling between chromophores (OH bonds), it is typically assumed that they interact as point dipoles. The assumption of a point dipole interaction is known as the transition dipole approximation (TDA). As seen in Eq. 6.12, evaluation of the intermolecular coupling constant (β) using the TDA essentially involves parameters related to the relative orientation and magnitude of each transition dipole moment of the interacting chromophores:

$$\beta = k_{ij}x_i x_j k_{ij} = \mu_i' \mu_j' \left\{ \frac{\hat{\mu}_i \cdot \hat{\mu}_j - 3[(\hat{\mu}_i \cdot \hat{n}_{ij})(\hat{\mu}_j \cdot \hat{n}_{ij})]}{{r_{ij}}^3} \right\}, \tag{6.12}$$

where, x_i and x_j are the position matrix elements for the $0 \rightarrow 1$ vibrational transition of dipoles i and j, μ_i' and μ_j' are the transition dipole derivative of the dipoles, $\hat{\mu}_i$ and $\hat{\mu}_i$ are the unit vectors of the dipoles, r_{ij} is the distance between the dipoles, and $\hat{n}_{ij}$ is a unit vector connecting the two dipoles. Following the work by Auer and Skinner,[2] the unit vector ($\hat{n}_{ij}$) is calculated at a position along the bond that is 0.58 Å from the oxygen atom of the OH bond.

In order to calculate the intermolecular vibrational coupling for all 988 different snapshots using the transition dipole approximation, we need to determine the position matrix elements and transition dipole derivative. Using the empirical map developed for water,[2] shown in Table 6.2, we have calculated the transition dipole derivative and the position matrix elements based on the

Table 6.2: Empirical map equations for OH transition frequencies (ω_{01}), coordinate matrix elements (x_{01}), and dipole derivatives (μ') for water. Frequencies are in cm^{-1}, while coordinates, dipole derivatives, and the electric field ($\mathscr{E}$) are in atomic units.

Empirical equations for OH	its RMSD
$\omega_{01} = 3762 - 5060\,\mathscr{E} - 86225\,\mathscr{E}^2$	70
$x_{01} = 0.1931 - 1.75 \times 10^{-5}\,\omega_{01}$	1.1×10^{-4}
$\mu'/\mu'_g = 0.7112 + 75.59\,\mathscr{E}$	0.41

electric field, $\mathscr{E}$, on the H (D) atom of interest projected along the OH (OD) due to the surrounding waters within the outer sphere radius discussed above.

Alternatively, it is also possible to quantify the vibrational coupling constants (β) between two chromophores with the use of our two-dimensional Born-Oppenheimer potential energy surface and the DVR calcualtions. In Eq. 6.13, we show a Hamiltonian matrix indexed by the vibrational states of two chromophores ($|v_a, v_b\rangle$, where v_a and v_b are vibrational states of molecules a and b). In this case $\beta(1)$ is equivalent to the vibrational coupling constant previously calculated using the transition dipole approximation.

$$\begin{array}{c} \langle 0,0| \quad \langle 0,1| \quad \langle 1,0| \quad \langle 0,2| \quad \langle 2,0| \\ \begin{pmatrix} E_{00} & \alpha(1) & \alpha(2) & \alpha(3) & \alpha(4) \\ \alpha(1) & E_{01} & \beta(1) & \alpha(5) & \beta(3) \\ \alpha(2) & \beta(1) & E_{10} & \beta(2) & \alpha(6) \\ \alpha(3) & \alpha(5) & \beta(2) & E_{02} & \beta(4) \\ \alpha(4) & \beta(3) & \alpha(6) & \beta(4) & E_{20} \end{pmatrix} \begin{array}{l} |0,0\rangle \\ |0,1\rangle \\ |1,0\rangle \\ |0,2\rangle \\ |2,0\rangle \end{array} \end{array} \Longrightarrow \begin{pmatrix} E_0 & 0 & 0 & 0 & 0 \\ 0 & E_1 & 0 & 0 & 0 \\ 0 & 0 & E_2 & 0 & 0 \\ 0 & 0 & 0 & E_3 & 0 \\ 0 & 0 & 0 & 0 & E_4 \end{pmatrix} \tag{6.13}$$

As indicated in Eq. 6.13, diagonalization of this matrix gives a matrix whose diagonal elements are the energies of the (excitonic) superposition states that result from the interaction of the states ($|v_a, v_b\rangle$). If these states can be written as a direct product, then the full two-dimensional Hamiltonian, $\hat{\mathscr{H}}$, can be written as a sum of one-dimensional kinetic and potential energies – $\hat{\mathscr{T}}_a$,

$\hat{\mathscr{T}}_b$, $\hat{\mathscr{V}}_a$, $\hat{\mathscr{V}}_b$ – that will each only act on the vibrational states of one oscillator (either a or b) as well as a coupling potential, $\hat{\mathscr{V}}_c$. The coupling potential is related to the difference between the 2D-PES, $\hat{V}(r_a, r_b)$ in Eq. 6.1, and the one-dimensional potential energies, $\hat{\mathscr{V}}_a(r_a) = V(r_a, r_b^{eq})$ and $\hat{\mathscr{V}}_b(r_b) = V(r_a^{eq}, r_b)$, that result from stretching one of the OH bonds and keeping the other at its equilibrium bond length, where r^{eq} = the SPC/E OH bond length = 1.00 Å.

6.3 Results

6.3.1 Intermolecular Coupling from the 2D-PES

We have calculated the energy of the superposition states by solving the full two-dimensional Hamiltonian in Eq. 6.1 and by diagonalizing the matrix elements of the direct product basis in Eq. 6.13. The difference in the energy of the first and second excited superposition states is calculated as $\Delta\omega_{11'} = \langle\psi_+|\hat{\mathscr{H}}|\psi_+\rangle - \langle\psi_-|\hat{\mathscr{H}}|\psi_-\rangle$, for the states ψ_+ and ψ_- obtained by these two methods. For the direct product basis, we have used the full 5×5 matrix shown in Eq. 6.13, a reduced 3×3 matrix containing the first 9 elements of the matrix, and a further reduced 3×3 matrix where $\alpha(1)$ and $\alpha(2)$ are assumed to be zero. The rigorous result is naturally that obtained from the full the 2D Hamiltonian, which can be used to assess the accuracy of the various direct product approaches.

In Fig. 6.5, we plot the distribution of the absolute difference, $|\Delta\omega_{11'}^{2D} - \Delta\omega_{11'}^{DP}|$, which is denoted as "Abs. $\omega_{11'}$ error"; here, "DP" stands for "direct product." This distribution is similar for all three matrices and ranges from 0 to 9 cm^{-1}. More than 70 % of the 988 clusters have an error in the direct product $\omega_{11'}$ of 5 cm^{-1} or less less with the probability of larger errors decreasing. This shows that the direct product approximation does quite well in reproducing the result of the full two-dimensional Hamiltonian.

Based on Fig. 6.5, it is clear that the reduced 3×3 matrix – where $\alpha(1)$ and $\alpha(2)$ are assumed to be zero and $\beta(1)$ (intermolecular vibrational coupling constant) is thus the only off-diagonal element of the matrix – is adequate for reproducing the results of the full 2D Hamiltonian. For all

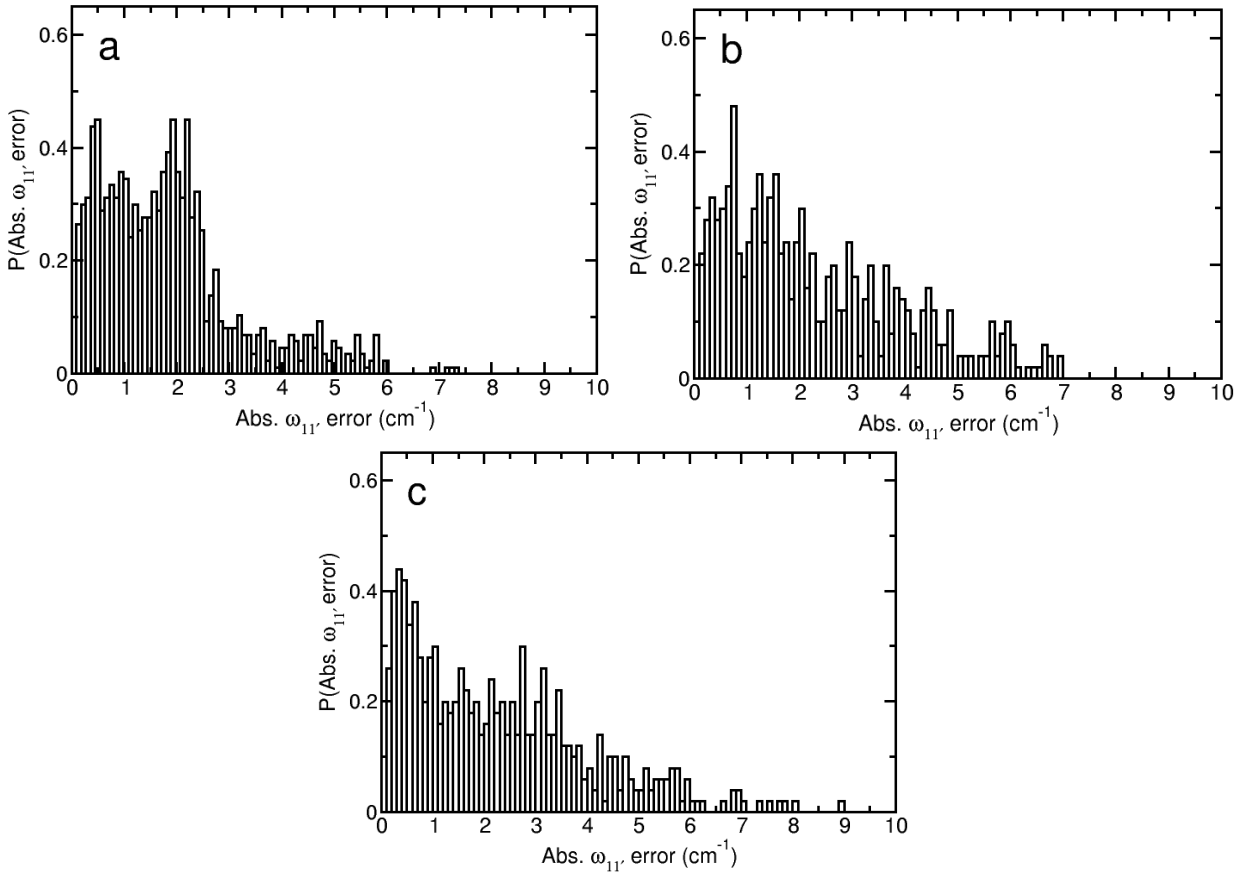

Figure 6.5: The distribution of the absolute difference of $\Delta\omega_{11'}{}^{Full-2D}$ - $\Delta\omega_{11'}{}^{Direct-product}$ is plotted for the (a) Reduced 3 $\times$ 3 direct product basis, (b) 3 $\times$ 3 direct product basis, and (c) 5 $\times$ 5 direct product basis.

subsequent calculations using the direct product basis, this reduced 3 $\times$ 3 matrix is used.

6.3.2 Intermolecular Vibrational Coupling Constants (β) from the TDA and DVR Calculations

The β values of OH oscillators in water are calculated using TDA and DVR methods. The values of β using the DVR method is equivalent to $\beta(1)$ in the direct product matrix. These results are shown in Fig. 6.6. The coupling constant ranges from -50 to 50 cm^{-1} for coupled OH bonds calculated using the DVR direct-product method described above and -60 to 20 cm^{-1} for these same OH bonds when calculated using couplings based on the TDA. The negative and positive values of β result because the two OH bonds considered could be parallel or anti-parallel to one

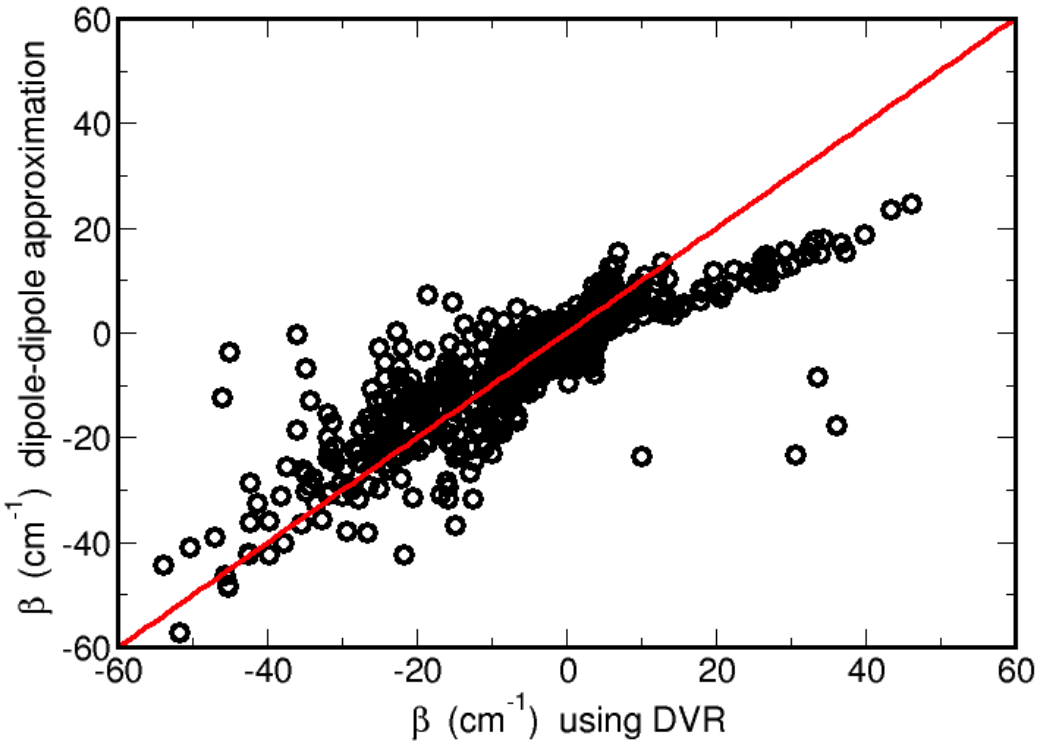

Figure 6.6: The calculated values of β using the DVR and TDA methods. The straight line $\beta_{DVR} = \beta_{DVR}$ is plotted for comparison.

another leading to different signs of the coupling constant. As seen from the plot of $\beta_{TDA} = \beta_{DVR}$, the red line in Fig. 6.6, for small values of β (*i.e.,* oscillators relative far away from each other) the DVR and TDA values are in very good agreement in line with what is expected of the TDA.[188]

At closer inter-oscillator distances where interactions are stronger (absolute value of β is large), there is a clear discrepancy between the DVR and TDA results for β and so the TDA fails as expected. The failure of the TDA to produce quantitative estimates of β at short inter-oscillator distances reinforces the need for a better empirical equation that adequately describes intermolecular vibrational coupling based on the geometry of the molecules involved and their charge distributions.

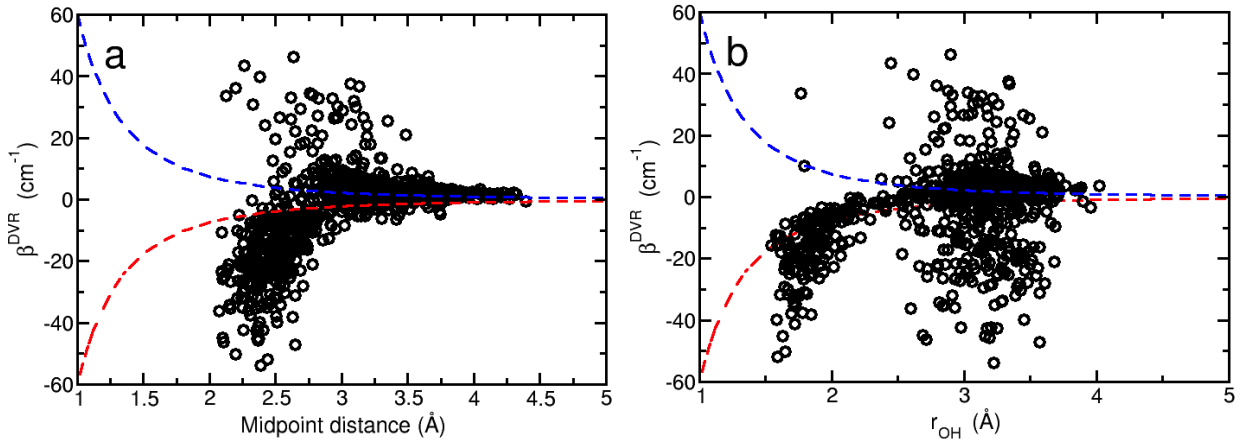

Figure 6.7: The calculated values of β using the DVR is plotted against (a) The distance between midpoints of both OH bonds, and (b) The distance between the oxygen atom of one OH bond and the hydrogen bond of the other. The polynomials $-60/r^3$ (red) and $60/r^3*$(blue) are plotted for comparison.

6.3.3 Intermolecular Vibrational Coupling and the Distance Between the OH Bonds

In the TDA, the coupling constant decays as $1/r^3$ where r is the distance between the midpoint of both oscillators. We have examined the dependence of β obtained with the DVR on this intermolecular distance (r) and the results are shown in Fig. 6.7a. The the polynomials $-60/r^3$ and $60/r^3*$ are also plotted for comparison.

For $r > 3.5$ Å it appears that β does roughly decay as $1/r^3$ as expected within the TDA. However, at much shorter distances, the coupling constant clearly is not described by the TDA model and no $1/r^3$ relationship is observed.

Alternatively, we have used a different distance criteria, $r_{O\cdots H}$, that is the distance between the oxygen atom of one of the OH bonds and the hydrogen atom of the other OH bond. The β values are plotted against $r_{O\cdots H}$ in Fig. 6.7b. In the case of this distance metric, it is clear that there's a poorer $1/r^3$ relationship between the coupling constant (β) and $r_{O\cdots H}$ when the results are compared to results using the other distance criterion. However, at even short distances where the TDA is an inadequate approximation, some of the data points seem to have this $1/r^3$.

6.3.4 Isotope Effect on the Intermolecular Vibrational Coupling in Water

In order to quantify the influence of isotopic substitution on intermolecular vibrational coupling and how this might change the vibrational spectra of D_2O compared to H_2O, we have calculated the difference in energy $\omega_{11'}$ between the first two excited vibrational states (ψ_-, ψ_+) of two coupled OH (or OD) oscillators.

The results are plotted and shown in Figs. 6.8 (a) and (b). While the spacing in the energy levels extend to about 700 cm^{-1} for coupled OH bonds, it extends to just 400 cm^{-1} for the OD bonds. More than 50% of the clusters considered have $\omega_{11'}$ values of between 200 to 800 cm^{-1} for OH, while less than 20% have $\omega_{11'}$ values in this range for OD. These values clearly show that upon isotopic substitution (H $\rightarrow$ D), there is weaker intermolecular coupling. Further validation of this fact is seen in Fig. 6.8 (c) where the intermolecular vibrational coupling constants for OH and OD bonds in water are compared. These values are from the same snapshots of water clusters extracted from MD simulations and the coupling constants for the OD bonds are seen to be smaller when compared to that of coupled OH bonds.

It is predicted that the decrease in coupling upon this isotopic substitution should lead to a smaller shoulder in the vibrational spectra of D_2O. This is the shoulder in the lower frequency range that is due to the presence of excitonic states that may result from intermolecular vibrational coupling in heavy water.

6.4 Summary

In an effort to develop a more accurate empirical relationship between coupled OH stretching modes in water which will, in turn, lead to better simulations of the vibrational spectra of water, a sinc-function discrete variable representation was employed in the calculation of the coupled vibrational states for 988 different configurations drawn from a classical molecular dynamics simulation of water.

The results of the vibrational energies of the direct product DVR basis are compared to that

of the full two-dimensional Hamiltonian and there is a very good agreement between the two. Intermolecular vibrational coupling constants, β^{DVR}, derived from our DVR approach were compared to that derived from the transition dipole approximation, β^{TDA}. This comparison showed the inadequacies of the transition dipole approximation at short intermolecular distances.

Fitting the β^{DVR} values to polynomials of the form $-60/r^3$ and $60/r^3$, where r is an intermolecular distance between the OH bonds showed that it was well fit by this polynomial for intermolecular distances between the midpoints of OH bonds longer that 3.5 Å, in line with the assumptions of the TDA[188]. However, when the intermolecular distance between for OH bonds is measured as the distance between the oxygen atom of one OH bond and the hydrogen atom of the other molecule, the coupling constants are poorly fit to $-60/r^3$ and $-60/r^3$ at long distances.

Finally, intermolecular vibrational coupling was calculated for OD bonds and compared to that of OH bonds. The results indicate that intermolecular vibrational coupling is stronger in water compared to D_2O and as such its vibrational spectra should be less complicated with the collective vibrational band (akin to that of water at 3250 cm^{-1}) red shifted from the main peak less pronounced than that of water.[2, 170]

Based on our DVR results, the next step is to provide an empirical relationship based on point charges and geometric parameters of coupled chromophores that can be used to more accurately evaluate intermolecular vibrational coupling in water with an extensions to H-bonded liquids.

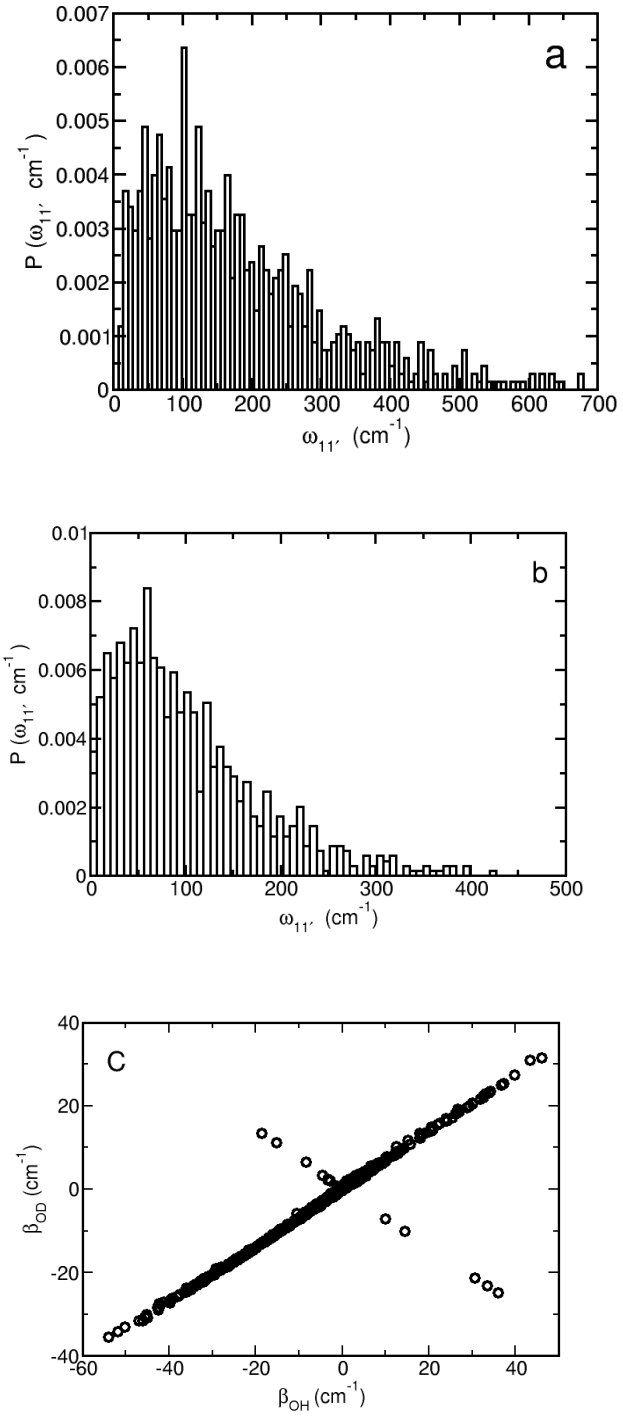

Figure 6.8: The difference between the first (ψ_-) and second (ψ_+) excited states of two coupled (a) OH and (b) OD bonds. (c) is the intermolecular vibrational coupling constant of OH and OD bonds in water.

Chapter 7

Concluding Remarks

7.1 Mechanism of Molecular Reorientation in Isomeric Butanols

The purpose of this work is to investigate the mechanism of molecular reorientation in alcohols. Molecular dynamics simulations of isomeric butanols is used to generate trajectories that are analyzed in this study. By applying the extended jump model, we concluded that the presence of steric bulk around the OH group of an alcohol leads to a slow down in the reorientation of the alcohol. Of the four isomers of butanol studied, *iso*-propanol had the fastest reorientation time followed *n*-butanol and *sec*-butanol with the same reorientation time and *tert*-butanol with the slowest. Similar reorientation times in *n*-butanol and *sec*-butanol is due to a fortuitous cancellation between the jump and frame reorientation times. This work proposes a predictive model that describes molecular reorientation via jumps in alcohols resulting from exchange of hydrogen bond partners coming from adjacent solvent shells.

7.1.1 Future Directions

7.1.1.1 Emergent Jump Reorientation Timescale and Frame Reorientation Times

We know that beyond the predictive model for predicting jump times in alcohols, there's still the need to develop a predictive model to describe frame reorientation. Because the autocorrelation function for calculating frame reorientation is determined from only intact hydrogen bonds, estimates of the frame reorientation time can be poor due to a limited statistics of these intact hydrogen bonds as they do not remain intact over very long timescales. Better estimates of the frame reori-

Table 7.1: Jump times and amplitudes of alcohols determined from the bi-exponential fits to the side-side correlation function; all times are in ps.

Molecule	A_1	t_1	A_2	B_2
Methanol	1	15.9	-	-
Ethanol	0.96	41.4	0.04	8.2
Propanol	0.94	58.9	0.06	16.2
n-butanol	0.86	100	0.14	25.8
Pentanol	0.81	119	0.19	36.3
Hexanol	0.76	157	0.24	44.1
iso-butanol	0.86	56.3	0.14	30.2
sec-butanol	0.92	171	0.08	63.3
tert-butanol	0.85	215	0.15	87.6

entation time can be determined when molecules are tethered together so that the hydrogen bonds are never broken and better estimates of the frame reorientation times can be determined. While viscosity might play a major role in the mechanism of frame reorientation, more work needs to be done to confirm this hypothesis. It is possible to calculate the viscosity of these alcohols using a Green-Kubo relation by calculating the stress autocorrelation function.

In addition, we mentioned that there's a presence of an emergent timescale in the jump reorientation times as we move from water to the alcohols. In an effort to investigate the reason for this emergent timescale, we have done MD simulations of the all-atom model of all linear alcohols from methanol to hexanol and the results of a bi-exponential fit to the side-side correlation function of the jump reorientation are shown in Table 7.1. The jump time contributions from these bi-exponential fits shows that methanol is adequately fit by a single exponential while there is a growing shorter time component with an increase in the alkyl chain length of the alcohols.

The reason for this emergent timescale is not entirely clear, but the presence of the emergent timescale might be due to the absence of correlated jumps where H-bond partners do not switch to different partners at the same time. Some preliminary work has been done to investigate the new

Table 7.2: Comparison of jump time determined from single exponential fits to the coupled correlation function, the product of side-side correlation functions when both reactants are H-bonded (1,2 neighbors), the product of side-side correlation functions when both reactants are separated by a molecule that accepts an H-bond from one of the reactants (1,3 neighbors) and donates H-bond to the other reactant, and side-side correlation function for independent molecules; all times are in ps.

Molecule	$\tau_0(coupled)$	$\tau_0(product^{(1,2)})$	$\tau_0(product^{(1,3)})$	τ_0
Methanol	17	24	26	16
Ethanol	44	61	66	41
Propanol	63	86	96	57
n-butanol	89	121	122	79
Pentanol	118	160	194	105
Hexanol	148	202	252	129
iso-butanol	61	80	91	54
sec-butanol	191	250	279	166
tert-butanol	243	314	348	208

timescale by using coupled correlation functions of the form,

$$\left\langle n_R^A(0) n_R^B(0) n_P^A(t) n_P^B(t) \right\rangle \stackrel{?}{=} \left\langle n_R^A(0) n_P^A(0) \right\rangle \left\langle n_R^B(0) n_P^B(t) \right\rangle, \tag{7.1}$$

where A and B represent H-bond donors when they are reactants (R) and after they switch H-bond partners to products (P). The correlation function is zero when both reactants A and B are with their original H-bond partners at time $t = 0$, and becomes 1 at time t when both have switched H-bond partners. This correlation function is calculated for two different scenarios - if both A and B are direct H-bond partners and also if A and B are not H-bond partners but have one molecule accepting H-bond from A and donating H-bond to B.

The coupled correlation function is fit to a single exponential and the product of side-side correlation functions for the two scenarios discussed above which is the right hand-side of Eq. 7.1 is also fit to a single exponential. The results of the jump time contribution of the coupled correlation function is compared to that of the product of side-side correlation functions and the jump time

contribution from the side-side correlation in Chapter 2. If the equality sign in Eq. 7.1 does not hold, then the jump times from the coupled correlation function must be different from that determined from the product of the side-side correlation functions. For all of the alcohols, the jump time contribution from the coupled correlation function is less than that from the product of correlation functions. The percentage difference in the jump times is similar for all the linear alcohols when jump time contributions from the coupled correlation function is compared to that of the product of correlation function of H-bond partners. The values are 41%, 39%, 37%, 36%. 36%, 36% for linear alcohols from methanol to hexanol. The difference in the jump time contributions from both correlation functions does not support the theory that jumps are uncorrelated because the difference shows that the jumps are indeed correlated and a new theory for the emergent timescale has to be explored.

Another possible reason for the new timescale in the jump contribution could be that when a molecule switches H-bond partners at an initial time (t_1) it could either return to its former acceptor or to an entirely new acceptor. One way to investigate this is to write a correlation function of the form,

$$\left\langle n_R^A(0) n_P^B(t_1) n_P^C(t_2) \right\rangle, \tag{7.2}$$

$$\left\langle n_R^A(0) n_P^B(t_1) n_P^A(t_2) \right\rangle, \tag{7.3}$$

where the reactant is H-bonded to A at time $t = 0$ and H-bonded to B at time t_1. The reactant either goes back to A at t_2 or switches to an entirely different partner which is C. An investigation of this correlation function might yield some insights into the origin of the new jump contribution times.

Finally, since the nature and magnitude of the emergent timescale changes with the length and arrangement of the alkyl chain of the alcohols, a theory that links the emergent timescale to the length and arrangement of the alkyl chain will prove very useful.

7.1.1.2 Molecular Reorientation of Nanoconfined Alcohols, polyols and Alcohol-Water Mixtures

An extension of this work will be to investigate alcohol-water mixtures mainly because of their use as co-solvents in chemical processes and small polyols that are either geminal or vicinal. The effect of nanoscale confinement on molecular reorientation of alcohols should also be pursued. We know that upon the nanoscale confinement of water in silica, there is an emergence of an additional timescale due partly to molecules of water H-bonded to the silica. Such additional timescale should be expected in the case of alcohol themselves and should depend on the propensity of the alcohols to form H-bonds to other molecules, *i.e.,* either to other water molecules in a mixed solvent or to H-bonding groups on the walls of the nanoscale silica pores.

7.2 Removing the Barrier to the Calculation of Activation Energies

In the second chapter, activation energies were calculated from quantum and molecular dynamics simulations by using time correlation functions that can yield reaction rate constants. In this way, we were able to determine the activation energy for particles crossing the model one-dimensional Eckart potential and for H-bond jumps in liquid water.

The calculation of the activation energy of jump reorientation in water uses the constant number of particles, volume, and temperature (NVT) ensemble and the results are sensitive to the frequency at which the thermostating of the simulation temperature is done. Recent work has shown that the better way of determining activation energies would be to extract multiple snapshots from an equilibriated NVT trajectory and performing short constant number of particles, volume and energy (NVE) simulations on these snapshots. These simulations last for short, several picosecond times and are performed on a couple thousand of extracted snapshots.

7.2.1 Future Directions

7.2.1.1 Activation Volumes from a Single Temperature Simulation

The activation volume tells us if the transition state of a chemical reaction is associative or dissociative and can be determined in a way similar to the activation energy. Dang and coworkers have determined the activation volume of solvent exchange in water, methanol, and ion pairs in water, methanol, and acetonitrile.[198–201] The activation volume in all of this work was determined by performing several NPT simulations at different elevated pressures typically thousands of bars.

$$\Delta V^{\ddagger} = -RT\left(\frac{\partial ln(k)}{\partial P}\right)_T. \tag{7.4}$$

As seen in Eq. 7.4, the slope of a plot of the natural logarithm of the activation energy against pressure for all of the simulated pressures gives the activation volume. Here, V is the volume, k is the rate constant, and T outside the parenthesis means the pressure dependence of the rate constant is determined at constant temperature.

Using our method of determining activation energy, the activation volume can also be related to the fluctuation in the volume during MD simulations,

$$\Delta V^{\ddagger} = \frac{1}{k}\lim_{t\to long}\langle \delta V(0)\, F_s(0)\, \theta[s(t) - s^{\ddagger}]\rangle. \tag{7.5}$$

This equation is product of the fluctuation of the reactant volume and the flux-side correlation average over the ensemble of reactant trajectories. The same can be done with the side-side and flux-flux correlation functions used in the calculation of activation energies. This method of using correlation functions will also remove the barrier to the calculation of activation volumes and should be tested with the systems investigated by Dang and coworkers.

7.2.1.2 Derivatives of Time Correlation Functions

More general behavior of time correlation functions and the associated rate constants or transport coefficients can be considered.

Consider a time correlation function (TCF),

$$C_{AB}(t) = \langle A(0)B(t)\rangle = \frac{1}{Q}\mathrm{Tr}\left[e^{-\beta H}A(0)e^{i\hat{\mathscr{L}}t}B(0)\right], \tag{7.6}$$

where H is the Hamiltonian and $\hat{\mathscr{L}}$ is the Liouville operator. Taking the derivative of the TCF with respect to a parameter (α) in the Hamiltonian (e.g, mass or potential parameter), we have,

$$\begin{aligned}\frac{\partial C_{AB}(t)}{\partial\alpha} = \frac{-1}{Q^2}\frac{\partial Q}{\partial\alpha}\mathrm{Tr}\left[e^{-\beta H}A(0)e^{i\hat{\mathscr{L}}t}B(0)\right] + \\ \frac{1}{Q}\mathrm{Tr}\left[e^{-\beta H}\left(-\beta\frac{\partial H}{\partial\alpha}\right)A(0)e^{i\hat{\mathscr{L}}t}B(0)\right] + \frac{1}{Q}\mathrm{Tr}\left[e^{-\beta H}A(0)\int_0^t e^{i\hat{\mathscr{L}}(t-s)}\frac{\partial i\hat{\mathscr{L}}}{\partial\alpha}e^{i\hat{\mathscr{L}}s}dsB(0)\right],\end{aligned} \tag{7.7}$$

where we have assumed that both A and B are independent of α, and in the last term we have used the result from R.M Wilcox.[202] If we proceed to consider each term in succession,

$$\frac{-1}{Q}\frac{\partial Q}{\partial\alpha} = \beta\frac{1}{Q}\mathrm{Tr}\left[\frac{\partial H}{\partial\alpha}e^{-\beta H}\right] = \beta\left\langle\frac{\partial H}{\partial\alpha}\right\rangle, \tag{7.8}$$

which gives,

$$\frac{-1}{Q^2}\frac{\partial Q}{\partial\alpha}\mathrm{Tr}\left[e^{-\beta H}A(0)e^{i\hat{\mathscr{L}}t}B(0)\right] = \beta\left\langle\frac{\partial H}{\partial\alpha}\right\rangle\langle A(0)B(t)\rangle, \tag{7.9}$$

the second term becomes,

$$-\beta\left\langle\frac{\partial H(0)}{\partial\alpha}A(0)B(t)\right\rangle, \tag{7.10}$$

and the sum of the first two terms,

$$-\beta\left\langle\left[\frac{\partial H(0)}{\partial\alpha} - \left\langle\frac{\partial H}{\partial\alpha}\right\rangle\right]A(0)B(t)\right\rangle = \beta\left\langle\delta\left(\frac{\partial H(0)}{\partial\alpha}\right)A(0)B(t)\right\rangle. \tag{7.11}$$

The third term can be further simplified into the form,

$$-\int_0^t ds \frac{1}{Q}\sum_j \mathrm{Tr}\left[e^{-\beta H}A(s-t)\frac{\partial F_j(s)}{\partial \alpha}\frac{\partial B(s)}{\partial p_j}\right], \tag{7.12}$$

and thus,

$$-\int_0^t ds \sum_j \mathrm{Tr}\left\langle A(s-t)\frac{\partial F_j(s)}{\partial \alpha}\frac{\partial B(s)}{\partial p_j}\right\rangle, \tag{7.13}$$

where F is the force on particle j during MD simulation and p is its momentum.

The first two terms represent the sampling or configurational derivatives, *i.e.,* how the TCF changes with parameter (α) via α affecting initial ($t = 0$) configurations.

If the parameter of the Hamiltonian is mass (m) and the correlation function in this case is the flux-side correlation function that gives the rate constant, we can calculate the derivative of this rate constant with respect to mass,

$$\frac{\partial k(T)}{\partial m} = \frac{-k}{m} + \frac{\beta}{m}\left\langle \delta T(0) F_q(0)\theta\left[q(t) - q^{\ddagger}\right]\right\rangle - \frac{t}{m}\left\langle F_q(0)F_q(t)\right\rangle, \tag{7.14}$$

where $\delta T(0)$ is the fluctuation in the kinetic energy and F_q is the force along the reaction coordinate q, and the third term becomes zero in the case of the transition state rate constant where trajectories are started from the dividing surface. The dependence of the transition state rate constant (k) on the mass (m) in the case of the Eckart barrier has been evaluated from MD simulations and the results compared to the result from the formula,

$$\frac{\partial k(T)}{\partial m} = -0.5/m^{3/2}\sqrt{\frac{k_B T}{2\pi}}e^{\frac{-V_0}{k_B T}}. \tag{7.15}$$

As shown in Fig. 7.1, the value of -4.2 $\times$ 10^{28} cm molecule^{-1} s^{-1} g^{-1} derived from the MD simulation started at the dividing surface where we used the same simulation parameters used in Chapter 3 match well with the results from Eq. 7.15.

Finally, it will be interesting to see the contribution of the time dependent third term in Eq. 7.14 when trajectories are not started from the dividing surface and the third term has to be included.

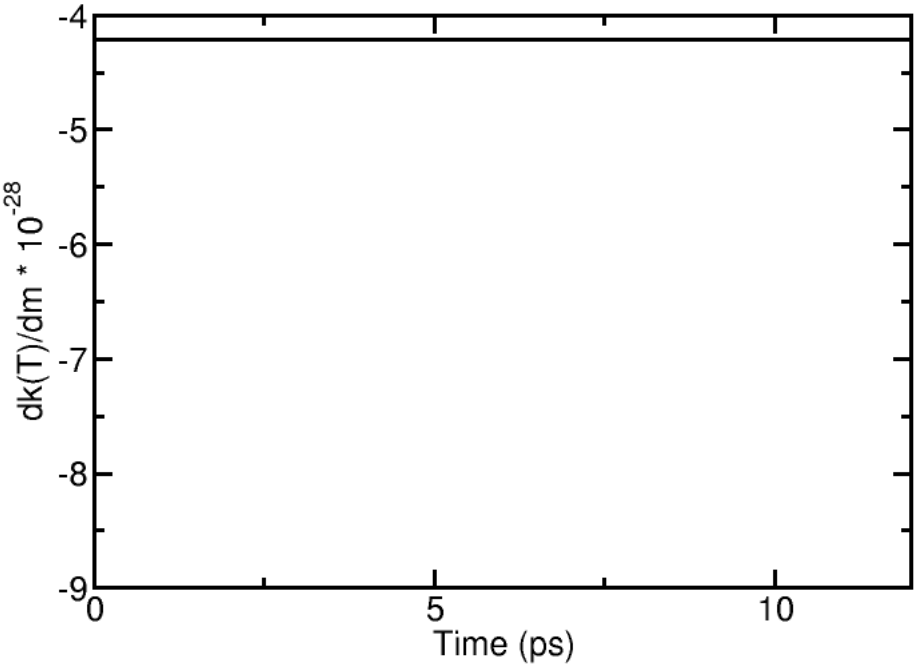

Figure 7.1: Derivative of the flux-side correlation function (See. Eq. 7.14) with respect to mass as determined from a MD simulation started at the dividing surface of the Eckart barrier.

Extensions of the parameter dependence of correlation functions to many physical quantities that involve TCFs beyond reaction rate constant (e.g. spectral diffusion) will prove to be very beneficial.

7.3 Simulating the Vibrational Spectra of OH Stretch in Alcohols

“Universal" empirical maps for the simulation of vibrational spectra of the OH stretch in alcohols have been developed for alcohols by combining data from the MD simulations of methanol, ethanol, propanol, and butanol. The empirical maps are used to simulate the IR, Raman, and 2D-IR photon-echo spectra of the OH stretch in methanol, ethanol, propanol, and the isomers of butanol.

The “universal" empirical maps shows that the correlation between the OH vibrational frequency determined by DFT calculations on clusters extracted from MD simulations and the electric field at the hydrogen atom projected along the OH bond does not depend on the nature of the

linear alcohols used to build the map. The simulated IR spectra of the linear alcohols was seen to differ slightly from experimental spectra because the simulated IR spectra is slightly blue shifted with narrower linewidths. The appearance of a shoulder at higher frequencies in the OH stretch frequency distribution of propanol and butanol indicates the presence of dangling OH bonds. An analysis of the radial distribution function of propanol and butanol indicates that non-Condon effects play a huge role in the spectra. The center-line-slope of the 2D-IR photon echo spectra was also confirmed as an accurate measure of spectral diffusion in the alcohols. Spectral diffusion times show an increase in spectral diffusion with increase in the length of the alkyl chain of the linear alcohols.

The simulated spectra of isomeric butanols, showed a narrowing of the linewidth of simulated IR spectra from the primary alcohols (*iso*-butanol and *n*-butanol) to *sec*-butanol and *tert*-butanol. Spectral diffusion calculated from the center-line-slope showed that all four isomers showed similar spectral dynamics indicating that the influence of dynamics on the linewidth of the simulated spectra of the isomers is due to the different OH reorientation dynamics. The simulated Raman spectra of all of the isomers showed a shoulder/peak with different intensities at $\sim$3700 cm^{-1} which is due to different percentages of dangling OH bonds in the isomers.

7.3.1 Future Directions

7.3.1.1 “Universal" Empirical Maps

The empirical maps developed in this work have been applied to simulate the spectra of both linear and branched alcohols. For the linear alcohols, correlation between the OH vibrational frequency and the electric field projected along the OH bond was seen to be independent of the alcohols. Building maps based on some clusters extracted from the MD simulation of the isomers of butanol will help in establishing this fact for branched alcohols as well which will further support the “universality" of alcohol maps.

Due to the small transition dipole moment of dangling OH bonds, they are silent in the IR spectra and can not be identified. As seen in the spectra of isomeric butanols, a better alternative to

this is to simulate the isotropic, perpendicular-polarized (I_{VH}), and parallel-polarized (I_{VV}) Raman spectra by building empirical maps of the respective transition polarizability that is needed to simulate these spectra. The dangling OH bonds are not silent in the Raman spectra because the transition dipole polarizability is relatively large when compared to the transition dipole moment. Following an earlier work simulating the spectra of methanol [126], the isotropic and anistropic Raman spectra is related to the vertical and horizontal spectra by the two equations below.,

$$I_{iso}(\omega) = I_{VV}(\omega) - \frac{4}{3} I_{VH}(\omega), \tag{7.16}$$

and

$$I_{ani}(\omega) = I_{VH}(\omega). \tag{7.17}$$

The polarizability tensor elements that are required to compute the spectra can be determined in a similar manner to the transition dipole moments used in simulating the IR spectra. DFT calculations on the alcohol clusters extracted from MD simulations will yield the polarizability tensor elements.

7.3.1.2 Spectra of Alcohols in Inhomogeneous Systems

Following earlier work on water, the transferability of the maps to inhomogeneous systems can be tested by simulating some alcohols in nanoscale silica pores. As the structure and dynamics of a networked liquid like water is known to change upon confinement mostly due to its interfacial molecules, the simulations of the vibrational spectra will help in the investigation of the influence of nanoconfinement on the structure and dynamics of alcohols. Simulation of non-linear spectra that probe interfacial properties of liquids like the sum-frequency generation (SFG) spectra of alcohols is also possible with the empirical maps for the transition dipole moment and transition polarizability.

Finally, the dearth in experimental spectra of isomeric butanols also makes it difficult to compare our simulated spectra to experiments. It is hoped that our ability to do these simulations will

spur an increased interest in experiments that will investigate alcohols.

7.4 Intermolecular Vibrational Coupling of OH Bonds in Water

A sinc-function discrete variable representation (DVR) was successfully used to calculate the intermolecular vibrational coupling constant between OH bonds in water. The results of this approach when compared to the commonly used transition dipole coupling (TDC) approximation gives a better estimate of the coupling constant at short intermolecular distances where the TDC approximation is known to fail.

An investigation of the effect of isotopic substitution on coupling was pursued by a comparison of intermolecular vibrational coupling in water and heavy water. The results revealed that coupling of OH bonds are more signicant than coupling of OD bonds. At long intermolecular distances of the OH or OD bonds, the TDC approximation was sufficient to estimate the coupling between the bonds of interest. Further improvement of this work will require fitting the coupling constant determined from the DVR method to a number of distance and angle criteria similar to the work by Skinner and coworkers.[203] It is hoped that such a study will help in deriving an empirical relationship between intermolecular vibration coupling and the relative geometry of the coupled bonds. Such work, will be an improvement upon the commonly used transition dipole method and help in simulating better vibrational spectra of the neat liquids and also in studies where a good estimate of the coupling constant is necessary.

References

[1] Auer, B.; Kumar, R.; Schmidt, J. R.; Skinner, J. L. *Proc. Natl. Acad. Sci.* **2007**, *104*, 14215–14220.

[2] Auer, B. M.; Skinner, J. L. *J. Chem. Phys.* **2008**, *128*, 224511.

[3] Shinokita, K.; Cunha, A. V.; Jansen, T. L. C.; Pshenichnikov, M. S. *J. Chem. Phys.* **2015**, *142*, 212450.

[4] Saiz, L.; Guardia, E.; Padro, J.-A. *J. Chem. Phys.* **2000**, *113*, 2814 –2822.

[5] Cardona, J.; Fartaria, R.; Sweatman, M. B.; Lue, L.; Cardona, J.; Fartaria, R.; Sweatman, M. B.; Lue, L. *Mol. Sim.* **2016**, *22*, 370–390.

[6] Stirnemann, G.; Laage, D. *J. Phys. Chem. Lett.* **2010**, *1*, 1511–1516.

[7] Ramasesha, K.; Roberts, S. T.; Nicodemus, R. a.; Mandal, A.; Tokmakoff, A. *J. Chem. Phys.* **2011**, *135*, 054509.

[8] Mazur, K.; Bonn, M.; Hunger, J. *J. Phys. Chem. B.* **2015**, *119*, 1558–1566.

[9] Ludwig, R.; Gill, D. S.; Zeidler, M. D. *Z. Naturforsch. A.* **1991**, *46*, 89–94.

[10] Ludwig, R.; Zeidler, M. D.; Farrar, T. C. *Z. Phys. Chem.* **1995**, *189*, 19–27.

[11] Herold, E.; Strauch, M.; Michalik, D.; Appelhagen, A.; Ludwig, R. *ChemPhysChem* **2014**, *15*, 3040–3048.

[12] Ludwig, R.; Zeidler, M. D. *Mol. Phys.* **1994**, *82*, 313–323.

[13] Ferris, T. D.; Farrar, T. C. *Mol. Phys.* **2002**, *100*, 303–309.

[14] Vartia, A. A.; Mitchell-Koch, K. R.; Stirnemann, G.; Laage, D.; Thompson, W. H. *J. Phys. Chem. B.* **2011**, *115*, 12173–12178.

[15] Ludwig, R; Zeidler, M.D; Farrar, T. *Z. Phys. Chem.* **1995**, *189*, 19–27.

[16] Ludwig, R.; Zeidler, M. *Mol. Phys.* **1994**, *82*, 313–323.

[17] Debye, P. *Polar molecules*; The Chemical Catalog Company, Inc.: New York, 1929.

[18] Ivanov, E. N. *Sov. Phys. JETP* **1964**, *18*, 1041–1045.

[19] Laage, D.; Hynes, J. T. *J. Phys. Chem. B.* **2008**, *112*, 14230–14242.

[20] Marcus, R. A. *Annu. Rev. Phys. Chem.* **1964**, *15*, 155–196.

[21] Warshel, A. *Computer Modeling of Chemical Reactions in Enzymes and Solutions*; Wiley: New York, 1997.

[22] Ando, K.; Hynes, J. *J. Phys. Chem. B.* **1997**, *101*, 10464–10478.

[23] Bentley, T. W.; Carter, G. E. *J. Am. Chem. Soc.* **1982**, *104*, 5741–5747.

[24] Vedernikova, E. V.; Gafurov, M. M.; Ataev, M. B. *Russ. Phys. J.* **2011**, *53*, 843–848.

[25] Siler, A. R.; Walker, R. A. *J. Phys. Chem. C.* **2011**, *115*, 9637–9643.

[26] Sieffert, N.; Bühl, M.; Gaigeot, M.-P.; Morrison, C. A. *J. Chem. Theor. Comp.* **2013**, *9*, 106–118.

[27] Singh, L. P.; Alba-Simionesco, C.; Richert, R. *J. Chem. Phys.* **2013**, *139*, 144503.

[28] Böhmer, R.; Gainaru, C.; Richert, R. *Phys. Rep.* **2014**, *545*, 125–195.

[29] Fennell, C. J.; Wymer, K. L.; Mobley, D. L. *J. Phys. Chem. B.* **2014**, *118*, 6438–6446.

[30] Laage, D.; Hynes, J. T. *Science* **2006**, *311*, 832–5.

[31] Fogarty, A. C.; Laage, D. *J. Phys. Chem. B.* **2013**,

[32] Fogarty, A. C.; Coudert, F.-X.; Boutin, A.; Laage, D. *Chemphyschem* **2014**, *15*, 521–529.

[33] Laage, D.; Stirnemann, G.; Hynes, J. T. *J. Phys. Chem. B.* **2009**, *113*, 2428–35.

[34] Fogarty, A. C.; Duboué-Dijon, E.; Laage, D.; Thompson, W. H. *J. Chem. Phys.* **2014**, *141*, 18C523.

[35] Laage, D.; Thompson, W. H. *J. Chem. Phys.* **2012**, *136*, 044513.

[36] Mazur, K.; Heisler, I. A.; Meech, S. R. *J. Phys. Chem. A.* **2012**, *116*, 2678–2685.

[37] Tielrooij, K. J.; van der Post, S. T.; Hunger, J.; Bonn, M.; Bakker, H. J. *J. Phys. Chem. B.* **2011**, *115*, 12638–12647.

[38] Haughney, M. *J. Phys. Chem.* **1987**, *91*, 4934–4940.

[39] Lehtola, J.; Hakala, M.; Ha, K. *J. Phys. Chem. B.* **2010**, *114*, 6426–6436.

[40] Saiz, L.; Padro, J.; Guardia, E. *J. Phys. Chem. B.* **1997**, *101*, 78–86.

[41] Padro, J. A.; Saiz, L.; Guardia, E. *J. Mol. Struct.* **1997**, *416*, 243–248.

[42] Bich, E.; Hensen, U.; Michalik, M.; Wandschneider, D.; Heintz, A. *Phys. Chem. Chem. Phys.* **2002**, *4*, 5827–5832.

[43] Gainaru, C.; Meier, R.; Schildmann, S.; Lederle, C.; Hiller, W.; Rossler, E.; Böhmer, R. *Phys. Rev. Lett.* **2010**, *105*, 258303.

[44] Hédoux, A.; Guinet, Y.; Paccou, L.; Derollez, P.; Danède, F. *J. Chem. Phys.* **2013**, *138*, 214506.

[45] Abdel Hamid, A. R.; Lefort, R.; Lechaux, Y.; Moréac, A.; Ghoufi, A.; Alba-Simionesco, C.; Morineau, D. *J. Phys. Chem. B.* **2013**, *117*, 10221–10230.

[46] Crupi, V.; Magazu, S.; Maisano, G.; Majolino, D.; Migliardo, P. *J. Phys.-Condens. Mat.* **1993**, *5*, 6819–6832.

[47] Czarnecki, M. A.; Maeda, H.; Ozaki, Y.; Suzuki, M.; Iwahashi, M. *J. Phys. Chem. A.* **1998**, *102*, 9117–9123.

[48] Czarnecki, M. A.; Czarnik-Matusewicz, B.; Ozaki, Y.; Iwahashi, M. *J. Phys. Chem. A.* **2000**, *104*, 4906–4911.

[49] Andanson, J.-M.; Soetens, J.-C.; Tassaing, T.; Besnard, M. *J. Chem. Phys.* **2005**, *122*, 174512.

[50] Palombo, F.; Paolantoni, M.; Sassi, P.; Morresi, A.; Cataliotti, R. S. *J. Mol. Liq.* **2006**, *125*, 139–146.

[51] Sokolova, M.; Barlow, S. J.; Bondarenko, G. V.; Gorbaty, Y. E.; Poliakoff, M. *J. Phys. Chem. A.* **2006**, *110*, 3882–3885.

[52] Czarnecki, M. A.; Wojtków, D.; Haufa, K. *Chem. Phys. Lett.* **2006**, *431*, 294–299.

[53] Sassi, P.; Palombo, F.; Cataliotti, R. S.; Paolantoni, M.; Morresi, A. *J. Phys. Chem. A.* **2007**, *111*, 6020–6027.

[54] Bauer, S.; Moch, K.; Münzner, P.; Schildmann, S.; Gainaru, C.; Böhmer, R. *J. Non-Cryst. Solids* **2015**, *407*, 384–391.

[55] Lederle, C.; Hiller, W.; Gainaru, C.; Böhmer, R. *J. Chem. Phys.* **2011**, *134*, 064512.

[56] Shang, X.; Benderskii, A. V.; Eisenthal, K. B. *J. Phys. Chem. B.* **2001**, *105*, 11578–11585.

[57] Zhang, X.; Steel, W.; Walker, R. *J. Phys. Chem. B.* **2003**, *107*, 3829–3836.

[58] Yanagimachi, M.; Tamai, N.; Masuhara, H. *Chem. Phys. Lett.* **1992**, *200*, 469–474.

[59] Joo, T.; Jia, Y.; Yu, J.; Lang, M.; Fleming, G. *J. Chem. Phys.* **1996**, *104*, 6089–6108.

[60] Biswas, R.; Nandi, N.; Bagchi, B. *J. Phys. Chem. B.* **1997**, *101*, 2968–2979.

[61] Nath, P. P.; Sarkar, S.; Krishna, P. S. R.; Joarder, R. N. *Appl. Phys. A-Mater.* **2002**, *74*, s348–s351.

[62] Tomsic, M.; Jamnik, A.; Fritz-Popovski, G.; Glatter, O.; Vlcek, L. *J. Phys. Chem. B.* **2007**, *111*, 1738–1751.

[63] Pylkkänen, T.; Lehtola, J.; Hakala, M.; Sakko, A.; Monaco, G.; Huotari, S.; Hämäläinen, K. *J. Phys. Chem. B.* **2010**, *114*, 13076–13083.

[64] Shmyt'ko, I. M.; Jiménez-Riobóo, R. J.; Hassaine, M.; Ramos, M. A. *J. Phys.-Condens. Mat.* **2010**, *22*, 195102.

[65] Kaatze, U.; Schumacher, A.; Pottel, R. *Ber. Bunsen. Phys. Chem.* **1991**, *95*, 585–592.

[66] Murthy, S.; Nayak, S. K. *J. Chem. Phys.* **1993**, *99*, 5362–5368.

[67] Becker, U.; Stockhausen, M. *J. Mol. Liq.* **1999**, *81*, 89–100.

[68] Andanson, J.-M.; Soetens, J.-C.; Tassaing, T.; Besnard, M. *J. Chem. Phys.* **2005**, *122*, 174512–174512.

[69] Kusalik, P. G.; Lyubartsev, A. P.; Bergman, D. L.; Laaksonen, A. *J. Phys. Chem. B.* **2000**, *104*, 9533–9539.

[70] Kusalik, P. G.; Lyubartsev, A. P.; Bergman, D. L.; Laaksonen, A. *J. Phys. Chem. B.* **2000**, *104*, 9526–9532.

[71] Yonker C.R, Wallen S.L, Palmer B.J, G. B. *J. Phys. Chem. A.* **1997**, *101*, 9564–9570.

[72] Margalit, Y. *J. Chem. Phys.* **1971**, *55*, 3072–3077.

[73] Nadolny, H.; Volmari, A.; Weingartner, H. *Ber. Bunsenges. Phys. Chem.* **1998**, *102*, 866–871.

[74] Plimpton, S. *J. Comp. Phys.* **1995**, *117*, 1–19.

[75] Jorgensen, W. L. *J. Phys. Chem.* **1986**, *90*, 1276–1284.

[76] Jorgensen, W. *J. Am. Chem. Soc.* **1996**, *118*, 11225–11236.

[77] Weast, R. C.; et al., *Handboook of Chemistry and Physics, 52nd Edition*; The Chemical Rubber Company: Cleveland, OH, 1971.

[78] Nose, S. *Mol. Phys.* **1984**, *52*, 255–268.

[79] Wiiliam G. Hoover, *Phys. Rev. A.* **1985**, *31*, 1695–1697.

[80] Shoemaker, D.P; Garland, C.W; Nibler, J. *Experiments in Physical Chemistry*; McGraw-Hill: New York, 1989.

[81] Northrup, S. H.; Hynes, J. T. *J. Chem. Phys.* **1980**, *73*, 2700–2714.

[82] Grote, R. F.; Hynes, J. T. *J. Chem. Phys.* **1980**, *73*, 2715–2732.

[83] Bowron, D.T; Finney, J.L; Soper, A. *Mol. Phys.* **1998**, *93*, 531–543.

[84] The use of τ_{libr}^{-1} for the attempt frequency is indeed crude and may not properly represent isotope effects in H-bond jump times and reorientation. For example, OD reorientation in HOD dilute in H_2O has been observed to be faster than that of OH reorientation of HOD dilute in D_2O,[85] a result that would not be predicted by $\omega_S = \tau_{libr}^{-1}$ alone. The approximation here is only intended for simple estimates and additional work is needed to improve upon it.

[85] Bakker, H. J.; Rezus, Y. L. A.; Timmer, R. L. A. *J. Phys. Chem. A.* **2008**, *112*, 11523–11534.

[86] Ansón, A.; Garriga, R.; Martínez, S.; Pérez, P.; Gracia, M. *J. Chem. Eng. Data* **2005**, *50*, 1478–1483.

[87] Yamamoto, T. *J. Chem. Phys.* **1960**, *33*, 281–289.

[88] Pechukas, P.; McLafferty, F. J. *J. Chem. Phys.* **1973**, *58*, 1622–1625.

[89] Miller, W. H. *J. Chem. Phys.* **1974**, *61*, 1823–1834.

[90] Miller, W. H.; Schwartz, S. D.; Tromp, J. W. *J. Chem. Phys.* **1983**, *79*, 4889–4898.

[91] Chandler, D. *J. Chem. Phys.* **1978**, *68*, 2959–2970.

[92] Bolhuis, P. G.; Chandler, D.; Dellago, C.; Geissler, P. L. *Annu. Rev. Phys. Chem.* **2002**, *53*, 291–318.

[93] Dellago, C.; Bolhuis, P. G. *Mol. Sim.* **2004**, *30*, 795–799.

[94] Lo, C. S.; Radhakrishnan, R.; Trout, B. L. *Catalysis Today* **2005**, *105*, 93–105.

[95] Borrero, E. E.; Dellago, C. *J. Chem. Phys.* **2010**, *133*.

[96] Drechsel-Grau, C.; Sprik, M. *J. Chem. Phys.* **2012**, *136*.

[97] Tolman, R. C. *J. Am. Chem. Soc.* **1920**, *42*, 2506–2528.

[98] This form also assumes the use of absorbing boundary conditions wherein $n_p(t) = 1$ for all times t after a trajectory reaches the product region, *i.e.*, after $s(t)$ passes s_p. In this way, longer-time dynamics associated with reformation of the reactants from the products through the reverse reaction are disregarded.

[99] Park, T. J.; Light, J. C. *J. Chem. Phys.* **1988**, *88*, 4897–4912.

[100] Thompson, W. H.; Miller, W. H. *J. Chem. Phys.* **1997**, *106*, 142.

[101] Johnston, H. S. *Gas Phase Reaction Rate Theory*; Ronald Press: New York, 1966.

[102] Colbert, D. T.; Miller, W. H. *J. Chem. Phys.* **1992**, *96*, 1982–1991.

[103] Lanczos, C. *J. Res. Natl. Bur. Stand.* **1950**, *45*, 255–282.

[104] Laage, D.; Hynes, J. T. *Science* **2006**, *311*, 832–835.

[105] Laage, D.; Hynes, J. T. *J. Phys. Chem. B.* **2008**, *112*, 14230–14242.

[106] The LAMMPS molecular dynamics package, http://lammps.sandia.gov.

[107] Berendsen, H. J. C.; Grigera, J. R.; Straatsma, T. P. *J. Phys. Chem.* **1987**, *91*, 6269–6271.

[108] Reichardt, C. *Solvents and Solvent Effects in Organic Chemistry*; VCH: New York, 1990.

[109] Mesele, O. O.; Vartia, A. A.; Laage, D.; Thompson, W. H. *J. Phys. Chem. B.* **2016**, *120*, 1546–1559.

[110] Liddel, U.; Becker, E. D. *Spectrochim. Acta* **1957**, *10*, 70–84.

[111] Uemura, T.; Saito, S.; Mizutani, Y.; Tominaga, K. *Mol. Phys.* **2005**, *103*, 37–44.

[112] Iwaki, L. K.; Dlott, D. D. *Chem. Phys. Lett.* **2000**, *321*, 419–425.

[113] Iwaki, L. K.; Dlott, D. D. *J. Phys. Chem. A.* **2000**, *104*, 9101–9112.

[114] Doroshenko, I.; Pogorelov, V.; Sablinskas, V. *Dataset Papers in Chemistry* **2013**, *2013*, 1–6.

[115] Gorbaty, Y. E.; Bondarenko, G. V. *Russ. J. Phys. Chem. B.* **2013**, *6*, 873–877.

[116] Morgado, P.; Garcia, A. R.; Ilharco, L. M.; Marcos, J.; Anastácio, M.; Martins, L. F. G.; Filipe, E. J. M. *J. Phys. Chem. B.* **2016**, *120*, 100910–10105.

[117] Michniewicz, N.; Muszyński, A. S.; Wrzeszcz, W.; Czarnecki, M. A.; Golec, B.; Hawranek, J. P.; Mielke, Z. *J. Mol. Struct.* **2008**, *887*, 180–186.

[118] Deng, G.-h.; Shen, Y.; He, Z.; Zhang, Q.; Jiang, B.; Yuan, K.; Wu, G.; Yang, X. *Phys. Chem. Chem. Phys.* **2017**, *19*, 4345–4351.

[119] Paolantoni, M.; Sassi, P.; Morresi, A.; Cataliotti, R. S. *J. Raman Spectrosc.* **2006**, *37*, 528–537.

[120] Gaffney, K. J.; Piletic, I. R.; Fayer, M. D. *J. Phys. Chem. A.* **2002**, *106*, 9428–9435.

[121] Piletic, I. R.; Gaffney, K. J.; Fayer, M. D. *J. Chem. Phys.* **2003**, *119*, 423–434.

[122] Woutersen, S. *J. Chem. Phys.* **2007**, *127*, 154517–5.

[123] Lin, K.; Zhou, X.; Luo, Y.; Liu, S. *J. Phys. Chem. B.* **2010**, *114*, 3567–3573.

[124] Lin, K.; Hu, N.; Zhou, X.; Liu, S.; Luo, Y. *J. Raman Spectrosc.* **2012**, *43*, 82–88.

[125] Barlow, S. J.; Bondarenko, G. V.; Gorbaty, Y. E.; Yamaguchi, T.; Poliakoff, M. *J. Phys. Chem. A.* **2002**, *106*, 10452–10460.

[126] Zheng, R.; Sun, Y.; Shi, Q. *Phys. Chem. Chem. Phys.* **2011**, *13*, 2027–2035.

[127] Yadav, V. K.; Karmakar, A.; Choudhuri, J. R.; Chandra, A. *Chem. Phys.* **2012**, *408*, 36–42.

[128] Yadav, V. K.; Chandra, A. *Chem. Phys.* **2013**, *415*, 1–7.

[129] Bakker, H. J.; Skinner, J. L. *Chem. Rev.* **2010**, *110*, 1498–1517.

[130] Corcelli, S. A.; Lawrence, C. P.; Skinner, J. L. *J. Chem. Phys.* **2004**, *120*, 8107–8117.

[131] Corcelli, S. A.; Skinner, J. L. *J. Phys. Chem. A.* **2005**, *109*, 6154–6165.

[132] Schmidt, J. R.; Corcelli, S. A.; Skinner, J. L. *J. Chem. Phys.* **2005**, *123*, 044513.

[133] Gruenbaum, S. M.; Tainter, C. J.; Shi, L.; Ni, Y.; Skinner, J. L. *J. Chem. Theor. Comp.* **2013**, *9*, 3109–3117.

[134] Jorgensen, W. L. *J. Phys. Chem.* **1986**, *90*, 1276–1284.

[135] Jorgensen, W. L.; Maxwell, D. S.; Tirado-Rives, J. *J. Am. Chem. Soc.* **1996**, *118*, 11225–11236.

[136] Nosé, S. *Mol. Phys.* **1984**, *52*, 255–268.

[137] Hoover, W. G. *Phys. Rev. A.* **1985**, *31*, 1695–1697.

[138] Torii, H. *J. Phys. Chem. A.* **2006**, *110*, 9469–9477.

[139] Becke, A. D. *J. Chem. Phys.* **1997**, *107*, 8554–8560.

[140] Hehre, W. J.; Ditchfield, R.; Pople, J. A. *J. Chem. Phys.* **1972**, *56*, 2257–2261.

[141] Valiev, M.; Bylaska, E. J.; Govind, N.; Kowalski, K.; Straatsma, T. P.; Van Dam, H. J. J.; Wang, D.; Nieplocha, J.; Apra, E.; Windus, T. L.; de Jong, W. A. *Comp. Phys. Comm.* **2010**, *181*, 1477–1489.

[142] Shimanouchi, T. *Tables of Molecular Vibrational Frequencies Consolidated Volume I*; National Bureau of Standards: Washington, DC, 1972.

[143] Coblentz Society, Inc., "Evaluated Infrared Reference Spectra" in **NIST Chemistry WebBook, NIST Standard Reference Database Number 69** Linstrom, P.J.; Mallard, W.G, eds., National Institute of Standards and Technology, Gaithersburg MD, 20899.

[144] In Ref. 14 we obtained $\langle\tau\rangle = 3.3 \pm 0.3$ and 6.3 ± 1.8 ps for methanol and ethanol using united-atom OPLS models.[134] The all-atom models used in the present study thus give better agreement with the available experimental data.

[145] Tielrooij, K. J.; Petersen, C.; Rezus, Y. L. A.; Bakker, H. J. *Chem. Phys. Lett.* **2009**, *471*, 71–74.

[146] Schmidt, J. R.; Roberts, S. T.; Loparo, J. J.; Tokmakoff, A.; Fayer, M. D.; Skinner, J. L. *Chem. Phys.* **2007**, *341*, 143–157.

[147] Hamm, P.; Zanni, M. *Concepts and Methods of 2D Infrared Spectroscopy*; Cambridge University Press: New York, 2011.

[148] Kwak, K.; Rosenfeld, D. E.; Fayer, M. D. *J. Chem. Phys.* **2008**, *128*, 204505.

[149] The CLS is calculated from the simulated 2D-IR spectra by examining the value of ω_3 for the $0 \rightarrow 1$ peak in the spectrum for each ω_1 value. This maximum value is determined by fitting a slice through the spectrum at a fixed ω_1 to a Gaussian over a range of 150 cm^{-1} in

ω_3. The resulting center line, obtained by connecting the maximum ω_3 values as a function of ω_1 is fit to a line for 3315 $cm^{-1} < \omega_1 <$ 3415 cm^{-1} to obtain the CLS. This calculation is repeated for each waiting time .

[150] Burris, P. C.; Laage, D.; Thompson, W. H. *J. Chem. Phys.* **2016**, *144*, 194709.

[151] Ball, P. *Nature* **2008**, *452*, 291–292.

[152] Fecko, C. J.; Loparo, J. J.; Roberts, S. T.; Tokmakoff, A. *J. Chem. Phys.* **2005**, *122*.

[153] Smith, J. D.; Cappa, C. D.; Wilson, K. R.; Cohen, R. C.; Geissler, L.; Saykally, R. J.; Smitht, J. D.; Cappat, C. D.; Wilson, K. R.; Cohent, R. C.; Geisslert, P. L.; H, R. J. S. *Proc. Natl. Acad. Sci.* **2005**, *102*, 14171 – 14174.

[154] Choi, J. H.; Cho, M. *J. Chem. Phys.* **2013**, *138*.

[155] Walrafen, G. E. *J. Chem. Phys.* **1968**, *48*, 244–251.

[156] Laenen, R.; Rauscher, C.; Laubereau, a. *Phys. Rev. Lett.* **1998**, *80*, 2622–2625.

[157] Gale, G. M.; Gallot, G.; Hache, F.; Lascoux, N.; Bratos, S.; Leicknam, J.-C. *Phys. Rev. Lett.* **1999**, *82*, 1068–1071.

[158] Piryatinski, a.; Skinner, J. L. *J. Phys. Chem. B.* **2002**, *106*, 8055–8063.

[159] Stenger, J.; Madsen, D.; Hamm, P.; Nibbering, E. T. J.; Elsaesser, T. *J. Phys. Chem. A.* **2002**, *106*, 2341–2350.

[160] Stenger, J.; Madsen, D.; Hamm, P.; Nibbering, E. T. J.; Elsaesser, T. *Phys. Rev. Lett.* **2001**, *87*, 027401.

[161] Yeremenko, S.; Pshenichnikov, M. S.; Wiersma, D. A. *Chem. Phys. Lett.* **2003**, *369*, 107–113.

[162] Corcelli, S. A.; Lawrence, C. P.; Asbury, J. B.; Steinel, T.; Fayer, M. D.; Skinner, J. L. *J. Chem. Phys.* **2004**, *121*, 8897–8900.

[163] Loparo, J. J.; Roberts, S. T.; Tokmakoff, A. *J. Chem. Phys.* **2006**, *125*.

[164] Jansen, T. C.; Auer, B. M.; Yang, M.; Skinner, J. L. *J. Chem. Phys.* **2011**, *224503*.

[165] Bakker, H. J.; Nienhuys, H. K.; Gallot, G.; Lascoux, N.; Gale, G. M.; Leicknam, J. C.; Bratos, S. *J. Chem. Phys.* **2002**, *116*, 2592–2598.

[166] Salucci, P. et al. *Science* **2003**, *301*.

[167] Brubach, J. B.; Mermet, A.; Filabozzi, A.; Gerschel, A.; Roy, P. *J. Chem. Phys.* **2005**, *122*.

[168] D'Arrigo, G.; Maisano, G.; Mallamace, F.; Migliardo, P.; Wanderlingh, F. *J. Chem. Phys.* **1981**, *75*, 4264–4270.

[169] Hare, D. E.; Sorensen, C. M. *J. Chem. Phys.* **1992**, *96*, 13–22.

[170] Yang, M.; Skinner, J. L. *Phys. Chem. Chem. Phys.* **2010**, *12*, 982–991.

[171] Carey, D. M. *J. Chem. Phys.* **1998**, *108*, 2669–2675.

[172] Green, J. L.; Lacey, A. R.; Sceats, M. G. *J. Phys. Chem.* **1986**, *90*, 3958–3964.

[173] Skinner, J. L. *J. Phys. Chem.* **1994**, *98*, 2503–2507.

[174] Sieler, G.; Schweitzer-Stenner, R. *J. Am. Chem. Soc.* **1997**, *119*, 1720–1726.

[175] Guillaume, B. C. R.; Yogev, D.; Fendler, J. H. *J. Chem. Soc., Faraday Trans.* **1992**, *88*, 1281.

[176] Lafleur, M.; Pigeon, M.; Pczolet, M. *J. Phys. Chem.* **1989**, 1522–1526.

[177] Pieniazek, P. A.; Tainter, C. J.; Skinner, J. L. *J. Chem. Phys.* **2011**, *135*.

[178] Auer, B. M.; Skinner, J. L. *J. Phys. Chem. B.* **2009**, *113*, 4125–4130.

[179] Auer, B. M.; Skinner, J. L. *Chem. Phys. Lett.* **2009**, *470*, 13–20.

[180] Ishiyama, T.; Morita, A. *J. Phys. Chem. C.* **2009**, *113*, 16299–16302.

[181] Paarmann, A.; Hayashi, T.; Mukamel, S.; Miller, R. J. D. *J. Chem. Phys.* **2008**, *128*.

[182] Giorgini, M. G. *Pure Appl. Chem.* **2004**, *76*, 157–169.

[183] Piatkowski, L.; Eisenthal, K. B.; Bakker, H. J. *Phys. Chem. Chem. Phys.* **2009**, *11*, 9033–9038.

[184] Poulsen, J. A.; Nyman, G.; Nordholm, S. *J. Phys. Chem. A.* **2003**, *107*, 8420–8428.

[185] Bian, H.; Wen, X.; Li, J.; Zheng, J. *J. Chem. Phys.* **2010**, *133*.

[186] Krimm, S.; Abe, Y. *Proc. Natl Acad. Sci.* **1972**, *69*, 2788–2792.

[187] Torii, H.; Tasumi, M. *J. Chem. Phys.* **1992**, *96*, 3379–3387.

[188] Cha, S.; Ham, S.; Cho, M. *J. Chem. Phys.* **2002**, *117*, 740–750.

[189] Ryckaert, J. P.; Ciccotti, G.; Berendsen, H. J. *J. Comp. Phys.* **1977**, *23*, 327–341.

[190] Andersen, H. C. *J. Comp. Phys.* **1983**, *52*, 24–34.

[191] Dawes, R.; Thompson, D. L.; Guo, Y.; Wagner, A. F.; Minkoff, M. *J. Chem. Phys.* **2007**, *126*, 184108.

[192] Maisuradze, G. G.; Thompson, D. L. *J. Phys. Chem. A.* **2003**, 7118–7124.

[193] Maisuradze, G. G.; Thompson, D. L.; Wagner, A. F.; Minkoff, M. *J. Chem. Phys.* **2003**, *119*, 10002.

[194] Rabitz, H.; Alis, Ö.; Alış, Ö. F. *J. Math. Chem.* **1999**, *25*, 197–233.

[195] Li, G.; Rosenthal, C.; Rabitz, H. *J. Phys. Chem. A.* **2001**, *105*, 7765–7777.

[196] Manzhos, S.; Carrington, T. *J. Chem. Phys.* **2006**, *125*, 084109.

[197] Alis, Ö. F.; Rabitz, H. *J. Math. Chem.* **2001**, *29*, 127–142.

[198] Roy, S.; Dang, L. X. *Chem. Phys. Lett.* **2015**, *628*, 30–34.

[199] Roy, S.; Dang, L. X. *J. Phys. Chem. B.* **2016**, *120*, 1440–1445.

[200] Dang, L. X.; Chang, T.-m.; Dang, L. X.; Chang, T.-m. *J. Chem. Phys.* **2016**, *145*.

[201] Dang, L. X.; Schenter, G. K. *Chem. Phys. Lett.* **2016**, *643*, 142–148.

[202] Wilcox, R. M. *J. Math. Phys.* **1967**, *8*, 962 – 982.

[203] Kumar, R.; Schmidt, J. R.; Skinner, J. L. *J. Chem. Phys.* **2007**, *126*, 204107.

Appendix A

Empirical Maps Derived for Methanol, Ethanol, Propanol, and Butanol.

Table A.1: Individual empirical map equations for OH (OD) transition frequencies (ω_{nm}), coordinate matrix elements (x_{nm}), and dipole derivatives (μ') for methanol. Frequencies are in cm^{-1}, while coordinates, the dipole derivative, and the electric field ($\mathscr{E}$) are in atomic units.

Map Equation for OH	RMSD
$\omega_{01} = 3771 - 8427\,\mathscr{E} - 33634\,\mathscr{E}^2$	70
$\omega_{12} = 3649 - 9459\,\mathscr{E} - 65037\,\mathscr{E}^2$	88
$x_{01} = 0.1926 - 1.7446 \times 10^{-5}\ \omega_{01}$	9.1×10^{-5}
$x_{12} = 0.26815 - 2.4295 \times 10^{-5}\ \omega_{12}$	2.7×10^{-4}
Map Equation for OD	
$\omega_{01} = 2736 - 5871\,\mathscr{E} - 17876\,\mathscr{E}^2$	47
$\omega_{12} = 2661 - 6246\,\mathscr{E} - 32005\,\mathscr{E}^2$	55
$x_{01} = 0.1643 - 2.0732 \times 10^{-5}\omega_{01}$	5.9×10^{-5}
$x_{12} = 0.2293 - 2.8749 \times 10^{-5}\omega_{12}$	1.1×10^{-4}
Map Equation for OH and OD	
$\mu' = 0.1295 + 15.42\,\mathscr{E}$	0.074

Table A.2: Individual empirical map equations for OH (OD) transition frequencies (ω_{nm}), coordinate matrix elements (x_{nm}), and dipole derivatives (μ') for ethanol. Frequencies are in cm^{-1}, while coordinates, the dipole derivative, and the electric field ($\mathscr{E}$) are in atomic units.

Map Equation for OH	RMSD
$\omega_{01} = 3745 - 6324\,\mathscr{E} - 73719\,\mathscr{E}^2$	65
$\omega_{12} = 3620 - 6655\,\mathscr{E} - 121999\,\mathscr{E}^2$	83
$x_{01} = 0.1922 - 1.7416 \times 10^{-5}\ \omega_{01}$	1.1×10^{-4}
$x_{12} = 0.2668 - 2.3997 \times 10^{-5}\ \omega_{12}$	2.6×10^{-4}
Map Equation for OD	
$\omega_{01} = 2702 - 4360\,\mathscr{E} - 44698\,\mathscr{E}^2$	50
$\omega_{12} = 2625 - 4333\,\mathscr{E} - 66976\,\mathscr{E}^2$	51
$x_{01} = 0.1638 - 2.0834 \times 10^{-5}\omega_{01}$	1.2×10^{-4}
$x_{12} = 0.2283 - 2.8716 \times 10^{-5}\omega_{12}$	1.7×10^{-4}
Map Equation for OH and OD	
$\mu' = 0.067 + 16.87\,\mathscr{E}$	0.078

Table A.3: Individual empirical map equations for OH (OD) transition frequencies (ω_{nm}), coordinate matrix elements (x_{nm}), and dipole derivatives (μ') for *n*-propanol. Frequencies are in cm^{-1}, while coordinates, the dipole derivative, and the electric field ($\mathscr{E}$) are in atomic units.

Map Equation for OH	RMSD
$\omega_{01} = 3698 - 6331\,\mathscr{E} - 62745\,\mathscr{E}^2$	66
$\omega_{12} = 3570 - 6704\,\mathscr{E} - 106643\,\mathscr{E}^2$	88
$x_{01} = 0.1921 - 1.7579 \times 10^{-5}\ \omega_{01}$	8.1×10^{-5}
$x_{12} = 0.2669 - 2.4313 \times 10^{-5}\ \omega_{12}$	2.3×10^{-4}
Map Equation for OD	
$\omega_{01} = 2664 - 4388\,\mathscr{E} - 37085\,\mathscr{E}^2$	44
$\omega_{12} = 2587 - 4420\,\mathscr{E} - 56842\,\mathscr{E}^2$	50
$x_{01} = 0.1633 - 2.0979 \times 10^{-5}\omega_{01}$	5.3×10^{-5}
$x_{12} = 0.2276 - 2.8941 \times 10^{-5}\omega_{12}$	9.7×10^{-5}
Map Equation for OH and OD	
$\mu' = 0.1049 + 16.06\,\mathscr{E}$	0.074

Table A.4: Individual empirical map equations for OH (OD) transition frequencies (ω_{nm}), coordinate matrix elements (x_{nm}), and dipole derivatives (μ') for *n*-butanol. Frequencies are in cm^{-1}, while coordinates, the dipole derivative, and the electric field ($\mathscr{E}$) are in atomic units.

Map Equation for OH	RMSD
$\omega_{01} = 3740 - 6810\,\mathscr{E} - 59849\,\mathscr{E}^2$	63
$\omega_{12} = 3617 - 7617\,\mathscr{E} - 96422\,\mathscr{E}^2$	88
$x_{01} = 0.1918 - 1.7411 \times 10^{-5}\ \omega_{01}$	7.9×10^{-5}
$x_{12} = 0.2661 - 2.3922 \times 10^{-5}\ \omega_{12}$	2.3×10^{-4}
Map Equation for OD	
$\omega_{01} = 2688 - 4609\,\mathscr{E} - 36829\,\mathscr{E}^2$	42
$\omega_{12} = 2613 - 4797\,\mathscr{E} - 539963\,\mathscr{E}^2$	48
$x_{01} = 0.1632 - 2.0905 \times 10^{-5}\omega_{01}$	6.4×10^{-5}
$x_{12} = 0.2275 - 2.8844 \times 10^{-5}\omega_{12}$	1.2×10^{-4}
Map Equation for OH and OD	
$\mu' = 0.0787 + 16.77\,\mathscr{E}$	0.081